Reaction mechanism study of vanadium pentoxide as cathode material for beyond-Li energy storage *via in operando* techniques

Zur Erlangung des akademischen Grades eines
DOKTORS DER NATURWISSENSCHAFTEN
(Dr. rer. nat.)

von der KIT-Fakultät für Chemie und Biowissenschaften
des Karlsruher Instituts für Technologie (KIT)
genehmigte

DISSERTATION

von
QIANG FU
aus China

KIT-Dekan: Prof. Dr. Reinhard Fischer

Referent: Prof. Dr. Helmut Ehrenberg

Korreferent: Prof. Dr. Stefano Passerini

Tag der mündlichen Prüfung: 07.05.2019

Die vorliegende Arbeit wurde im Zeitraum vom 1. Oktober 2015 bis 22. March 2019 am Institut für Anorganische Chemie der Fakultät für Chemie und Biowissenschaften am Karlsruher Institut für Technologie (KIT) unter der Leitung von Prof. Dr. Helmut Ehrenberg angefertigt.

Hiermit versichere ich, die vorliegende Arbeit selbstständig verfasst und keine anderen als die angegebenen Quellen und Hilfsmittel verwendet sowie Zitate kenntlich gemacht zu haben. Die Dissertation wurde bisher an keiner anderen Hochschule oder Universität eingereicht.

Karlsruhe,

Qiang Fu

Abstract

The current thesis focuses on the study of the ion storage mechanism in V_2O_5 cathode material. In particular, the storage of Mg^{2+}, K^+, and Zn^{2+} is investigated through *in operando* Synchrotron Diffraction and *in operando* X-ray Absorption Spectroscopy in combination with *ex situ* Raman and X-ray Photoelectron Spectroscopy (XPS) or Transmission Electron Microscopy (TEM). In addition, the electrochemical performance of V_2O_5 as cathode materials in the three different systems (rechargeable Mg, K-ion and aqueous Zn batteries) was also investigated. Moreover, cation doping in the orthorhombic V_2O_5 material is investigated and the location of doping cation in the interstitial position in M-V_2O_5 (M=Ni, Mn, and Fe) is determined. All the orthorhombic V_2O_5-based materials were synthesized via a hydrothermal method. The work on the V_2O_5 is organized in four sections as described below:

(I) *V_2O_5 in rechargeable Mg batteries (MBs)*. Metallic Mg is incompatible with electrolytes containing salts and solvents that are normally used in Li-ion batteries. For this reason, in order to investigate the reaction mechanism of V_2O_5 during Mg-ion insertion/extraction by *in operando* techniques, a special cell configuration based on V_2O_5 cathode, 1 M $Mg(ClO_4)_2$/acetonitrile electrolyte and $Mg_xMo_6S_8$ (x~2) anode (schematically: $V_2O_5 \vert Mg(ClO_4)_2/AN \vert Mg_xMo_6S_8$) was designed. In this cell configuration, the V_2O_5 electrode delivers an initial magnesiation/de-magnesiation capacity of 103 mAh g^{-1}/110 mAh g^{-1} and the highest magnesiation capacity of 130 mAh g^{-1} in the 6th cycle at C/20 rate. *In operando* synchrotron diffraction and *ex situ* Raman revealed a phase transition into a new Mg-rich phase ε-$Mg_xV_2O_5$, which is forming during Mg insertion. Moreover, the recovery of α-V_2O_5 after Mg extraction has been demonstrated. *In operando* XAS and *ex situ* XPS confirm the reduction/oxidation of vanadium during the Mg insertion/extraction. Therefore, the high reversibility, crystal structure changes, and the evolution of the oxidation states of V_2O_5 during magnesium insertion/extraction are fully clarified.

(II) *V_2O_5 in rechargeable K-ion batteries (KIBs)*. Compared with MBs, V_2O_5 in 1 M KPF_6/PC electrolyte displays a higher initial insertion capacity of 200 mAh g^{-1} (corresponding to the insertion of 1.36 K^+) and a de-insertion capacity of 217 mAh g^{-1} in the potential range of 1.5 - 4.0 V vs K^+/K. These values have been obtained with the higher rate of C/12, suggesting faster kinetics for KIBs with respect to MBs. However, the capacity of V_2O_5 rapidly fades to 54 mAh g^{-1} at the 31st cycle. After that, the capacity slowly increases up to 80 mAh g^{-1} at the 200th cycle. The storage

mechanism upon K ions insertion into V_2O_5 is studied by *in operando* synchrotron diffraction and *in operando* XAS, as well as by *ex situ* Raman and TEM. *In operando* synchrotron diffraction revealed that during the first K ions insertion V_2O_5 first undergoes a solid solution and then a coexistence of solid solution and two-phase reaction. Upon K ions extraction, the coexistence of solid solution and the two-phase reaction is identified together with irreversible processes. *In operando* XAS confirmed the reduction/oxidation of vanadium during the K insertion/extraction with some irreversibility, in consistency with the other results obtained.

(III) *V_2O_5 in rechargeable aqueous Zn batteries (ZBs)*. In 1M $ZnSO_4$/water electrolyte, V_2O_5 nanowires deliver much higher initial insertion/de-insertion capacities (277 and 432 mAh g^{-1} at 50 mA g^{-1}, close to its theoretical capacity of 294 mAh g^{-1}) compared with those obtained in MBs and KIBs. However, in this electrolyte, capacity retention is poor (discharge capacity is only 21 mAh g^{-1} after 100 cycles). The V_2O_5 nanowires demonstrate much faster kinetics in aqueous ZBs with respect to organic MBs and KIBs. We found that V_2O_5 first undergoes a solid solution and two-phase reaction along with the formation of two byproducts $Zn_3(OH)_2V_2O_7{\cdot}2(H_2O)$ and $ZnSO_4Zn_3(OH)_6{\cdot}5H_2O$. This process is reversible upon Zn ion extraction. However, the formation of $Zn_3(OH)_2V_2O_7{\cdot}2(H_2O)$ is found to take place during the first discharge only and is not observed in the subsequent cycles. *In operando* XAS confirms the reduction/oxidation of vanadium during the Zn insertion/extraction with partial irreversibility.

(IV) *Metal doping in V_2O_5*. The preferred location of the doped cation (substitutional or interstitial position) in V_2O_5 is studied with three different examples (Mn, Ni, and Fe). Single phase for pristine and both Mn- and Ni-doped V_2O_5 is obtained through hydrothermal method ($M_xV_{2-x}O_5$, M= Mn, Ni, x=0, 0.1 and 0.2). Rietveld refinement confirmed that the Mn, Ni, and Fe prefer to locate in the interstitial position in the M-doped V_2O_5 ($M_xV_{2-x}O_5$, M= Mn, Ni, x= 0.1 and 0.2). However, an impurity phase of $Fe_2V_4O_{13}$ is also obtained for $Fe_xV_{2-x}O_5$ (x= 0.1 and 0.2). To gain a complete understanding of the cations doping in the V_2O_5 structure, several techniques are used such as chemical analysis, synchrotron diffraction, Pair distribution function (PDF), SEM, Raman, XPS, ^{51}V NMR, and XAS (XANES and EXAFS).

In addition to the study of V_2O_5, other works performed during my PhD study have been briefly summarized in the last part of this thesis, including the international cooperation work with Jilin University and TiO_2 in MBs and hybrid Li/Mg batteries, as well as results obtained with novel Ca-doped Lithium vanadium phosphate (LVP) materials used as anodes for LIBs.

Zusammenfassung

Die vorliegende Arbeit beschäftigt sich mit der Untersuchung des Ionenspeichermechanismus in V_2O_5-Kathodenmaterial. Insbesondere wurde die Speicherung von Mg^{2+}, K^+ und Zn^{2+} mit *in operando*-Synchrotronbeugung und *in operando* Röntgenabsorptionsspektroskopie in Kombination mit *ex situ* Raman und Röntgenphotoelektronenspektroskopie (XPS) oder Transmissionselektronenmikroskopie (TEM) untersucht. Weiterhin wurden die elektrochemischen Eigenschaften von V_2O_5 als Kathodenmaterial in den drei verschiedenen Systemen (wiederaufladbaren Mg, K-Ionen and Zn-Batterien) untersucht. Darüber hinaus wurde orthorhombisches V_2O_5 mit verschiedenen Metallkationen (Ni-, Mn- und Fe-Ionen) dotiert und deren interstitielle Lage in M-V_2O_5 (M = Ni, Mn und Fe) bestimmt. Alle V_2O_5 basierten orthorhombischen Materialien wurden über ein Hydrothermalverfahren synthetisiert. Die vorliegende Arbeit ist in vier Abschnitte unterteilt, die im Folgenden näher beschrieben werden.

(I) *V_2O_5 in wiedraufladbaren Mg-Batterien (MBs).* Eine spezielle Zellkonfiguration, basierend auf einer V_2O_5-Kathode, 1 M $Mg(ClO_4)_2$/Acetonitril-Elektrolyt und einer $Mg_xMo_6S_8$ (x~2) Anode (schematisch: $V_2O_5 | Mg(ClO_4)_2/AN | Mg_xMo_6S_8$), wurde entwickelt. Der Reaktionsmechanismus von V_2O_5, während der Mg-Ionen-Interkalation/Deinterkalation wurde mit Hilfe von *in operando*-Techniken untersucht. In dieser Zellkonfiguration liefert die V_2O_5-Elektrode eine anfängliche Magnesierungs-/Entmagnesierungskapazität von 103 mAh g^{-1}/110 mAh g^{-1} und erreicht die höchste Magnesiumkapazität von 130 mAh g^{-1} im sechsten Zyklus bei einer C/20-Rate. *In operando* Synchrotronbeugung und *ex situ* Raman zeigen den Phasenübergang in eine neue, Mg-reiche ε-$Mg_xV_2O_5$-Phase, die sich während der Mg-Interkalation bildet. Darüber hinaus wurde die Rückumwandlung zu α-V_2O_5 nach Mg-Deinterkalation nachgewiesen. *In operando* XAS und *ex situ* XPS bestätigten die Reduktion/Oxidation von Vanadium während der Mg-Interkalation/Deinterkalation. Die hohe Reversibilität, die Kristallstrukturänderungen und die Entwicklung der Oxidationszustände von V_2O_5 während der Interkalation/Deinterkalation von Magnesium wurde somit vollständig erklärt.

(II) *V_2O_5 in wiedraufladbaren K-Ionen-Batterien (KIBs).* Verglichen mit MBs zeigt V_2O_5 in 1 M KPF_6/PC-Elektrolyten eine höhere anfängliche Interkalationskapazität von 200 mAh g^{-1} (entsprechend der Interkalation von 1,36 K^+) und Deinterkalationskapazität von 217 mAh g^{-1} im Potenzialbereich von 1,5 – 4,0 V gegen K^+/K. Diese Werte wurden mit der höheren C/12-Rate

erhalten, was auf eine schnellere Kinetik in KIBs im Vergleich zu MBs schließen lässt. Die Kapazität von V_2O_5 sinkt jedoch beim 31. Zyklus schnell auf 54 mAh g^{-1}. Danach steigt die Kapazität im 200. Zyklus langsam auf bis zu 80 mAh g^{-1} an. Der Speichermechanismus der Interkalation von K-Ionen in V_2O_5 wurde mittels *in operando*-Synchrotronbeugung und *in operando* XAS sowie *ex situ* Raman und TEM untersucht. *In operando* Synchrotronbeugung zeigte, dass V_2O_5 während der ersten K-Ionen-Interkalation zuerst eine Mischkristallphase bildet und dann eine Koexistenz von Mischkristall und Zweiphasengebiet aufweist. Neben der Koexistenz der Mischkristallphase und des Zweiphasengebiets wurden auch irreversible Prozesse bei der Deinterkalation von K-Ionen bestätigt. Die mit *in operando* XAS bestätigte Reduktion/Oxidation von Vanadium während K-Interkalation/Deinterkalation und die teilweise Irreversibilität stehen im Einklang mit den Ergebnissen aus Synchrotronbeugung, Raman und TEM.

(III) *V_2O_5 in wiedraufladbaren wässrigen Zn-Batterien (ZBs).* Im 1 M $ZnSO_4$ / Wasser-Elektrolyten liefern V_2O_5-Nanodrähte viel höhere anfängliche Interkalations/Deinterkalations-Kapazitäten (277 und 432 mAh g^{-1} bei 50 mA g^{-1}, nahe ihrer theoretischen Kapazität von 294 mAh g^{-1}) im Vergleich zu MBs und KIBs. In diesem Elektrolyten ist die Zyklenstabilität jedoch schlecht (die Entladekapazität beträgt nach 100 Zyklen nur noch 21 mAh g^{-1}). Die V_2O_5-Nanodrähte zeigen eine viel schnellere Kinetik in ZBs als in organischen MBs und KIBs. Wir konnten zeigen, dass V_2O_5 zuerst einen Mischkristall bildet und dann ein Zweiphasengebiet durchläuft, zusammen mit der Bildung der zwei Nebenprodukte $Zn_3(OH)_2V_2O_7 \cdot 2(H_2O)$ und $ZnSO_4Zn_3(OH)_6 \cdot 5H_2O$. Dieser Vorgang ist bezüglich der Zn-Ionen-Deinterkalation reversibel. Die Bildung von $Zn_3(OH)_2V_2O_7 \cdot 2(H_2O)$ findet jedoch nur während der ersten Entladung statt und wird in den nachfolgenden Zyklen nicht beobachtet. *In operando* XAS bestätigt die Reduktion/Oxidation von Vanadium während der Zn-Interkalation/Deinterkalation mit teilweiser Irreversibilität.

(IV) *Metalldotierung in V_2O_5.* Die bevorzugte Position des dotierten Kations (Substitutions- oder Interstitialposition) in V_2O_5 wird anhand von drei verschiedenen Beispielen (Mn, Ni und Fe) untersucht. Einphasiges Material sowohl für das reine als auch das Mn- und Ni-dotierte V_2O_5 wird durch Hydrothermalsynthese erhalten ($M_xV_{2-x}O_5$, M = Mn, Ni, x = 0, 0,1 und 0,2). Die Rietveld-Verfeinerung zeigte, dass Mn, Ni und Fe bevorzugt in der interstitiellen Position im M-dotierten V_2O_5 ($M_xV_{2-x}O_5$, M = Mn, Ni, x = 0,1 und 0,2) vorliegen. Es wird jedoch eine Phasenverunreinigung durch $Fe_2V_4O_{13}$ in $Fe_xV_{2-x}O_5$ (x = 0,1 und 0,2) erhalten, mit Ausnahme des

Fe-haltigen V_2O_5. Um ein umfassendes Verständnis der Kationen-Dotierung in der V_2O_5-Struktur zu erhalten, werden verschiedene Techniken wie chemische Analyse, Synchrotronbeugung, Paarverteilungsfunktion (PDF), SEM, Raman, XPS, ^{51}V-NMR und XAS (XANES und EXAFS) verwendet.

Im Anschluss werden weitere Arbeiten, die während meiner Doktorarbeit durchgeführt wurden, kurz zusammengefasst. Dazu gehören die internationale Zusammenarbeit mit der Jilin Universität und TiO_2 in MBs und Hybrid-Li/Mg-Batterien, sowie Ergebnisse mit Ca-dotierten Lithiumvanadiumphosphat (LVP) Materialien, die als Anoden für LIBs verwendet werden.

.

Acknowledgments

First of all, I would like to thank my supervisor Prof. Dr. Helmut Ehrenberg for his continuous support, guidance and valuable advice during my PhD study who offered me a chance to do my research with the whole group in Institute of Applied materials - Energy Storage Systems (IAM - ESS), KIT. Besides, I would like to thank co-supervisor Dr. Natalia Bramnik (10.2015-09.2016, - present), Dr. Aiswarya Bhaskar (10.2016-12.2016) and Dr. Sonia Dsoke (01.2017-present), for their support, enthusiastic encouragement, valuable guidance, thoughtful suggestions and discussion as well as so much patience to teach me "How to do research with my work from scientific side" and "How to present my research/work to other people including writing and giving a presentation" during my study. Moreover, I would express many thanks to Dr. Angelina Sarapulova for her support and much patience from both experimental part and many discussions for analyzing the data of synchrotron diffraction and X-ray absorption spectroscopy (XAS).

I also would like to express much thankfulness to all my colleagues in our IAM-ESS for their support from the scientific part, technique part, and daily life as well as the wonderful, harmonious and warm atmosphere in the last three years. In particular, I want to thank Dr. Michael Knapp for his lecture about the Rietveld method refinement and for his thoughtful discussion and answers related to crystal structure aspects. Ditty Dixon is gratefully thanked because of his introductory course for X-ray absorption spectroscopy and many discussion associated with XAS result. Murat Yavuz is also thanked for his instruction course of Pair distribution function. Raheleh Azmi, Vanessa Trouillet, Xinlin Luo, and Julia Maibach are thanked for their XPS measurements and discussion with respect to the specific materials. I want to thank Mrs. Bettina Hunzinger for her contributions to SEM measurements and Mrs. Liuda Mereacre for her contributions to TGA and IR measurements. I greatly appreciate the support from Ms. Lihua Zhu for the Raman measurements and discussions. Dr. Maximilian Kaus is acknowledged for the NMR measurement and Dr. Sylvio Indris is gratefully thanked for the contribution to NMR measurement, analysis, and discussion. I am also appreciative for great time and many sleepless nights spent with my beamtime colleagues Heike Stöffler, Florian Sigel, Björn Schwarz, Angelina, Georg Bosch, Christoph Dräger, Sylvio Indris, Weibo Hua, Chengping Li, Guiying Tian, Zijian Zhao, Geethu Balachandran, Xinyang Liu, Michael Knapp, Sonia during the measurement in synchrotron beamline in Hamburg and Barcelona. I would like to thank my master student Nadine

Michenfelder, Shuoqi Liu, and Jiaqi Wang as well as my student research assistant Philipp Kamm for their kind support with materials and samples preparation as well as electrochemistry study. I want to express many thanks to Almut Kriese for her continuous support with many documents, Richard Hans Schneider and Heinz-Robert Goebel for their many supports with network and laptop. Felix Thol and Marcus Mayer are also thanked for technical help. Marina Bauer and Michael Knapp are thanked for the German checking and corrections.

This work has gained benefit from beamtime allocation at BL04 - MSPD at ALBA Synchrotron (Barcelona, Spain), at the XAS beamline Synchrotron at the KIT (ANKA, Karlsruhe), and at High Resolution powder Diffraction Beamline P02.1 and Hard X-ray Absorption Spectroscopy Beamiline P64 and P65 at DESY (PETRA III, Hamburg, Germany). I also want to express my heartfelt thanks to Beamline scientist Dr. Aleksandr Missiul, Dr. Francois Fauth of Experiments Division from ALBA, Alexander Schoekel, Martin Etter, Edmund Welter, Ruidy Nemausat, Vadim Murzin from Experiments Division in DESY, and Stefan Mangold from Experiments Division in ANKA for their support in the beamline.

The submitted study is accomplished at the Center for Electrochemical Energy Storage Ulm-Karlsruhe (CELEST) and IAM - ESS, Karlsruhe Institute of Technology (KIT), Germany. I would acknowledge a research scholarship from the Ministry of Science, Research, and the Arts of Baden-Württemberg (MWK) in the frame of the competence network “Functional nanostructures” for the support from October 2015 to September 2016 and the financial support from Initiative and Networking Fund of the Helmholtz Association within the Network of Excellence on post-Lithium batteries (ExNet-0035) and Deutsche Forschungsgemeinschaft (DFG, German Research Foundation) under Germany´s Excellence Strategy - EXC-2154/1 - Project A.2.1.

I would like to thank my thesis committee members: Prof. Dr. Helmut Ehrenberg, Prof. Dr. Stefano Passerini, Prof. Dr. Jan-Dierk Grunwaldt, and Priv.-Doz. Dr. Pavel Levkin, for all of their guidance and valuable discussion.

Finally, I want to express my deep thanks to my parents, sister, brother and my girlfriend Hainan for their endless love, confidence, support and encouragement to me in my life.

Karlsruhe, May 2019,

Qiang Fu,

Contents

Symbols and Abbreviations

AN	Acetonitrile
CV	Cyclic voltammetry
ESSs	Energy storage systems
EXAFS	Extended X-ray absorption fine structure
GCPL	Galvanostatic cycling with potential limitation
HRTEM	High-resolution transmission electron microscope
KIBs	Potassium-ion batteries
LCF	Linear combination fitting
LIBs	Lithium-ion batteries
LVP	Lithium vanadium phosphate
NIBs	Sodium-ion batteries
NMIB	Na^+/Mg^{2+} hybrid-ion battery
NMP	N-Methyl-2-pyrrolidone
NMR	Nuclear magnetic resonance
MBs	Magnesium batteries
PDF	Pair distribution function
PTFE	Polytetrafluoroethylene
PVDF	Polyvinylidene difluoride
SEM	Scanning electron microscope/microscopy
SHE	Standard hydrogen electrode
SS	Stainless Steel
TEM	Transmission electron microscopy
TMOs	Transition metal oxides
XANES	X-ray absorption near-edge structure
XAS	X-ray absorption spectroscopy
XRD	X-ray powder diffraction
ZBs	Zinc batteries

List of Figures

Chapter 1 Introduction

1.1 Background

Along with the vigorous expansion of population and the rapid development in modern society, the demands for energy increase progressively. In recent years, the high greenhouse gas levels, CO_2, and pollutant gas emission coming from large consumption of fossil fuels have resulted in very serious environmental problems, such as global warming and environmental pollution[1-5]. Consequently, renewable energy sources, such as solar, wind, geothermal power, biomass energy, etc. are playing important roles being as power supplies. Particularly, solar and wind power are gradually becoming a large part of energy proportion share. They are inherently intermittent and generally dispersed, strongly depending on the weather, time, and season, as well as location, while the consumption and demands of electric energy are comparatively constant[5-7]. Some unpredictable and serious problems, for instance, safety issue, for power grids may arise from the online operation of renewable energy generation systems because of their intermittent output. Therefore, rechargeable batteries, being large-scale electric energy storage systems (EESs), are necessary and very important to realize the smooth integration of these intermittent energies into grids[8-10].

Currently, rechargeable lithium-ion batteries (LIBs) are playing very important roles in modern society and our daily life since its commercialization in the 1990s, owing to their superior performance, such as high power/energy density, high voltage, and long cycle life[11-15]. Compared with other rechargeable batteries, such as nickel-cadmium (Ni-Cd), lead-acid batteries, and nickel-metal hydride (Ni-MH) batteries, lightweight, environmental compatibility, and high power/energy density make LIBs more competing and widely used in portable electrical devices, such as laptops, mobile phones, and digital electronics etc[16-18]. However, their applications in terms of the large-scale energy storage systems are strongly limited by the manufacturing cost and safety concerns. There are some very essential criteria required for large-scale EES as reported by Kang et al. and Yang et al.[5, 19] including 1) high safety for long-time usage; 2) low cost of manufacture and maintenance; 3) long cycle calendar life; 4) nontoxicity and environmental benignity.

Considering the cost and abundance of elements, the cost of raw materials, Li_2CO_3, is increasing and the relative abundance of lithium in the crust of the Earth is rather low (only 20 ppm)[20]. In addition, lithium resources are unevenly distributed (mainly in South America), which results in a high risk of unstable supply and the price increase of Li market. Therefore, it is very urgent to develop other rechargeable batteries based on rich resources and low cost, for example, Mg batteries (MBs)[16], K-ion batteries (KIBs)[21-22], and aqueous Zn batteries (ZBs).

Vanadium pentoxide (V_2O_5) has received great attention as a very promising cathode materials for LIBs due to its significant advantages, such as high energy density (theoretical capacity of 294 mAh g^{-1} with 2 Li ions insertion), high working voltage, high cost-efficiency, and easy preparation, as well as adequate safety[15, 23-25]. Because of its layered structure, there are large enough interstitial voids in V_2O_5 to accept various guest species such as Li^+, K^+, Na^+, and Mg^{2+}, as well as Zn^{2+}[26]. In the present PhD thesis, V_2O_5 as cathode materials for MBs, KIBs, and aqueous ZBs will be investigated regarding its electrochemical performance and reaction mechanism during guest ions insertion and extraction.

The key components of the Li-ion, Mg, K-ion, and Zn batteries are electrodes. The structure of electrode materials undergoes continuous evolution during cycling in the battery. It is very important to better understand the correlation between the structure evolution of the materials in "real time" and electrochemical performance during cycling, which can be used to improve the performance and guide the development and application of new materials with high performance. Synchrotron-based techniques, *in operando* synchrotron powder diffraction and *in operando* X-ray absorption spectroscopy (XAS), are very powerful and high-efficiency tools and approaches to uncover the evolution of crystal structure and the local structure and oxidation state of the materials during the electrochemical reaction[27-30]. Although the catalysis community has mainly agreed on using the expression "operando", "operando" would be incorrect from a grammar point of view. I would favour the correct Latin expression and therefore, use "in operando" version in my thesis.

In operando study of battery materials possesses remarkable advantages by comparison with the traditional *ex situ* methods for the following reasons[29, 31-33]: (i) it is possible directly to look into the reaction arising at the sample, giving higher precision and better reliability for the data collection and analysis; (ii) it continuously monitors the structure changes and electrochemical processes (time-resolved) during operation, offering the valuable information under "real-time" operation; (iii) it allows the investigation under non-equilibrium process during reactions, where the non-equilibrium or intermediate species or states cannot be detected by *ex situ* measurements; (iv) it sensibly reduces the workload of assembling and disassembling cells and eliminate sample variance from independent samples; (v) it effectively avoids the unpredictable contamination and irreversible changes of highly reactive samples at discharged/charged state during preparation, handling and transportation for *ex situ* measurements.

1.2 Overview of Li-ion batteries

1.2.1 Components and working principle of lithium-ion batteries

In general, a LIB is composed of a negative (Anode) electrode and a positive (Cathode) electrode in an electrolyte, separated by a separator. The electrolyte provides the pure ionic conductivity, transporting the ions between the two electrodes, while the separator, made of microporous membrane, is a physical barrier between the negative and positive to prevent short circuit. As shown in **Figure 1.1**, $LiCoO_2$ cathode and the graphite anode are used as an example[12, 34-35] to illustrate the electrochemical reaction mechanism during cycling. Upon charging, lithium-ions are reversibly extracted from $LiCoO_2$ cathode material (eq.1.1) and inserted into the carbonaceous anode material (eq.1.2) through the electrolyte, while the corresponding electrons simultaneously flow from the cathode side to the anode through an external circuit, resulting in the reduction of the anode and oxidation of cathode (eq.1.3). Upon discharging, lithium-ions and electrons move reversely (eq.1.4-6). Therefore, LIBs are also known as "Rocking-chair" batteries. The electrochemical reaction can be described as follows:

Charge: $LiCoO_2 \rightarrow Li_{1-x}CoO_2 + xLi^+ + xe^-$ (1.1)

: $C + xLi^+ + xe^- \rightarrow CLi_x$ (1.2)

Total reaction: $LiCoO_2 + C \rightarrow Li_{1-x}CoO_2 + CLi_x$ (1.3)

Discharge: $Li_{1-x}CoO_2 + xLi^+ + xe^- \rightarrow LiCoO_2$ (1.4)

: $CLi_x \rightarrow C + xLi^+ + xe^-$ (1.5)

Total reaction: $Li_{1-x}CoO_2 + CLi_x \rightarrow LiCoO_2 + C$ (1.6)

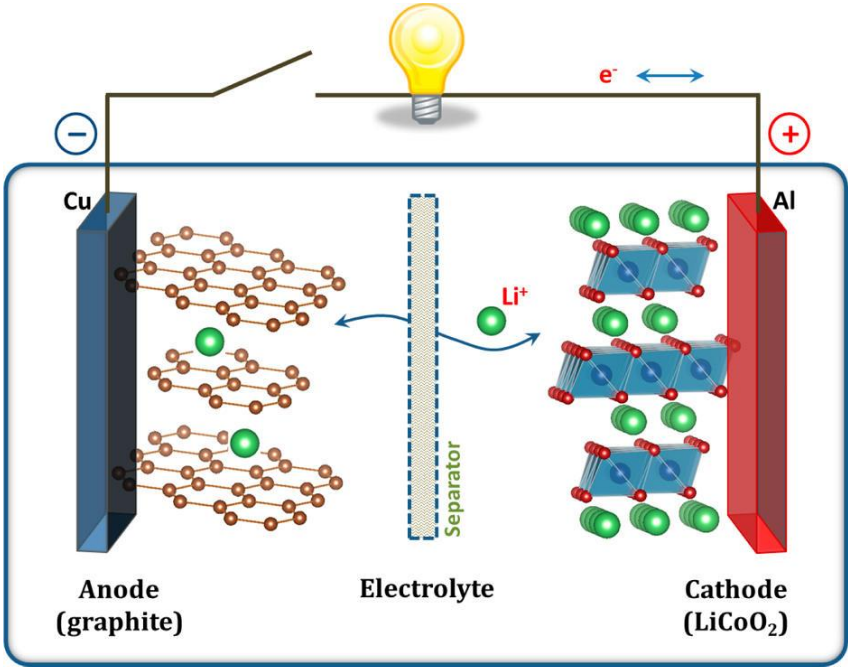

Figure 1.1 Scheme of the working principles of lithium-ion batteries[12]. Reprinted with permission from ref 12. Copyright 2013, American Chemical Society.

The battery components and the working principles of Na-ion batteries[9, 14], Mg batteries[16, 36], K-ion batteries[37-38], aqueous Zn batteries[39] and LIBs are basically the same except for their ion carriers. The intercalation chemistry with respect to cathode materials for Mg-ion, K-ion and Zn-ion, is very similar to that of lithium, makes it possible to apply similar compounds for these systems. However, there are some obvious differences between these systems, ions size, solvation energy and so on, which affects the phase stability, transport properties, and interphase formation, therefore to electrochemical performance.

1.3 State of the art of V_2O_5 as cathode material for different electrochemical energy storage systems

1.3.1 Structure, morphology, and synthesis of V_2O_5

Orthorhombic V_2O_5 (α-V_2O_5 $Pmn2_1$) is composed of [VO_5] square pyramids layers connected by sharing edges and corners and alternating in an up-up-down-down sequence with every third row being vacant[24, 40] (**Figure 1.2**). Three different oxygens atoms, O1, O2, and O3, exist in a single slab of V_2O_5 and a weak vanadium-oxygen interaction is responsible to the connection of adjacent V_2O_5 sheets, where the interlayer space is suitable for the guest ions intercalation. However, the orthorhombic structure of V_2O_5 can be addressed as distorted [VO_6] octahedral units as well[24, 41].

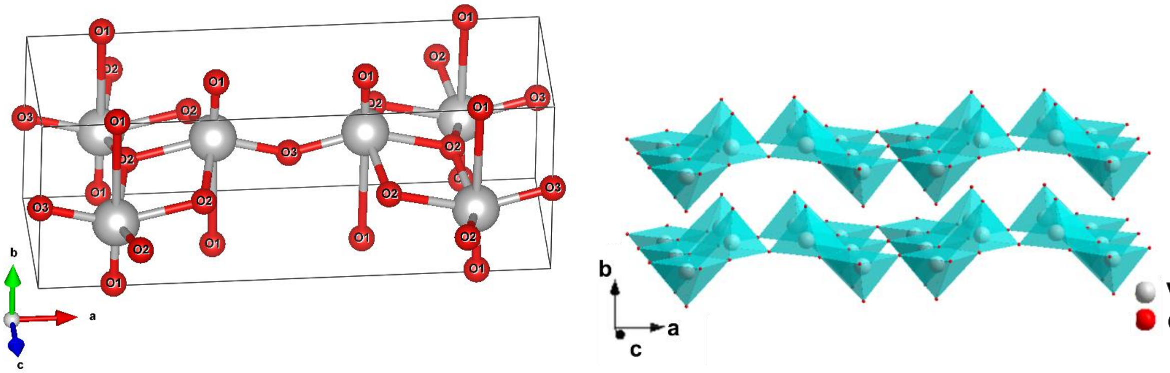

Figure 1.2 Crystal structure of orthorhombic V_2O_5 with space group $Pmn2_1$

Compared with bulk materials, nanostructured materials can tolerate much higher stresses before getting pulverized, which is beneficial to electrochemical performance (rate capability and cycling stability). Various kinds of nanostructured V_2O_5 cathode materials have been developed in the past decades, which showed much better performance than micron-sized or larger, and bulk V_2O_5 crystals in LIBs[23-24, 42-44]. Nanostructured V_2O_5 cathode materials can be typically classified into zero-dimensional (0D), one-dimensional (1D), two-dimensional (2D), three-dimensional (3D) nanomaterials[24, 42, 45], according to their nanoscaled property in different dimensions. 0D and 2D V_2O_5 nanostructure only have nanoparticles and nanosheets, respectively. While 1D V_2O_5 nanostructure includes nanorods, nanotubes, nanowires, nanofibers, and nanobelts, 3D V_2O_5 nanostructure covers the porous microspheres and microflower, hollow microspheres and microflower, as well as yolk-shell.

Various methods have been used to synthesize different nanostructured V_2O_5 materials, such as hydrothermal[46-53], electrospinning[54-56], solvothermal[57-60], thermal evaporation or pyrolysis[61-63], template-induced electrodeposition[64-65], sol-gel method[43, 66-67]. Among them, hydrothermal method is a very powerful approach to synthesize V_2O_5 nanowires. The electrospinning is a simple and versatile method for synthesizing the V_2O_5 nanowires. Hydrothermal and solvothermal methods have been extensively applied to synthesize V_2O_5 nanoparticles of 0D. However, some major problems, low-yield, safety issues, and expensive autoclaves, hinder the application of hydrothermal /solvothermal methods in scalable synthesis[45]. Thermal pyrolysis, for instance, flame spray pyrolysis, is a highly effective method for the scalable synthesis of V_2O_5 nanoparticles[63].

1.3.2 Working mechanism of V_2O_5 in Li- and Na-ion batteries

V_2O_5 is a typical intercalation material because of its layered structure. Being a promising cathode material, it has a very high theoretical capacity of 294 mAh g^{-1} and 442 mAh g^{-1} upon 2 and 3 Li^+ ions insertion per mole of V_2O_5, respectively[13, 43]. The structural evolution of orthorhombic V_2O_5 upon Li-ion intercalation/de-intercalation has been well investigated[15, 68-72]. During the Li-uptake, V_2O_5 goes through several phase transitions resulting in the formation of α-, ε-, δ-, γ-, and ω-phase. The α-phase is observed at $x < 0.1$ in $Li_xV_2O_5$, ε-phase exists in the range of $0.35 < x < 0.7$, while the δ-phase appears at $x = 1$ for $Li_xV_2O_5$. An irreversible transformation of δ-phase into γ-phase is observed when x is over 1, and the γ-phase can be reversibly cycled in the range of $0 \leq x \leq 2.0$ while maintaining the γ-type structure. The irreversible formation of ω-phase with a rocksalt-type structure takes place upon the third lithium insertion into the V_2O_5 structure. The orthorhombic α-, ε-, and δ-phases are composed of [VO_5] square pyramids layers with an increased puckering in the layers. The γ-phase also consists of [VO_5] square pyramids, but highly puckered and irreversible (metastable γ'-phase upon complete de-intercalation), while the ω-phase has a tetragonal structure, which is very different from the initial orthorhombic V_2O_5 phase. However, some authors suggested the co-existence of Li_xVO_2 and Li_3VO_4 compounds instead of the γ- and ω-phase.

Upon Na insertion into V_2O_5 the structure of pristine α-phase is maintained without significant changes in lattice parameters at low sodium amount ($x \leq 0.2$ in $Na_xV_2O_5$)[73]. In the range $0.2 \leq x \leq 1.6$, the insertion proceeds via solid solution mechanism with two different amplitudes: strong changes of lattice parameters in $0.2 \leq x \leq 0.7$ and only slight changes in $0.7 \leq x \leq 1.6$. The irreversible NaV_2O_5 phase is formed during the first Na insertion and the NaV_2O_5 phase can reversibly insert 0.8 sodium ions in the range of 1.4 V-3.0 V vs Na^+/Na. However, Ali and co-workers[74] proposed a different reaction mechanism. Two-phase mixture composed of a major phase NaV_2O_5 and a minor phase $Na_2V_2O_5$ were observed during the discharge process, where $Na_2V_2O_5$ phase exists in the presence of crystalline and amorphous-like phases. Upon charging process, it returns back to its original structure of V_2O_5 with a minor phase of NaV_2O_5. The detailed reaction mechanism of Na-ion insertion into V_2O_5 is still not clear so far.

1.3.3 Review of V_2O_5 Modification

Although V_2O_5 has many advantages of high capacity, abundant sources, low cost, and easy synthesis, making it a promising cathode material for next generation LIBs, its practical application has been retarded because of its low electronic conductivity (10^{-2} to 10^{-3} S cm^{-1})[41], low diffusion coefficient (10^{-12} to 10^{-13} cm^2 s^{-1})[41, 75] and the dissolution of V_2O_5 into electrolyte[76-77], causing poor cycling stability of this material. In order to solve these problems and improve the electrochemical performance of V_2O_5, numerous efforts and progress have been accomplished, such as the synthesis of nanostructured materials, heterogeneous structures (including surface coating, composites), and cation doping. Below, some of these strategies are described.

a) *Nanostructured V_2O_5*. Numerous nanostructured V_2O_5 materials were synthesized to improve the electrochemical performance, including cycling stability and rate capability. The nanostructures forms of V_2O_5 include zero-dimensional (0D) nanoparticles[63, 78], one-dimensional (1D) nanowires/nanobelts/nanotubes[56, 79-89]/nanorods[65, 90-91], and two-dimensional (2D) nanosheets[92-96], as well as three-dimensional (3D) hierarchical architectures, such as porous microspheres[97-100], yolk-shell[62, 101-102], and (hollow) microflowers[103-104], as well as hollow microspheres[105-109]. It is well known that nano-sized materials provide short diffusion lengths for cation insertion and facilitate the transport kinetics of electrons, resulting in higher capacities[110-111]. The small particle size and the large specific area increase the contact area between electrode and electrolyte, which is beneficial for rate capability[110, 112].

b) *Heterogeneous structures*. Heterogeneous structured materials consisting of multi-nanocomponents, surface coated materials and composites, are currently regarded as very promising materials for the development of electrochemical energy storage, due to their synergic properties, which arise from the integration of multi-nanocomponents, each tailored to satisfy a different requirement, such as high conductivity and high energy density, as well as outstanding mechanical stability[113]. The surface structure of electrode materials is known to affect significantly the electrochemical performance of LIBs. Surface coating has proven to be a very effective approach to improve the cycling stability and rate capability of electrode materials[114]. Carbon[115-

[117], rGO[118] and conducting polymers[119-121], as well as inorganic coating of TiO_2[122] and SiO_2[123], have been used to improve the performance of V_2O_5 materials. Moreover, composite based on V_2O_5 and rGO[124-127]/CNT[128-133] or polymer[67, 134-137] can also be used to achieve high rate capability and long cycle in LIBs.

Both surface coating and mixing with carbon nanotubes, rGO or polymers provide several benefits to V_2O_5 electrodes, such as (i) enhancing the electric conductivity and facilitating the charge transfer on the surface of V_2O_5 particles; (ii) suppressing the aggregation and serving as a buffer to alleviate the volume changes for active materials. In addition, the surface coating could also offer a physical protection barrier and a modification of the surface chemistry that improves the chemical stability of the material. Meanwhile, it can also prevent the collapse and crush of the V_2O_5 along with repeated cycling under harsh application condition[24].

c) *Cation doping*. Structure and electronic state of electrode materials can be greatly influenced by the doping. Recently, tremendous work has been focused on the doping of V_2O_5 nanostructure with various elements, such as Na[138], Mg[139], Al[140], Fe[141-142], Ti[143-144], Ni[105], Mn[145-146], Cr[147-149], Cu[150-151], Nb[152], Ag[153-155], Y[156], and Sn[157-158], to overcome the capacity fading and improve the rate capability. Some very distinct properties can be seen in the doped V_2O_5 electrodes: (1) cations doping results in increased electronic conductivity because of the formation of lower oxidation state of V (V^{3+} and V^{4+}); (2) cations doping into the V_2O_5 layers leads to the formation of [MO_6] octahedral units that can stabilize the layer structure of V_2O_5 during cycling; (3) cations doping can facilitate the charge transfer; (4) cations doping may reduce the particles size and alter the morphology, improving the electrochemical performance of V_2O_5[24, 159]. However, the excess of dopant may block the pathway for the inserted ions and inactive dopant could reduce the usage of active materials, thus reducing the capacity of the materials. Moreover, impurity or second phase might be induced with excess of doping cations as well, which might, in turn, have a negative effect on the electrochemical performance of materials.

Since in case of doping (like especially for semiconductors), the degree of the doping level is well below 0.1%. Doping has no significant influence on the (non-local) underlying structure. "Doping" is quite common for battery materials research even if the dopants concentrations are high and cause structural modifications. One should note the "doping" is not accurate or appropriate enough to describe such cases. It is a great challenge concerning the specific "wording" like this and "doping" is still used in this thesis.

1.3.4 V_2O_5 as cathode material for Mg, K-ion, and aqueous Zn batteries

Magnesium batteries (MBs) have been considered as a potential candidate for the large-scale EESs, owing to the abundant resources, lower cost, and high theoretical volumetric capacity (3833 mAh cm^{-3}) of magnesium, as well as higher safety of Mg-metal comparing to Li[1, 16, 160-161]. Despite the recent progress in MBs, there are many challenges to be overcome before their commercial application. One of the major issues is the sluggish diffusion of Mg ions in host structure[162-164]. The second major issue is the lacking of appropriate electrolytes and cathode materials[165-166]. V_2O_5 is exceedingly attractive as cathode material for MBs, owing to its proven high theoretical capacity and high working voltage in LIBs. However, up to now, only limited capacities have been obtained with V_2O_5 in MBs. For example, Tang et al.[26] reported that aero-gel V_2O_5 cathode delivers a discharge capacity of 180 mAh g^{-1}, which is dominated by the surface morphology, such as thin and mesoporous solid phase. Yu and Zhang[167] reported that in $Mg(ClO_4)_2$/propylene carbonate (PC) electrolyte, the electrochemical property of V_2O_5 depends on the H_2O level of the electrolyte, which exhibited the highest 1st discharge capacity of 158.6 mAh g^{-1} in 1 M $Mg(ClO_4)_2$+1.79 M H_2O/PC electrolyte. A high initial discharge capacity of 218 mAh g^{-1} is reported for VO_x nanotube cathode in $Mg(ClO_4)_2$/acetonitrile electrolyte by Kim et al.[168]. A metastable ζ-V_2O_5 (space group *C*2/*m*) cathode was reported by Andrews and co-workers[169], delivering a first discharge capacity 140 mAh g^{-1} and maintaining a discharge capacity of 90 mAh g^{-1} up to 100 cycles. The V_2O_5 nanoclusters/porous carbon composite was demonstrated to deliver an initial capacity of 300 mAh g^{-1} within working potential of 0.5 - 2.8 V vs. Mg^{2+}/Mg [170]. Gershinsky and co-authors[171] reported a V_2O_5 thin film that delivered a reversible capacity of ~ 150 mAh g^{-1} in the potential range of 2.2 - 3.0 V vs. Mg^{2+}/Mg. In the same work[171], *ex situ* XRD demonstrated that the intensity of reflections of V_2O_5 film material became weak and the main reflection 010 shifted to lower angle. However, a detailed investigation of structural changes of V_2O_5 upon Mg-ion insertion/extraction is still missing.

KIB, which has a similar working principle of “rocking chair” with LIBs, is another promising candidate for the large-scale EESs because of the high abundance and low cost of Potassium. K-ion is larger and heavier that Li^+ and Na^+, but K^+/K couple has a lower standard electrode potential (-2.936 V vs. SHE) than that of Na^+/Na (-2.714 V vs. SHE)[38]. Due to the lower desolvation energy and the smaller size of the solvated ion than that of Li- and Na-ion, K-ion displays a lower ion-solvent interaction, resulting in fast diffusion kinetic and high rate capability of KIBs[172]. Whereas the expensive Cu is usually applied as an anode current collector for Li-ion batteries, more affordable Al can be used as current collector in both NIBs and KIBs at low potential, where a Li alloy with Al would happen[173-174]. Although KIBs are very promising for large-scale EESs, KIBs are still in their infancy and face large challenges to develop electrode materials for their commercial application. Until now, only limited number of the original works on the anode and cathode materials for KIBs along with several reviews[14, 21-22, 38, 175] have been reported, such as carbon-based materials[176-183], Titanium-based materials[184-187], layered metal oxide[188-192], Prussian-based materials[193-198], Olivine[199], metal sulfide materials[200-202], alloying anode[203-205], organic compounds[206], as well as vanadium-based materials[207-214]. Among them, vanadium oxides are very promising for the cathode materials. Recently, Clites and coworkers[212] reported that δ-$K_xV_2O_5{\cdot}nH_2O$ cathode with interlayer spacing of 9.65 Å in KIBs showed a high electrochemical performance with initial discharge capacity of 268 mAh g^{-1} at C/50 and 226 mAh g^{-1} at C/15 rate in the voltage range of 2.0 - 4.3 V vs. K^+/K. Layered $K_{0.5}V_2O_5$ investigated by Deng et al.[213] delivered a reversible capacity of 90 mAh g^{-1} at current density of 10 mA g^{-1} and a high capacity retention of 81% within 250 cycles at 100 mA g^{-1} in the potential range of 1.5 -3.8 V vs. K^+/K. *Ex situ* XRD and XPS demonstrated high reversibility of structural transformation during K-ions insertion/extraction. Jin et al.[214] reported that a V_2O_3/carbon composite delivers a capacity of 240 mAh g^{-1} at current density of 50 mA g^{-1} with a high capacity retention of 95.8% after 500 cycles 0.01 - 3.0 V vs. K^+/K. The composite was shown to operate via a pseudocapacitive mechanism upon K ion insertion. Moreover, ab initio molecular dynamics and first-principle calculation demonstrated that V_2O_3 structure can only uptake up to 1 mol K-ion to form KV_2O_3, and the K-ion lies on the 6e sites in KV_2O_3 structure. Liu et al.[208] reported a layered $K_{0.23}V_2O_5$ anode material, which delivers a discharge capacity of 121.6 mAh g^{-1} within 150 cycles at 20 mA g^{-1}. Zhu et al.[211] reported a bilayered δ-$K_{0.51}V_2O_5$ cathode, which shows a high capacity of 131 mAh g^{-1} with excellent rate capability and a high average voltage of 3.2 V. A $V_2O_5{\cdot}0.6H_2O$ xerogel cathode was reported by Tian et al.[209]. This material delivers an initial discharge capacity of 224.4 mAh g^{-1} at 50 mA g^{-1} with a discharge capacity of 103 mAh g^{-1} after 500 cycles 1.5 - 4.0 V vs. K^+/K, while crystalline V_2O_5 only displays a discharge capacity of 44.3 mAh g^{-1} at 50 mA g^{-1}. Very recently, amorphous V_2O_5 /carbon nanotube sponge was reported by Ye and coauthors[210], which exhibited an initial discharge capacity of 206 mAh g^{-1} at 5 mA g^{-1}. However, a detailed investigation related to the structural changes of V_2O_5 upon K-ion insertion/extraction is still missing.

The aqueous ZBs have numerous advantages comparing to non-aqueous LIBs, NIBs, MBs and KIBs[19, 215]. The metallic zinc is an attractive anode. Metallic Zn has a high specific capacity of 820 mAh g^{-1} and high volumetric capacity of 5854 mAh cm^{-3}. The high potential for hydrogen evolution of Zn (-0.76 V vs. SHE) makes it stable in water[216]. The manufacturing costs of ZBs are expected to be low since water-based electrolyte are nontoxic, inflammable and do not require strict humidity control during cells assembling[217-218]. Compared with non-aqueous electrolyte (about 1^{-10} mS cm^{-1}), the ionic conductivity of the aqueous electrolyte (up to 1 S cm^{-1}) is much higher, resulting in a higher rate capability[19]. The utilization of aqueous electrolytes can lower the activation energy for charge transfer at the electrode/electrolyte interface. To date, several cathode materials for aqueous ZBs have been proposed, like the polymorphs of manganese oxide (α-MnO_2, β-MnO_2, γ-MnO_2, δ-MnO_2, spinel-MnO_2 and so on)[218-230], Prussian blue analogues (CuHCF and ZnHCF)[231-234], vanadium-based oxides ($Ca_{0.25}V_2O_5{\cdot}nH_2O$, $Zn_{0.25}V_2O_5{\cdot}nH_2O$, $Na_{0.33}V_2O_5$, $V_2O_5{\cdot}nH_2O$, LiV_3O_8, $H_2V_3O_8$, and so on)[215-216, 235-251], and other compounds such as $Na_3V_2(PO_4)_3$[121], $Na_3V_2(PO_4)_2F_3$[252], VS_2[253], Mo_6S_8[254], $ZnMn_2O_4$[255-256], and some organic compounds[257-258]. Among them, vanadium-based oxides with open framework show high potential. For example, $Zn_{0.25}V_2O_5{\cdot}nH_2O$ cathode reported by Kundu et al.[216] delivers an initial discharge/charge capacity of 282/278 mAh g^{-1} at C/6 rate with excellent rate capability and the high capacity retention of 80% after 1000 cycles at 15 C rate (278 mAh g^{-1}). Xia et al.[242] demonstrated high capacity of 367.1 mA h g^{-1} at 100 mA $g^{-1}$for $Na_{0.33}V_2O_5$ nanowire cathode. This material exhibits good capacity retention of 93% after 1000 cycles and good rate capability. $H_2V_3O_8$/graphene composite was investigated by Pang et al.[247], which displays a capacity of 394 mA h g^{-1} at C/3 and excellent cycling stability with capacity retention of 87% over 2000 cycles, as well as high rate capability. Recently, Zhou and co-authors[259] reported that V_2O_5 cathode shows high performance in 3 M $ZnSO_4$ electrolyte compared with different concentration and in other types of salts like $Zn(NO_3)_2$, $Zn(CH_3COO)_2$, and $ZnCl_2$. In 3 M $ZnSO_4$, V_2O_5 delivers a high capacity of 224 mAh g^{-1} at 100 mA g^{-1} and good cycling stability at the high current density of 1 and 2 A g^{-1}, respectively. *Ex situ* XRD demonstrated the formation of a new phase of $Zn_xV_2O_5$ upon Zn insertion into V_2O_5. Zhang et al.[260] also reported V_2O_5 cathode material with a capacity of 470 mAh g^{-1} at 0.2 A g^{-1} and high capacity retention of 91.1% after 4000 cycles at 5 A g^{-1} in 3

M $Zn(CF_3SO_3)_2$ electrolyte. It can also work well in extreme conditions at both high (50 ^oC) and low (-10 ^oC) temperatures. Hydrated Zn ions co-intercalation into V_2O_5 crystal structure was proposed as well based on the *ex situ* XRD, XPS, and TEM experiments. However, a detailed investigation of the structural changes of V_2O_5 upon Zn-ion insertion/extraction is still missing.

1.4 Aim and objectives of the thesis

The development of "beyond-lithium" rechargeable batteries for the application in large-scale EESs is an important topic today. However, all promising candidates mentioned above, MBs, KIBs, and aqueous ZBs, for next-generation rechargeable batteries are still in their early stage. New electrodes materials with high capacity, high voltage, and long cycle life are required. V_2O_5 is a promising cathode for different non-lithium systems. The high performance for such systems has been already reported, but the structural aspects of insertion for the cations others than lithium are not yet studied. In the present thesis, we concentrate on the study of mechanism reaction, via *in operando* techniques, of V_2O_5 upon Mg^{2+}, K^+, and Zn^{2+} insertion/extraction in MBs, KIBs, and aqueous ZBs, as well as its electrochemical properties in the three different systems, respectively. Additionally, M-doped V_2O_5 (M=Mn, Fe, and Ni) materials were prepared and the substitutional or interstitial cation doping in the M-V_2O_5 materials was investigated through several characterization methods. Finally, other related works performed during my PhD study are briefly reviewed and summarized.

The research objectives of the thesis are the following:

1) to synthesize crystallized orthorhombic nanostructured V_2O_5 nanowires via a hydrothermal method and to investigate the electrochemical performance and the reaction mechanism of V_2O_5 cathode upon Mg^{2+}, K^+, and Zn^{2+} insertion/extraction in MBs, KIBs, and aqueous ZBs, respectively, through *in operando* synchrotron diffraction and *in operando* XAS. In addition, *ex situ* techniques, such as Raman, X-ray photoelectron spectroscopy, and TEM are also used as assistant approaches for the storage mechanism study.

2) to determine the preferred positions where the M doping cation (M= Mn, Fe, and Ni) locates in the doped V_2O_5 samples

Chapter 2 Fundamentals of *in operando* synchrotron diffraction and *in operando* X-ray absorption spectroscopy study for rechargeable batteries

2.1 Introduction

Recent years, rechargeable batteries with high energy density, greater cycle life and safety characteristics are strongly required to realize the usage to electrical vehicles and grid energy storage. To meet these demands, great efforts have been done on developing promising new materials, materials modification, and new chemistry for the next generation rechargeable batteries. Electrode materials such as composition, structure and morphology, etc. are the key of rechargeable batteries, which decide the electrochemical performance and cost. The structure of electrode materials undergoes continuous evolution during cycling in the battery. It is very important to better understand the correlation between the structure evolution of the materials in "real time" and electrochemical performance during cycling, which can be used to improve the performance and guide the development and application of new materials with high performance[30, 261].

However, it is difficult to understand the reaction mechanism because of the inherently complexity of battery systems. It requires systematic and deep study on many aspects such as chemical compositions, physical properties, crystal structures, microstructures, and electron structures of battery materials, as well as their evolution during cycling. Synchrotron X-ray techniques was started to study of battery materials since about 25 years ago pioneered by Mcbreen et al.[32, 262-265] and have been widely used to understand the fundamental mechanism of battery materials[29-30, 33, 261]. The merits of synchrotron radiation, such as extremely bright, high flux, and high-energy, highly collimated and energy tuneable, allow the applications in battery science and technology. The tunability of synchrotron energies makes the conduct of experiments that require a continuous beam energy (e.g. XAS). It allows the optimization of the experiments to improve the quality of data via optimizing the beam energy, such as eliminating fluorescence artifacts during XRD measurement. It also allows the conduct of high temporal resolution (up to milliseconds) studies of the electrochemical/chemical reaction and high spatial resolution spectroscopic mapping and imaging of electrodes. Especially, the ultrahigh intense and penetration property of synchrotron radiation makes the *in operando* investigation of battery systems possible and easier to realize. *Ex situ* and *in operando* techniques have been widely used to elucidate the scientific and technological problems of rechargeable batteries. Compared to *ex situ* measurements, *in operando* techniques can provide direct information on the system in a non-equilibrium state and “real-time study”-time-dependent reaction, allowing a reliable visualization of real-reaction during the electrochemical reduction and oxidation processes, as already described in the Introduction of Chapter 1 (1.1 Background).

Synchrotron-based techniques, *in operando* synchrotron powder diffraction and *in operando* X-ray absorption spectroscopy (XAS), are very powerful and high-efficiency tools and approaches to uncover the evolution of crystal structure and the local structure and oxidation state of the materials during the electrochemical cycling. Both *in operando* techniques will be briefly discussed in this chapter, including the synchrotron light source and *in operando* setup used during electrochemical processes.

2.2 Synchrotron light source

Synchrotron radiation is based on an important theorem of classical electrodynamics and electromagnetic radiation emitted when charged particles are accelerated radially, i.e., when they are subject to an acceleration perpendicular to their velocity ($a \perp v$). It is produced, for example, in synchrotrons using bending magnets, undulators and/or wigglers. In a synchrotron facility, bunches of electrons are filled and accelerated to a final energy of about 1.5−8 GeV, close to the speed of light, and maintain at a fixed energy in the storage ring.

The ALBA-CELLS synchrotron[266] is a 3rd generation Synchrotron Light facility located in Cerdanyola del Vallès, (Barcelona), being the newest source in the Mediterranean area. Machine and beamline commissioning started at the end of 2010 and in mid 2011, respectively. The first official users started in May 2012. ALBA currently operates eight beamlines from soft X-ray energies to hard X-Ray energies. The machine is composed of a 268 m circumference storage ring with electrons accelerated to 3 GeV and with small emittance (4.8 nm rad). The electron current in the ring is now 150 mA.

The Material Science Powder Diffraction (MSPD)[266] beamline has a superconducting wiggler as an insertion device and it operates at energies between 8 and 50 keV. The effective X-ray source size and flux at the energy of 30 keV are 620 x 85 μm^2 and 1 x 10^{14} ph/s/0.1%bw within a 300 x 125 μrad^2 aperture, respectively. All technical properties of the MSPD beamline are given in **Table 2.1**.

Table 2.1 Technical Specifications of MSPD beamline

Photon Energy Range	8 – 50 keV
Flux at sample	~ $4 \cdot 10^{12}$ ph/s
Energy resolution	$2 \cdot 10^{-4}$
Beam size at sample	variable: 1.5 x 5 mm^2 to 0.015 x 0.015 mm^2
Photon source size (FWHM)	0.65 x 0.1 mm^2 (HxV)
Photon source div. (FWHM)	1.4 x 0.18 $mrad^2$ (HxV)
Insertion Device (ID)	Superconducting Wiggler SCW31
Monochromator	Si(111) Double Crystal with long 2nd crystal

PETRA III[267] is a large 3rd generation synchrotron radiation with 2.3 km circumference at DESY, Hamburg. It is the worldwide most brilliant storage ring based X-ray sources for high energy photons providing a brilliance exceeding 10^{21} ph/(s mm^2 $mrad^2$ 0.1% BW). It operates at 6 GeV particle energy at 100 mA beam current in top-up mode keeping the photon flux stable with 1%. The beamlines at PETRA III are distributed over three experimental halls, including the largest, 300 m long experimental hall ‘Max von Laue’ and the ‘Paul P. Ewald’ and the ‘Ada Yonath’ halls.

P65 is a new X-ray Absorption Fine Structure (XAFS) spectroscopy beamline at the high brilliance storage ring PETRA located in experimental hall ‘Paul P. Ewald’, in Hamburg, Germany[268-269].**Table 2.2** gives all the technical properties of the P65 beamline. The P65 beamline provides a relatively large beam (0.5x1 mm2) and a moderate photon flux density. The 11 period undulator delivers a maximum monochromatic photon flux of $2*10^{12}$ s^{-1} at 9 keV and more than 10^{11} s^{-1} at the higher end of the working range. Two plane mirrors with variable angle of incidence and three different surface coatings are installed in front of the water cooled double crystal monochromator (DCM). They reduce the power load density on the first DCM crystal and effectively suppress the contamination of the monochromatic X-ray beam with higher harmonics radiation. The main factor for the very high stability of the beam position on the sample is the short distance of only 5 m between the DCM and the sample position. The beamline design is optimised for standard EXAFS measurements with transmission and fluorescence mode under *ex situ* and *in operando* conditions.

Table 2.2 Technical Specifications of P65 beamline, PETRA III

Source	Mini-undulator (11 periods)
Photon Energy Range	4 – 44 keV
Accessible Elements	K-edges: Ca – Nd, L-edges: Sb - Uuo
Beam size at sample	0.5 x 1 mm^2 (vert x hor)
Photon flux at Sample	> 10^{11} – 10^{12} s^{-1}
Detectors	Energy dispersive 7 pixel HPGe detector, Si-PIPS diodes
Methods	X-ray absorption spectroscopy in transmission and fluorescence mode
Monochromator	Crystals: Si(111), Si(311)

2.3 *In operando* setup used at synchrotron beamline

2.3.1 *In operando* coin cell holder

In operando study of battery electrodes requires cell housings with a well defined electrolyte volume, chemically inert materials, air tightness and low background contributions to the scattered intensity. For example, dead volume inside the cell should be avoided to prevent migration of the electrolyte or other electrochemically formed compounds, which consequently leads to capacity losses as well demonstrated for Li–S systems[270].

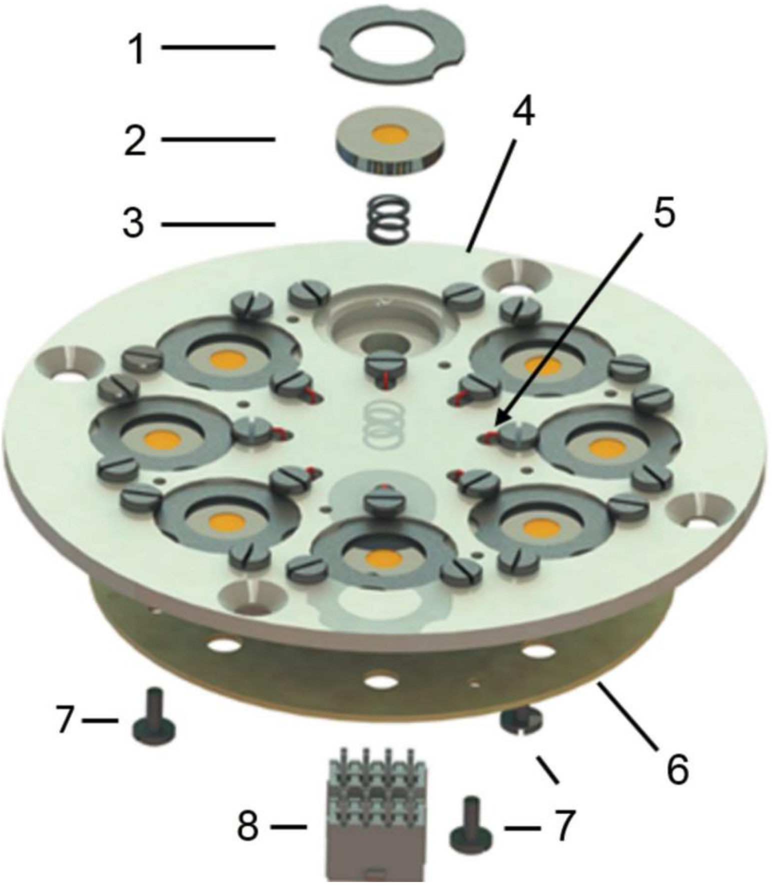

Figure 2.1 *In operando* battery holder for eight coin cells: (1) metallic cap; (2) in situ coin cell with Kapton windows; (3) metallic helical spring; (4) nonconductive sample holder, e.g. made of POM; (5) wire to connect metallic cap with PCB; (6) PCB; (7) screws to fix PCB to sample holder; (8) 2 x MOLEX eight-pole connector (designed holder from our previous work[28])

In operando coin cell holder is used from previous designed work in our group[28] and its schematic drawing is displayed in **Figure 2.1**. The holder consists of two main parts, a coin cell holder and a printed circuit board (PCB). The coin cell holder is made of an isolating rigid material, such as POM (polyoxymethylene). The coin cells are mounted in concentrically arranged slots (Ø = 20.6 mm, depth = 5.0 mm). A helical spring (Ø = 9.5 mm) is positioned within a hole to ensure the electrical contact of the coin cell with certain positioning. This enables the investigation of coin cells with different thicknesses t, such as CR2025 (t = 2.5 mm) or CR2032 (t = 3.2 mm). The electrical contact of the active electrodes is realized by the metallic caps, which are connected to a rearward mounted PCB by a screw and a wire. **Figure 2.2** shows the conducting paths of the PCB.

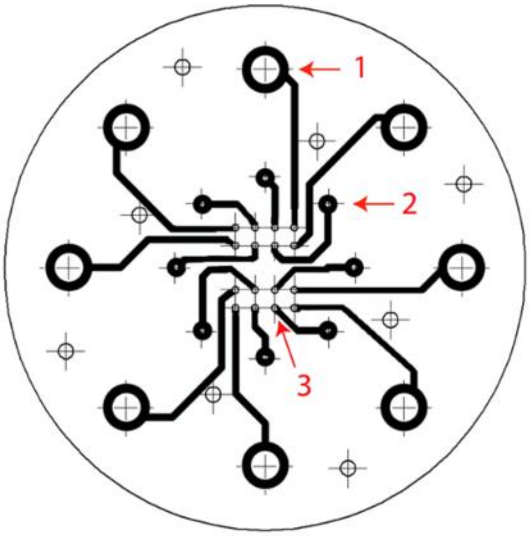

Figure 2.2 Detailed view of the PCB – printed circuit board: 1: conducting pads for the helical spring (Figure 2.1, item 3); 2: conducting pads for wire from metallic cap (Figure 2.1, item 1 and 5); 3: conducting pads for the MOLEX - connector (Figure 2.1, item 8).

Figure 2.3 presents the detailed schematic drawing of the *in operando* coin cell and a cross section of the coin cell holder[28]. All 16 poles conduct their electrical signals to the centre. The connection to the potentiostat is realized by two MOLEX eight-pole connectors and a flexible 16-wire cord attached to the centre of the holder. A concentric rotation of the holder is realized by a stepper motor. With this design, disturbance of the beam path by the wiring is avoided.

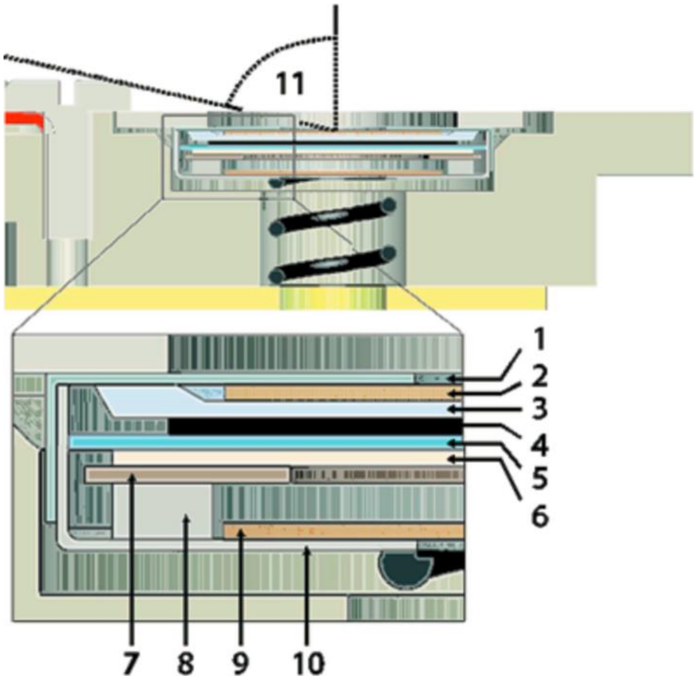

Figure 2.3 Schematic cross section of the holder with a detailed view of an in situ coin cell: (1) and (10) stainless steel coin cell housing with 4–5 mm hole; (2) and (9) Kapton foil/glass window (Ø: 8 mm); (3) and (4) current collector and active electrode (Ø: 12 mm); (5) separator with electrolyte (Ø: 17 mm); (6) Li/Na/K foil (Ø: 16 mm); (7) stainless steel spacer with 6 mm hole; (8) stainless steel wave spring; (11) maximum 2θ at 70º (designed coin cell from our previous work[28])

2.3.2 Setup at the MSPD beamline at ALBA and P65 beamline at DESY

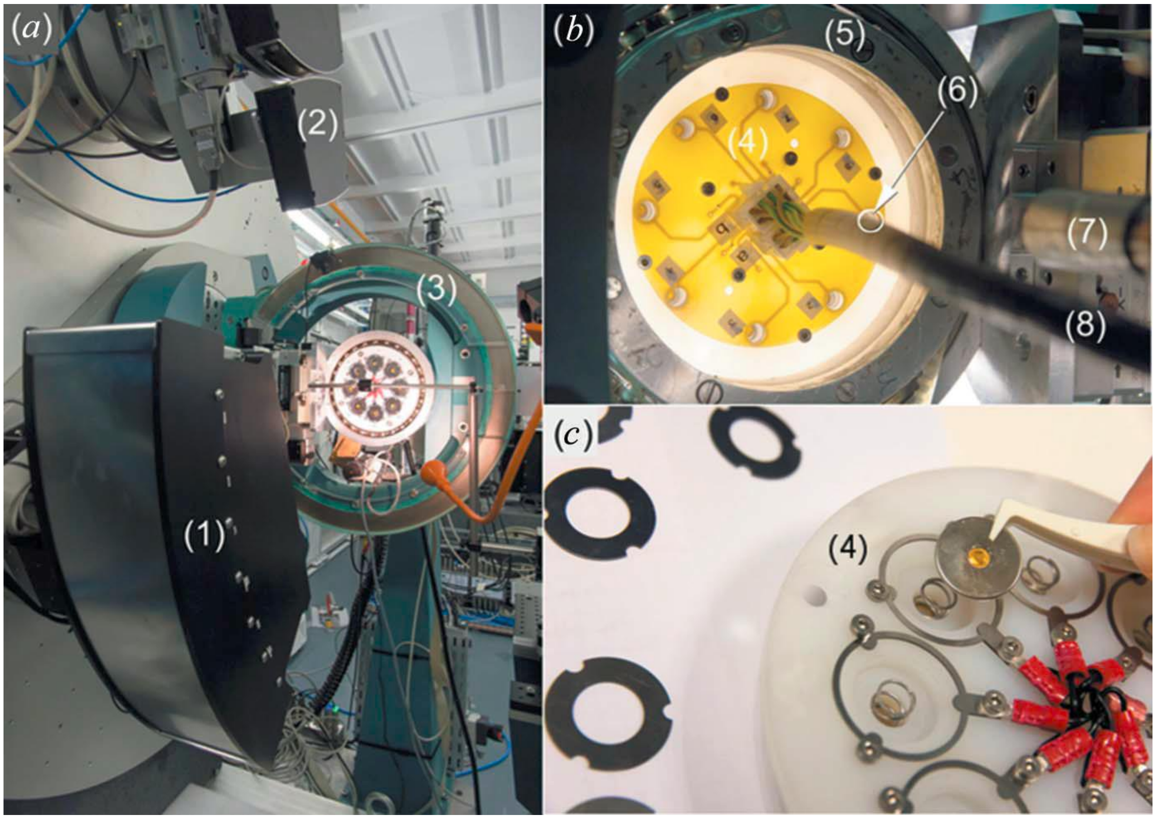

Figure 2.4 Photographs of the in situ coin cell holder installed at the MSPD beamline of the new synchrotron light source CELLS-ALBA for transmission diffraction experiments: (a) overview in downstream direction; (b) detailed view in upstream direction; (c) assembly of the coin cells. Marked parts: (1) six-module Mythen detector; (2) MAD26 high-resolution detector; (3) Eulerian cradle; (4) PCB; (5) ball bearing with stepper motor; (6) position exposed to the synchrotron beam; (7) synchrotron beam pipe; (8) 16-wire cord with MOLEX connector.

In operando synchrotron diffraction with transmission mode were performed at the MSPD beamline of the Spanish synchrotron light source ALBA in Barcelona[266]. **Figure 2.4** displays Photographs of the setup adjusted to the beamline. The holder was mounted onto a rotatable frame, which was accessed by a stepper motor allowing a sequential positioning and a consecutive measurement of each cell. A Mythen 6K detector is used to collect the diffraction data. In order to improve the powder averaging (increasing the number of crystallites contribution), the coin cells continuously oscillated +/-5 º around the incoming beam direction. Date with exposure times of

40 s per pattern can give sufficient statistics in intensity over angular range of 1.8° - 42° in 2theta, resulting in a measurement repetition time of about 360 s for each sample position. This time frame provides sufficient data points to track all structural changes of the sample when the measurement time is carried out with C/5 (meaning 5 h for full charging or discharging) or slower. In the case with high current/rate, either the exposure time or the number of samples has to be decreased to get enough efficient data points.

In operando XAS measurements were performed at synchrotron beamline P65 at PETRA III (DESY, Hamburg). The galvanostatic charge and discharge cycle was performed at C/14 rate in 2025-type coin cells with 5mm-diameter Kapton window. XAS spectra of Vanadium were recorded in quick-XAS (6 min/spectrum) mode in fluorescence geometry using PIPS (passivated implanted planar silicon) diode.

Chapter 3 *In operando* study of orthorhombic V_2O_5 as cathode material for rechargeable Mg batteries

3.1 Introduction

Rechargeable magnesium batteries (MBs) have been regarded to be a very promising alternative on the application of large-scale EESs[1, 16, 160-161], due to their remarkable advantages, such as the low cost, and high volumetric capacity (3833 mAh cm^{-3}) of magnesium, as well as high safety upon cycling when applying Mg-metal. In the 1980s, Gregory and coauthors[271] initiated the workable rechargeable battery system with Mg anode and the electrolyte solutions composed of Mg-organo-borate moieties and tetrahydrofuran $Mg(BBu_2Ph_2)_2$/THF. Their work can be regarded as the 1st breakthrough in the field of MBs. Although this electrolyte allowed the reversible deposition and dissolution of Mg metal, its electrochemical window was too narrow (< 2 V). The second breakthrough was done by Aurbach and co-workers[162] in 2000, who presented novel electrolyte solutions made of the reaction product of R_2Mg Lewis base and $AlCl_{3-n}R_n$ Lewis acid in ethers (Glymes or THF). The prototype reversible rechargeable MB constructed from $Mg(AlCl_2BuEt)_2$ electrolyte and Chevrel phase Mo_6S_8 cathode, as well as Mg metal anode, was demonstrated. This MB showed high capacity retention, very low self-discharge, and excellent cycle life, with more than 3500 cycles, along with a wide temperature operating range. A few years later, Aurbach and coauthors[272] developed a new advanced electrolyte with a wide electrochemical window (>3 V), the all-phenyl-complex (APC) electrolyte. Despite the great progress in MBs, it is still big challenging to commercialize them. One of the major issues is the lack of appropriate cathode materials and compatible electrolytes for high-voltage cathodes and Mg. In addition, the reported Mg-ion electrolytes cause high corrosion of the current collectors and battery casing. For example, the known APC electrolyte shows strong corrosion to stainless steel above 2 V vs Mg^{2+}/Mg[273]. The sluggish Mg-ion solid diffusion related to Mg^{2+} also limited the development of cathode materials. The electrochemical performance of Mg-insertion cathodes could be improved by using nanomaterials, open tunnel structures or employing layered materials[23-24, 43-44, 274].

Because of their known high capacity and high working voltage for LIBs, vanadium oxide materials (V_2O_5) are extremely attractive on the application of MBs. However, only limited capacities have been obtained so far for V_2O_5 material in MBs and a detailed study of crystal structural evolution upon Mg-ion insertion/extraction into/from V_2O_5 is still missing.

As far as we know, *in operando* techniques, namely, *in operando* synchrotron diffraction and *in operando* X-ray absorption spectroscopy (XAS), have not yet been employed to probe the detailed storage mechanism of V_2O_5 materials in MBs. In this chapter, two strategies are proposed to enhance the electrochemistry of V_2O_5 cathode and to investigate the reaction mechanism during cycling: (**i**) to synthesize nanostructured V_2O_5 materials. According to the first-principles calculations, the diffusion barrier of Mg^{2+} in single layered V_2O_5 is reduced to 0.20 eV [275] comparing to the hopping barrier of 1.26 eV for Mg^{2+} in bulk V_2O_5[276-277], which is about 3 times higher than that of Li^+ ions (0.35 eV). Moreover, nanostructured materials offer short diffusion pathway for guest ions insertion, leading to higher capacity and higher rate capability in comparison to analogous bulk materials. In fact, various nanostructured V_2O_5 cathode materials were reported to exhibit a superior electrochemical properties comparing to microsized materials thanks to their short Mg-ion pathways and high specific reaction areas[160, 168-170, 278]; (**ii**) to design a cell-configuration system within a selected "standard" electrolyte. As reported in literature[271, 279-280], a passivation film is formed on the surface of metallic magnesium when using the standard combinations of salts and organic solvents, such as $Mg(SO_3CF_3)_2$ and $Mg(ClO_4)_2$, in carbonates and nitriles, respectively. The APC electrolyte developed by Aurbach et al.[272] has a wide electrochemical window ~3.3 V vs. Mg^{2+}/Mg, but it cause corrosion the stainless steel, which constitutes the cell casing, above 2.0 V for V_2O_5. Because of the incompatibility of Mg metal with "standard" electrolyte, Mg anode cannot be applied. We constructed a cell configuration with V_2O_5 nanowires as cathode in 1 M $Mg(ClO_4)_2$ in acetonitrile (AN) electrolyte together with $Mg_xMo_6S_8$ (x~2) anode. The storage mechanism, including crystal structure changes, oxidation state and local structural changes was elucidated by *in operando* synchrotron diffraction and *in operando* X-ray absorption spectroscopy (XAS).

3.2 Experimental

Synthesis of V_2O_5 nanowires: The V_2O_5 nanowires were synthesized via a modified hydrothermal method as reported in literature[281]. Typically, 1.0 ml of 2 M HCl, 0.3 g of ammonium metavanadate (NH_4VO_3), and 0.5 g of surfactant P123 ($EO_{20}PO_{70}EO_{20}$, where EO and PO represent ethylene oxide and propylene oxide, respectively) were mixed into 30 ml of deionized water under ultrasonication for 10 mins and stirring for 1 h. After that, the mixed solution was transferred to 50ml Teflon-lined autoclave and maintained at 120 ^{o}C for 24 h in an oven. The resulting precipitates were filtered and washed with water and acetone several times, then dried under vacuum at 120 ^{o}C for 24 h. The product was annealed at 400 ^{o}C for 2 h in air with a heating rate of 10 ^{o}C/min.

***Synthesis of Mo_6S_8*:** Mo_6S_8 was synthesized according to the reported work[282]. The $Cu_2Mo_6S_8$ was synthesized through a molten salt synthesis using KCl as salt. Typically, CuS (0.398 g), Mo (0.602 g), MoS_2 (1 g), and KCl (2 g) were ground in the glovebox and annealed in an alumina crucible under argon atmosphere. The mixtures were kept at 850 ^{o}C for 60h with a heating rate of 150 ^{o}C/h and then the furnace was cooled down to room temperature. The products were washed two times with hot distilled water to remove residual salt. Then the washed powder was placed into a stirred 6 M HCl solution for 7 h with O_2 bubbling for Cu leaching to obtain the Mo_6S_8 product. Finally, the remaining powders were washed with water and dried in the oven at 120 ^{o}C for 2 h.

Preparation of two electrolytes: The preparation of electrolytes was performed in an argon-filled glove box with H_2O and O_2 less than 2 ppm. APC electrolyte was prepared by dissolving the corresponding amount 2 M Phenylmagnesium chloride in tetrahydrofuran $(PhMgCl)_2$/THF and $AlCl_3$ in tetrahydrofuran (THF) to get 0.4 M $(PhMgCl)_2$-$AlCl_3$. All these chemicals were water free grade and purchased from Sigma-Aldrich. 1 M $Mg(ClO_4)_2$/AN was prepared by dissolving a corresponding amount of anhydrous $Mg(ClO_4)_2$ (Fox-Chemicals) in anhydrous acetonitrile (AN, Alfa Aesar) with vigorous stirring at room temperature in the Ar-filled glovebox.

Morphological, Structural and Surface Characterization: The morphology was studied with a Zeiss Supra 55 Scanning Electron Microscope (SEM) with primary energy of 15 keV. The structural characterizations were done using synchrotron radiation (λ = 0.4132 Å, 30 keV) at the Material Science and Powder Diffraction beamline (MSPD) at ALBA synchrotron (Barcelona, Spain)[266]. The powder diffraction patterns were collected in capillary geometry with powders filled in 0.5 mm Ø boro-silicate capillaries. Raman scattering on electrodes was recorded on a microscope type HORIBA LabRam Evolution HR with a laser source (λ = 523 nm, 10 mW) from 100 to 1100 cm^{-1}. The electrodes after discharging and charging were washed with AN and dried under vacuum in the glovebox. Before the measurements, the electrodes were sealed in a cell with a quartz window inside a glovebox. The window is suitable for *ex situ* Raman measurement. X-ray photoelectron spectroscopy (XPS) was performed using a K-$Alpha^+$ XPS spectrometer (ThermoFisher Scientific, East Grinstead, UK) with a micro-focused, monochromatized Al K_α X-ray source. The samples storage and transportation to the spectrometer for XPS characterization was done in an airtight transport vessel under Ar. Thermo Avantage software was used to perform data acquisition and processing as described elsewhere[283]. The spectra were fitted with one or more Voigt profiles. All spectra were referenced to the C 1s peak of graphite at 284.4 eV binding energy controlled by means of the well-known photoelectron peaks of metallic Cu, Ag, and Au, respectively. The binding energy uncertainty of intense peaks was around ±0.1 eV and the uncertainty of weak peaks was estimated to be ±0.2 eV. The analyzer transmission function, Scofield's sensitivity factors[284] and effective attenuation lengths (EALs) for photoelectrons were applied for quantification and EALs were calculated using the standard TPP-2M formalism[285].

Electrochemical Characterization: The electrode mixture was prepared by mixing active material (V_2O_5 nanowires or Mo_6S_8), with Super C65 C (TIMCAL) and polyvinylidene difluoride (PVDF) binder in a ratio of 70:20:10 with N-Methyl-2-pyrrolidone solvent. After drying, the cathode materials (active V_2O_5 of 3.71 mg with total average thickness of 126 µm and Mo_6S_8 of 11.10 mg with total average thickness of 142 µm) were pressed on a current collector of 12 mm stainless steel mesh with a thickness of 60 µm before assembling the 2-electrode Swagelok cells (modified cell design from our previous work[286], see **Figure 3.1**). As displayed in **Scheme 3.1**, before assembling the cell $V_2O_5 \mid Mg(ClO_4)_2/AN \mid Mg_xMo_6S_8$ (x ~2), a cell consisting of $Mo_6S_8 \mid APC \mid Mg$ was made and discharged to obtain the $Mg_xMo_6S_8$ negative electrode. Then, the cell was disassembled and the $Mg_xMo_6S_8$ electrode was washed using THF solvent and dried in the glovebox. In the rebuild $V_2O_5 \mid Mg(ClO_4)_2/AN \mid Mg_xMo_6S_8$ cells, the mass of $Mg_xMo_6S_8$ was intentionally in excess (10-15 % capacity excess of $Mg_xMo_6S_8$ based on 1 mol of Mg^{2+} per mol V_2O_5). *Note that specific capacities in this work were calculated with respect to the weight of the V_2O_5 active cathode material.* Galvanostatic cycling and cyclic voltammetry experiments were performed using Bio-Logic VMP multichannel electrochemical workstation (long cycling with a rate of C/20; for *ex situ* Raman and XPS with a rate of C/80).

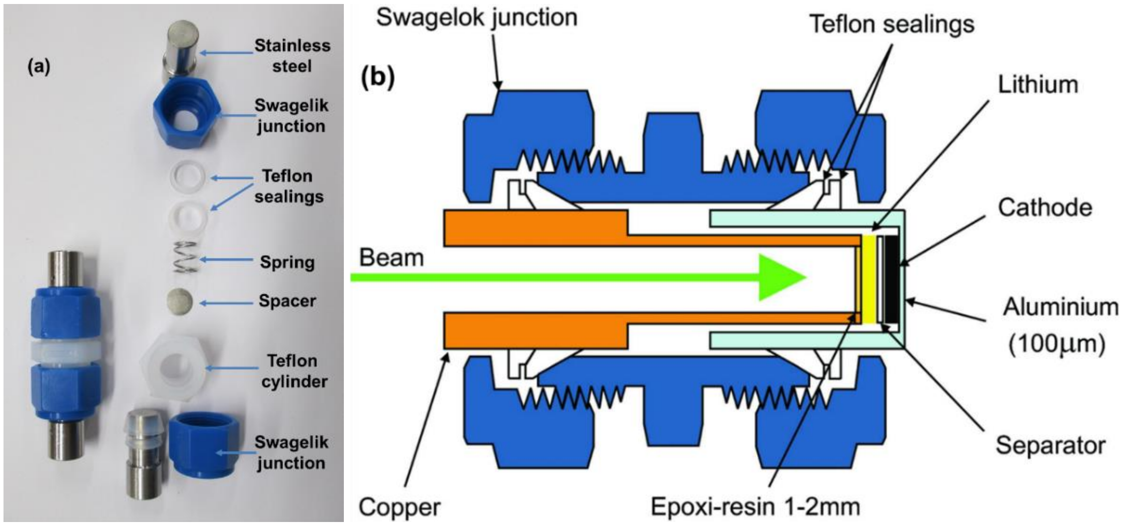

Figure 3.1 Photograph of the Swagelok cell and cell parts (a) and schematic drawing of the *in operando* Swagelok cell design from our previous work[286] (b)

Ex situ Raman and XPS samples preparation**:** the rebuild full cells, consisting of V_2O_5 and $Mg_xMo_6S_8$ with $Mg(ClO_4)_2$/AN electrolyte, were disassembled and the electrode under investigation was washed with AN in Ar-filled glovebox. Two samples were selected: one at 0.01 V after the first magnesiation (i.e after the first discharge) and the second one at 1.6 V after the first de-magnesiation (i.e. after the 1st charge) performed at C/80 rate. (For discharged/charged samples, the masses of V_2O_5 in the electrode were 3.185 mg/2.996 mg with total average thickness of ~110 µm and the masses of Mo_6S_8 were 9.24 mg/8.939 mg with total average thickness of ~135 µm).

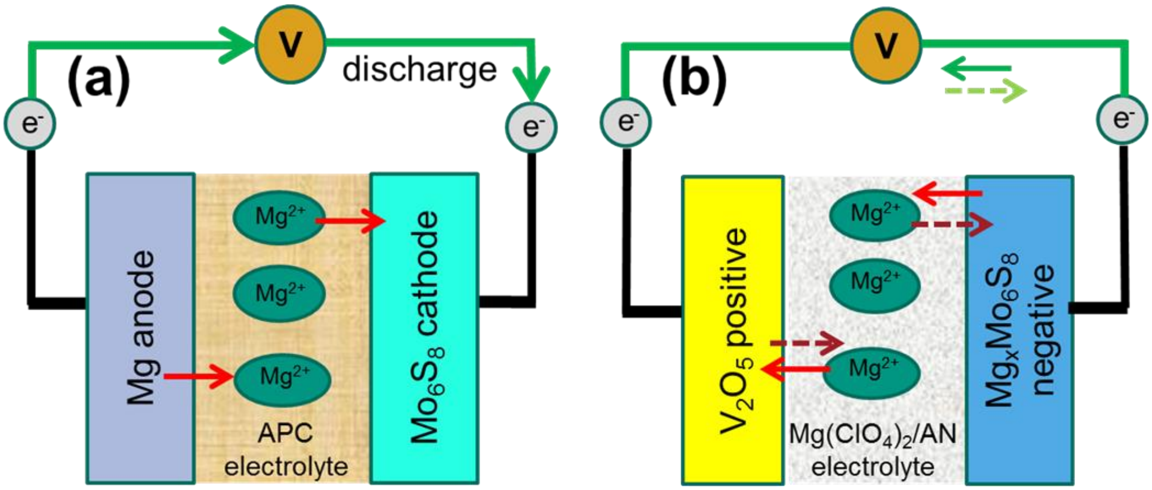

Scheme 3.1 The compositions of the half-cell for the electrochemical preparation of the $Mg_xMo_6S_8$ anode (a) and V_2O_5 │ $Mg(ClO_4)_2$/AN │ $Mg_xMo_6S_8$ (x ~2) cell configuration (b)

***In operando* synchrotron diffraction and *in operando* X-ray absorption spectroscopy (XAS):** *In operando* synchrotron diffraction during cycling was performed with synchrotron radiation at Material Science and Powder Diffraction beamline (MSPD) at ALBA synchrotron. The *in operando* cells for XRD were built by using 2025-type coin cells with 5 mm diameter beam entrance covered by glass windows. The cathode (V_2O_5 mixture total mass of 4.4 mg with an average thickness of 140 µm) was prepared by pressing the mixture on stainless steel mesh within a 5 mm hole in the center, and $Mg_xMo_6S_8$ anode (pure Mo_6S_8 mass: 9.94 mg with total average thickness of 155 µm) was made in the same way, but with a 5 mm hole in the center (**Figure 3.2a**). In this way, only the V_2O_5 material is detected during the *in operando* synchrotron measurements. More details of this setup can be found in Chapter 2[28]. *In operando* synchrotron diffraction patterns were collected at room temperature and λ= 0.4132 Å wavelength (30 keV), utilizing the position sensitive detector MYTHEN. Data were collected with effective exposure time of 60 s in steps of 0.006° over angular range of 1.8° - 42° in 2theta during the first two cycles with C/25 rate. In order to improve the powder averaging (increasing the number of crystallites contribution), the coin cells continuously oscillated +/-5 ° around the incoming beam direction.

The diffraction data analysis was carried out by the Rietveld method using the Fullprof software package[287]. For the Rietveld analysis of Mg-poor and Mg-rich phases of V_2O_5, the same structural model with different lattice parameters was used[40]. For the Rietveld refinement, the occupancy of Mg was determined and fixed according to the charge and capacity obtained from the electrochemical measurements, where x in $Mg_xV_2O_5$ is recorded by EC lab® software for each diffraction pattern. *In operando* XAS measurements were carried out at the synchrotron at the KIT, Karlsruhe. Photographs and schematic drawing of the *in operando* cell set up, modified from our previous work are shown in **Figure 3.2b** and **Figure 3.2c**[288]. *In operando* XAS measurements were carried out during the first discharge - charge with C/25 rate (active V_2O_5 of 3.493 mg with average thickness of 145 µm and pure Mo_6S_8 mass of 10.15 mg with average total thickness of 155 µm). XAS spectra of Vanadium were recorded in quick-XAS (6 min/spectrum) mode in fluorescence geometry using a germanium detector, since the penetration depth is several µm thick (bulk method), and the chances of a fluorescence photon to reach the detector are excellent. The V K-edge for V_2O_5 was measured during the electrochemical cycling and the energy was calibrated using a vanadium foil as it is commonly employed in XAS experiments. V_2O_3, VO_2, and V_2O_5 were used as standard materials. All the data were collected at room temperature with a Si (111) double crystal monochromator and all the XAS spectra were processed using the DEMETER software package[289].

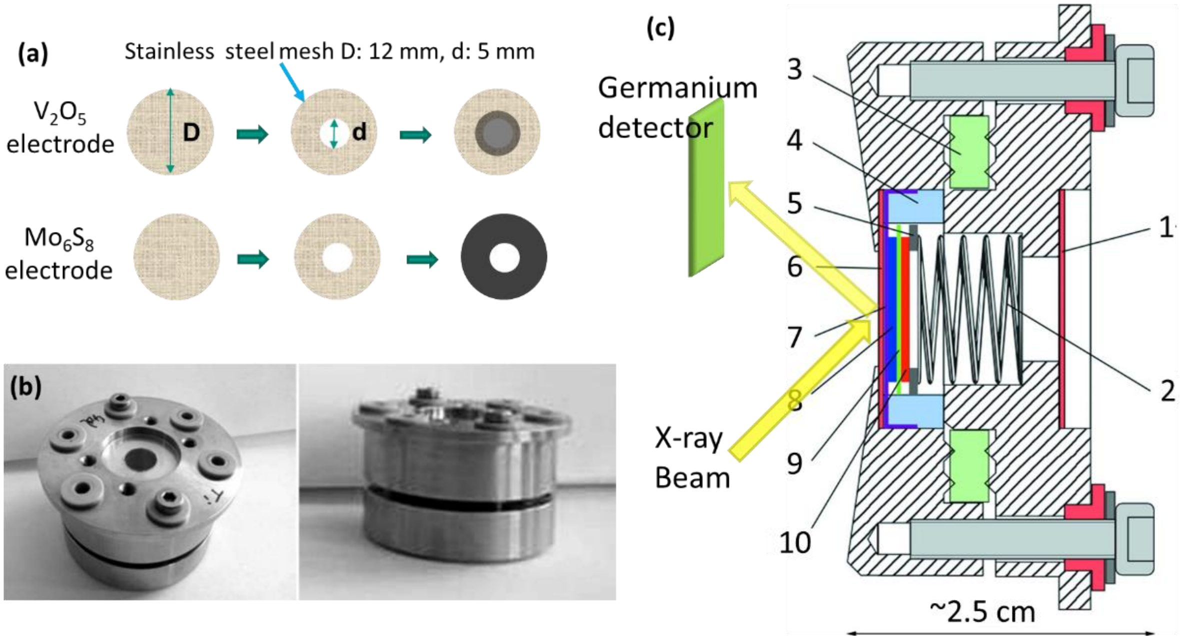

Figure 3.2 Electrode preparation used for *in operando* cell (a), photographs and schematic diagram of the *in operando* cell design (b, c): (1) and (6) 125 µm Kapton windows, (2) contact spring (Stainless steel), (3) Plastic sealing ring, (4) insulating PTFE ring, (5) and (7) current collector and current collector of stainless steel mesh with 9 mm hole in the center, (8) working electrode (WE), (9) Whatmann separator, and (10) counter electrode (CE) (Modified cell design from our previous work[288]).

3.3 Results and discussion

3.3.1 Structural and morphological characterization

The synchrotron diffraction pattern of pristine V_2O_5 nanowires powder is displayed in **Figure 3.3**, indicating a high crystallinity of the material. All reflections can be indexed as the orthorhombic α-V_2O_5 structure model with space group *Pmn*2_1. The lattice parameters are a=11.511 Å, b=4.373 Å, and c=3.565 Å, in good agreement with a previous report[40]. It is quite different from the bilayered $V_2O_5 \cdot nH_2O$[290] that only has few reflections due to its low crystallinity, suggesting the water-free crystalline V_2O_5 in the present work. Scanning electron microscopy (SEM) (see the inset in **Figure 3.3**) shows that the V_2O_5 consists of nanowires. The prepared Mo_6S_8

has hexagonal structure with space group *R* -3 (see **Figure 3.4**) and lattice parameters *a*=*b*=9.195 Å, *c*=10.884 Å (Bragg R-factor=3.74, Rf-factor=1.81). Two small reflections at 13.34° and 16.99° imply a very small amount of impurity as pointed out by pink arrows in **Figure 3.4**.

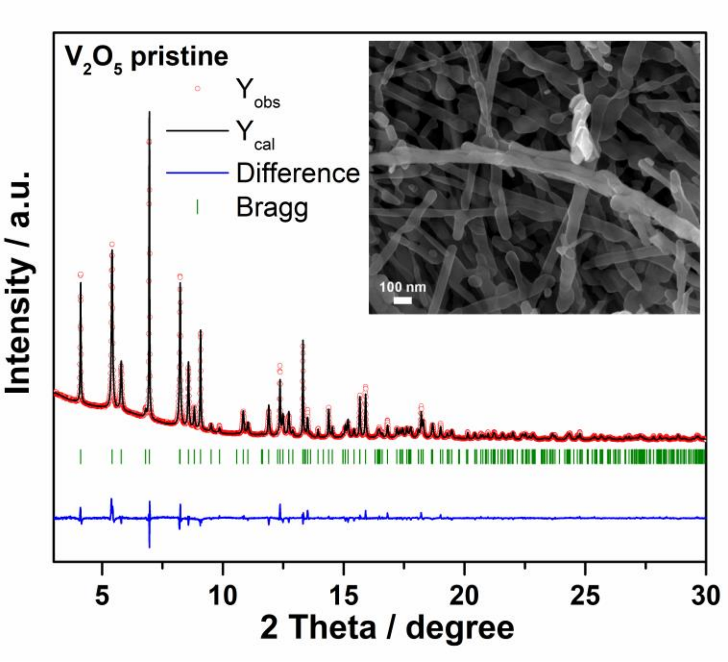

Figure 3.3 Rietveld refinement from synchrotron diffraction data of V_2O_5 nanowires (inset: SEM image)

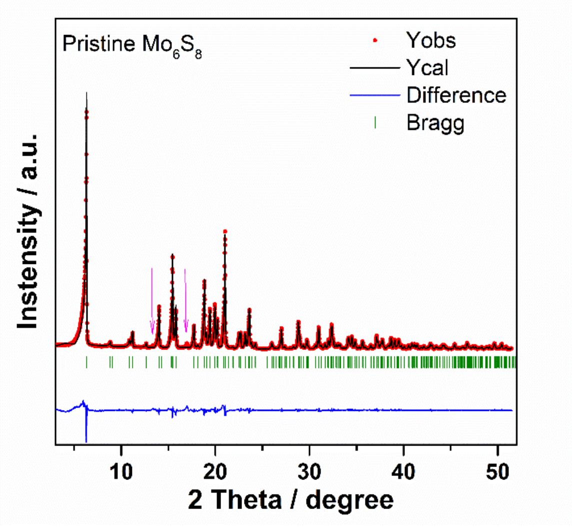

Figure 3.4 Rietveld refinement from diffraction data of Mo_6S_8 (Mo radiation, λ= 0.70932 Å)

3.3.2 Electrochemical properties

Figure 3.5 shows the voltage-capacity curve related to the magnesiation of the Mo_6S_8 electrode in APC electrolyte at C/50. During the 1st discharge, Mo_6S_8 exhibits one plateau at around

0.9 V with an initial discharge capacity of 125 mAh g^{-1} (theoretical capacity of 128 mAh g^{-1}), which is in good agreement with previous works[162, 272].

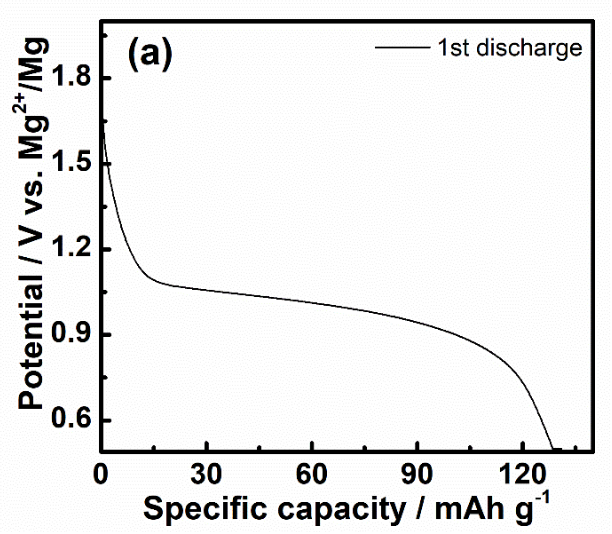

Figure 3.5 The voltage-capacity curve for magnesiation of Mo_6S_8 electrode in APC electrolyte at C/50 rate

Figure 3.6 displays the cycling behavior of V_2O_5 electrode in a cell configuration with $Mg(ClO_4)_2$/AN electrolyte at C/20. During the 1st discharge, a short plateau at around 0.9 V and a long plateau at around 0.4 V are observed. In contrast, only one flat plateau appears at about 1.1 V for the 1st charge process. V_2O_5 delivers an initial magnesiation/de-magnesiation capacity of 103 mAh g^{-1} (0.35 Mg^{2+})/110 mAh g^{-1} and the highest discharge capacity of 130 mAh g^{-1} in the 6th cycle. The cell exhibits a discharge capacity of 102 mAh g^{-1} in the second cycle with a lower plateau compared with that of the 1st discharge. The capacity or the amount of Mg-ion insertion not only depends on the plateau but also depends on the working voltage range. The cell shows a capacity increase in the following few cycles performed at C/20. After 100 cycles, the cell still delivers a capacity of 36 mAh g^{-1} as shown in **Figure 3.6b**. The possible reason of capacity decay could be ascribed to the unwanted side reaction[291], for example, the dissolution of V_2O_5 active material from the electrode [274, 292] or irreversible structural changes for V_2O_5. The "capacity match" between cathode and anode materials might also play an important role in an "unideal state"[291]. However, understanding the cause of capacity fading along cycling is rather complicated for current operating cell configurations and requires further investigations. The origin of the capacity fading along cycling was not studied in this work. Since $Mg_xMo_6S_8$ was taken in 10-15 % excess capacity (based on 1 Mg-ion insertion per V_2O_5) and this anode material has good rate capability, it can provide enough Mg-ions for the intercalation into the V_2O_5 host structure[160, 162]. The voltage profiles of the cell are determined by the curves of V_2O_5 and $Mg_xMo_6S_8$ in half-cells. As the state of charge x in the $Mg_xMo_6S_8$ anode is different for the investigated cell configurations, different voltage profiles are observed in spite of the same initial V_2O_5 electrodes. This difference could result from the different practical "capacity match" between cathode and anode materials as well as the different polarizations resulting from different C rates applied. However, the electrochemical mechanism of V_2O_5 is expected to be the same, despite the observation of different voltage profiles in the cell configuration when similar amount of Mg-ions are intercalated into the same V_2O_5. Note that the plateaus cannot be easily distinguished and assigned in the cell configuration system since both V_2O_5 and $Mg_xMo_6S_8$ electrodes have their specific electrochemistry characteristics. In the specific case, the sluggish Mg-ion solid diffusion cannot be completely avoided in spite of nanostructured V_2O_5, but the electrochemical performance can be promoted owing to the high reaction areas and short Mg-ion migration pathways of V_2O_5 nanowires. A serious capacity degradation of the cell is supposed at higher C rates because of the sluggish Mg-ion solid diffusion. Although it is not realistic using such slow charge/discharge rate of C/20 for the practical application, this work demonstrates that this cell configuration works and, consequently, **can be used for investigating V_2O_5 through *in operando* techniques**.

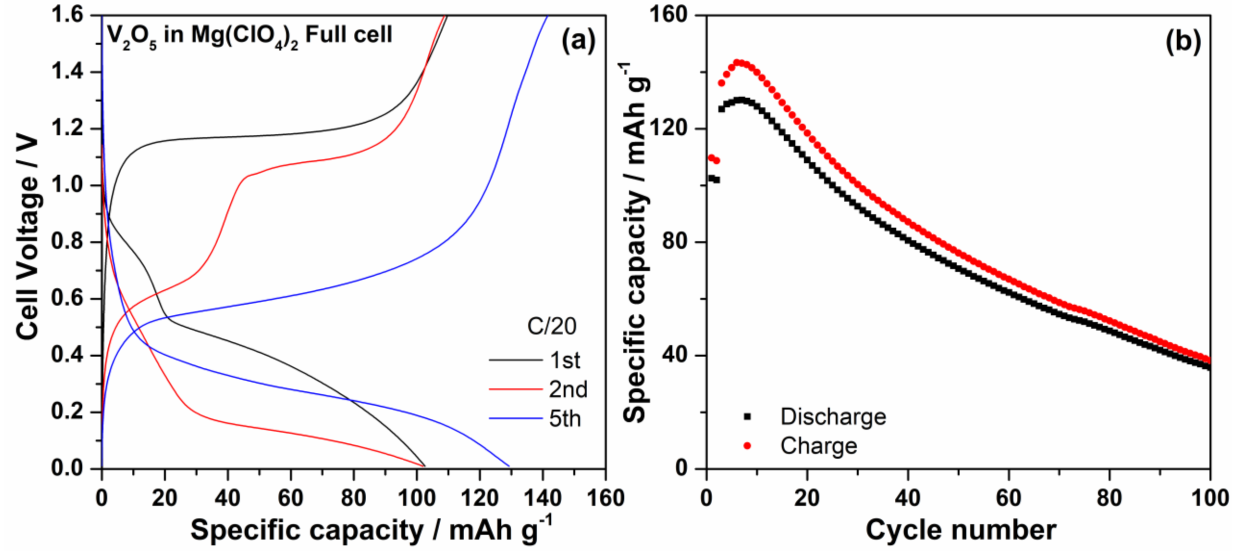

Figure 3.6 Discharge-charge profiles (a) and cycling performance (b) of V_2O_5 | $Mg(ClO_4)_2$/AN | $Mg_xMo_6S_8$ (x ~2) full cell (C/20) in the voltage range of 1.6 - 0.01 V.

3.3.3 Electrochemical mechanism

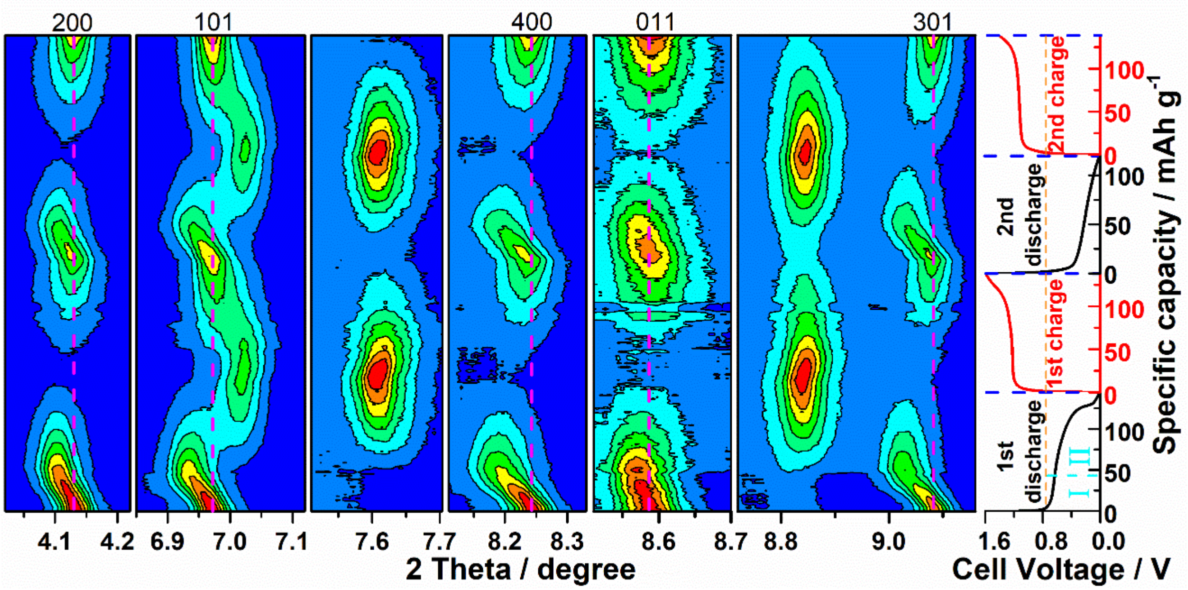

Figure 3.7 Contour maps of *in operando* synchrotron diffraction of V_2O_5 collected during the first two cycles and the corresponding discharge-charge profiles at a current rate of C/25 in cell voltage range between 0.01 - 1.6 V

In order to clarify the electrochemical mechanism during the Mg insertion and extraction in V_2O_5, *in operando* synchrotron diffraction was conducted. Contour maps in the selected ranges during the first two cycles are displayed in **Figure 3.7**. At the initial stage of discharge, all the reflections could be indexed based on an orthorhombic α-V_2O_5 phase with space group *Pmn*2$_1$ (see the Rietveld refinement of pristine V_2O_5 in **Figure 3.8a**). In the beginning of the 1st discharge (Mg insertion), most reflections of V_2O_5 gradually shift to lower angles, indicating a solid solution process with an expansion of the unit cell (**Region I**). The Mg content of the Mg-poor phase at the end of the solid solution regime was estimated as $Mg_{0.14}V_2O_5$ with lattice parameters of *a*=11.616 Å, *b*=4.369 Å, and *c*=3.591 Å, according to the diffraction patterns and the corresponding electrochemical profile (see the Rietveld refinement of $Mg_{0.14}V_2O_5$ in **Figure 3.8b**, pattern 21st). Some new reflections appear at 3.8°, 5.7°, 7.0°, 7.6°, 8.84°, 11.4°, 11.65°, 13.5°, 14.94°, and 15.99° when the composition is $Mg_{0.143}V_2O_5$, with a capacity of 42 mAh g^{-1}. The intensities of these new reflections increase, while those from the $Mg_{0.14}V_2O_5$ phase decrease and do not disappear completely at the end of discharge (See **Figure 3.9**). Therefore, in the composition range of $Mg_{0.143}V_2O_5$ to $Mg_{0.49}V_2O_5$ (Mg in total 0.49 at 0.01V), a two-phase transition between $Mg_{0.14}V_2O_5$ and a new phase with higher Mg-content occurs (**Region II**). The appearing phase also has an orthorhombic structure with a space group *Pmn*2$_1$ as the pristine V_2O_5, but with different lattice parameters. For the Mg-rich phase ($Mg_xV_2O_5$), x was estimated as 0.6 with lattice parameters of *a*=12.503 Å, *b*=4.181 Å, and *c*=3.523 Å, according to the Rietveld refinement and the corresponding electrochemical profile (see the Rietveld refinement based on pattern 70th in **Figure 3.8c**). In the very beginning of the 1st charge process, the intensities of the reflections from the Mg-rich $Mg_xV_2O_5$ phase slightly increase, which might be a delay of the structural response, because of the slow Mg^{2+} diffusion inside the electrode materials. Then, the intensities of the Mg-rich $Mg_xV_2O_5$ phase gradually decrease, while those intensities of the phase with lower Mg content grow up. The positions of the reflections remain at slightly lower 2theta values than that for the initial state. This small unit cell expansion indicates either some residual Mg in the host structure or an irreversible transformation, for example, due to a minor oxygen loss. However, the reflections from the Mg-rich $Mg_xV_2O_5$ phase still exist at the end of the 1st charge (see **Figure 3.8d**), which might be correlated to the small irreversible capacity. For the second discharge, the evolution of the reflections is very resembling to what observed for the first discharge. However, the reflections return back to the initial positions of pristine V_2O_5 and a single phase is obtained at the end of the 2nd charged state at 1.4 V (not reach 1.6 V due to the limited beamtime), indicating the high reversibility of the V_2O_5 material during Mg insertion/extraction (see **Figure 3.8e**). Note that the ratio of V and O is constantly 2:5 in the chemical formula, $Mg_xV_2O_5$, despite the existence of minor V^{3+}, residual from the surfactant P123 (confirmed by XPS), and the possible dissolution of V ions into the solvent or decomposition of V_2O_5.

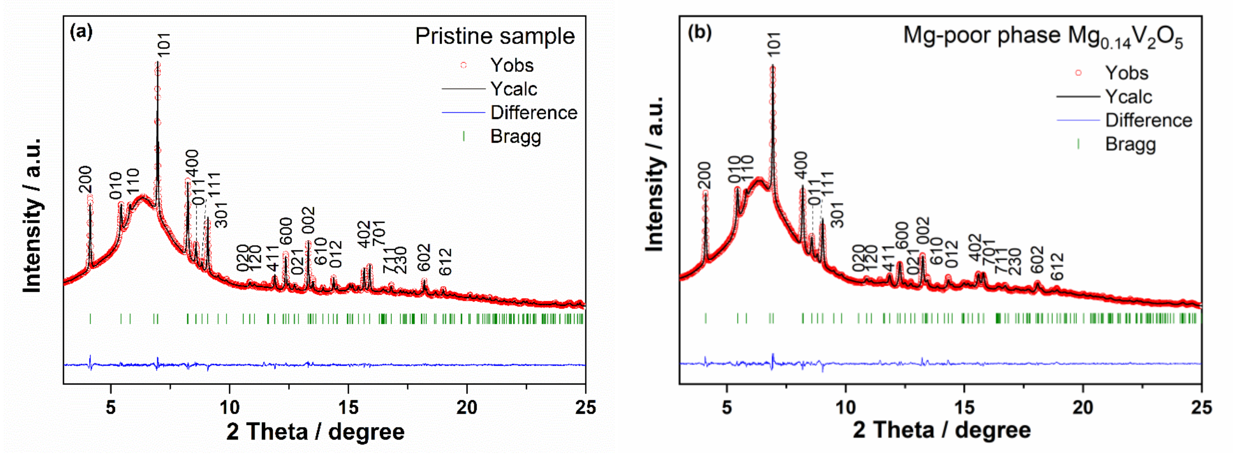

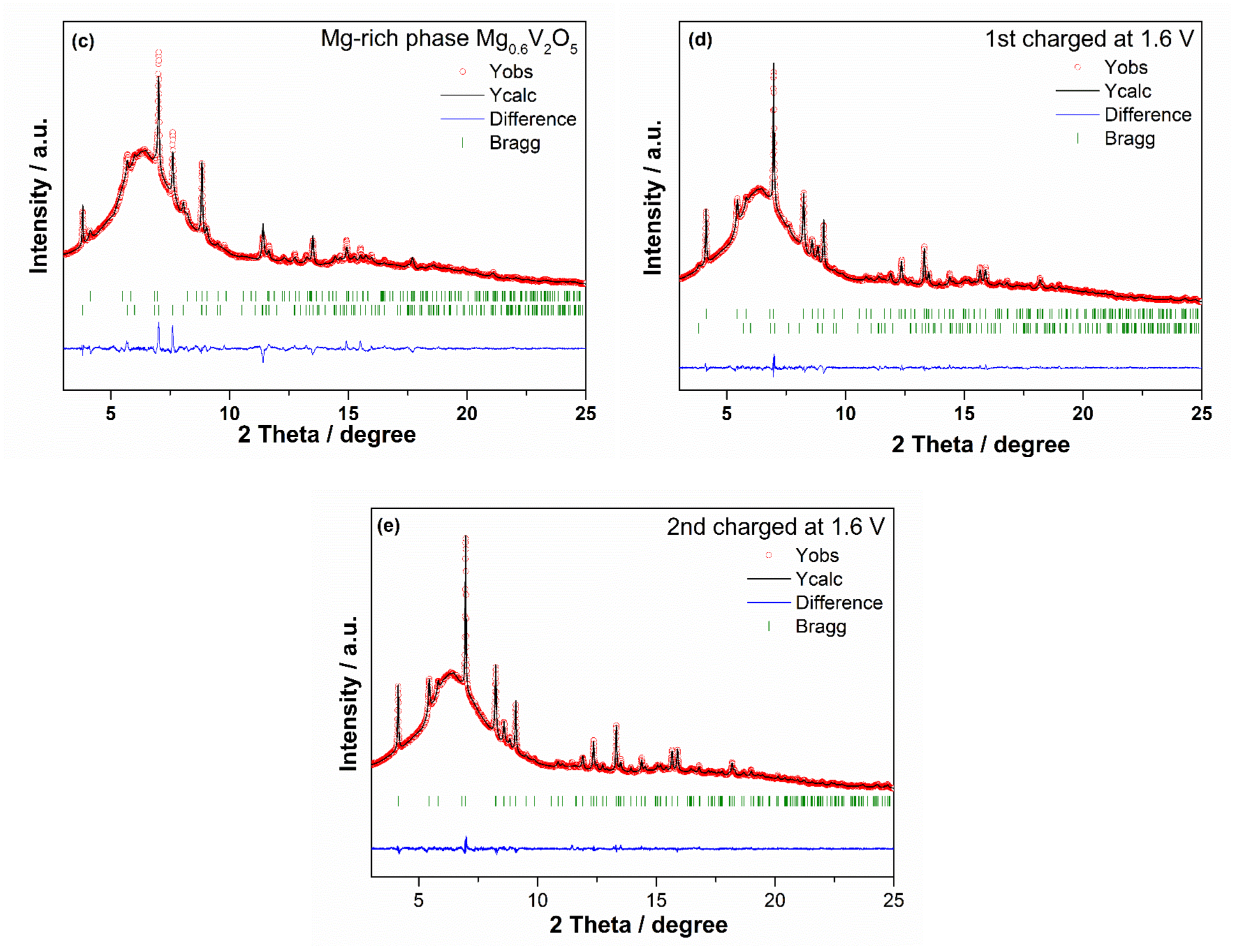

Figure 3.8 Rietveld refinement of the pristine V_2O_5 (a), Mg-poor phase $Mg_{0.14}V_2O_5$ in the solid solution region (pattern 21st, corresponding to the last pattern in solid solution region) (b), the V_2O_5 electrode at 1st discharged state of 0.01 V (c), the V_2O_5 electrode at 1st charged state of 1.6 V (d), and the V_2O_5 electrode at 2nd charged state of 1.6 V (e)

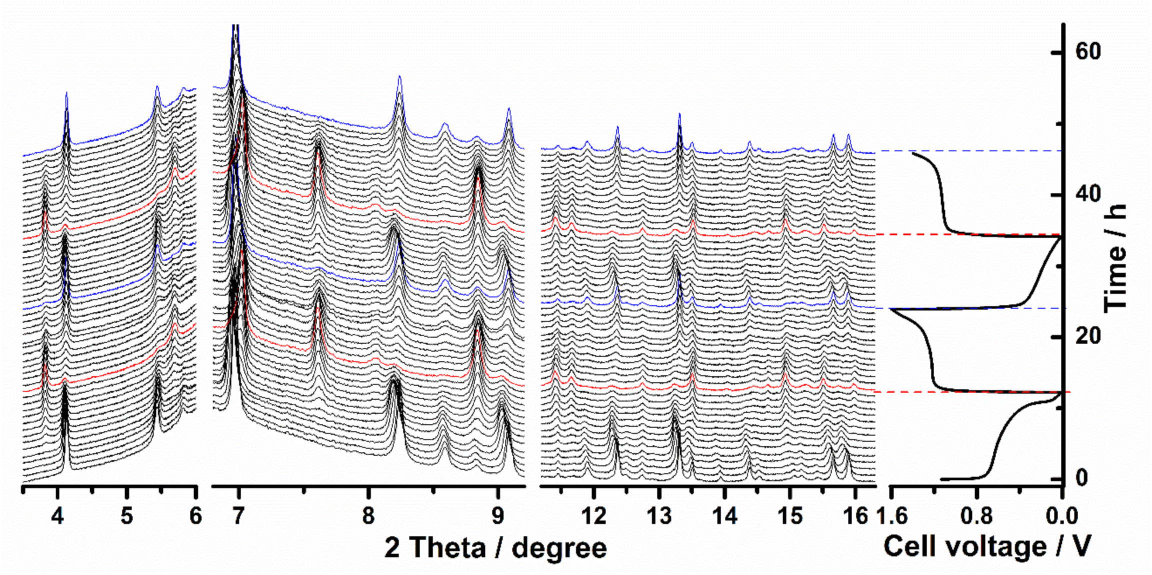

Figure 3.9 *In operando* synchrotron diffraction patterns

The structural parameters and phases ratios are shown in **Figure 3.10**. During the beginning of the discharge, the phase V_2O_5 accommodates Mg-ions via a solid solution mechanism up to a limiting stoichiometry of $Mg_{0.14}V_2O_5$ accompanied with an increase of *a* and *c* and a decrease of *b* lattice parameters. After that, magnesium uptake goes through a two-phase region with the decrease of the $Mg_{0.14}V_2O_5$ amount and an increase of Mg-rich $Mg_{0.6}V_2O_5$ phase with constant cell parameters for both phases. The phase ratio of $Mg_{0.14}V_2O_5$:$Mg_{0.6}V_2O_5$ is 13:87 at the end of 1st discharge. During the 1st charge process, the material exhibits first a two-phase transition and then a solid solution together with a two-phase transition (the decrease of *a* and *c*, the increase of *b*). In the second cycle, the material shows the same behavior as observed in the first discharge-charge process, except for the slightly different phase contribution of both phases at the end of 2nd discharge ($Mg_{0.14}V_2O_5$:$Mg_{0.6}V_2O_5$ = 15:85) and a very short region close to the end of the 2nd charge. The V_2O_5 material returns back to its original structure at the end of the 2nd charge.

The $Mg_xV_2O_5$ phase appearing during the electrochemical insertion of magnesium into V_2O_5 differs from MgV_2O_5 and $Mg_{0.2}V_2O_5$ reported in the literature[293-294]. MgV_2O_5 crystallizes in orthorhombic structure with a space group of *Cmcm* and $Mg_{0.2}V_2O_5$ has the same structure as the parent V_2O_5 with similar lattice parameters[293-294]. In addition, first-principles calculations, in which a δ-phase (space group: *Cmcm*) presuppose a better mobility for Mg diffusion[295], are not supported by our experimental results either. Meanwhile, first-principles calculations also illustrate that an ε-phase[295], with a specific ordering of Mg-ions at half magnesiated α-V_2O_5 host, is the most stable configuration in the α host and is somehow in agreement with our result, like Li-ordering is observed in Li-V_2O_5 system[68, 295] and has Li-ions at alternate sites along with the a-axis[296]. Recently, Xiao et al.[297] reported that V_2O_5 undergoes a phase-transition from α-phase to ε-phase and δ-phase in turn upon Mg insertion (0→0.5→1), using first-principles calculations. In the Li-V_2O_5 system, it is well known that a topotactic reaction is observed during lithium insertion into V_2O_5 ($0 < x < 1$)[298], where ‘‘topotactic‘‘ is used to describe that the basic structure of the positive electrode material is maintained during the reaction. The structure of ε-$Li_{0.46}V_2O_5$ (*a*=11.417 Å, *b*= 3.565 Å, and *c*=4.508 Å) has been identified and is very close to that of α-V_2O_5[296]. The newly observed $Mg_{0.6}V_2O_5$ phase (*a*=12.503 Å, *b*=4.181 Å, and *c*=3.523 Å) can also be called ε-$Mg_{0.6}V_2O_5$ phase since the basic structure of the pristine V_2O_5 material is maintained, although the differences in the lattice parameters are more pronounced. However, an increase of the interplanar distance and a decrease of lattice parameter *a* were observed during the lithiation of α-V_2O_5[296], which is different from a decrease of the interplanar distance and an increase of lattice parameter *a*, as obtained during magnesiation of α-V_2O_5 (**Region I** in **Figure 3.7**). This is attributed to the larger charge and smaller radii of Mg^{2+} in the host structure V_2O_5, compressing the layer and extending the *a* direction.

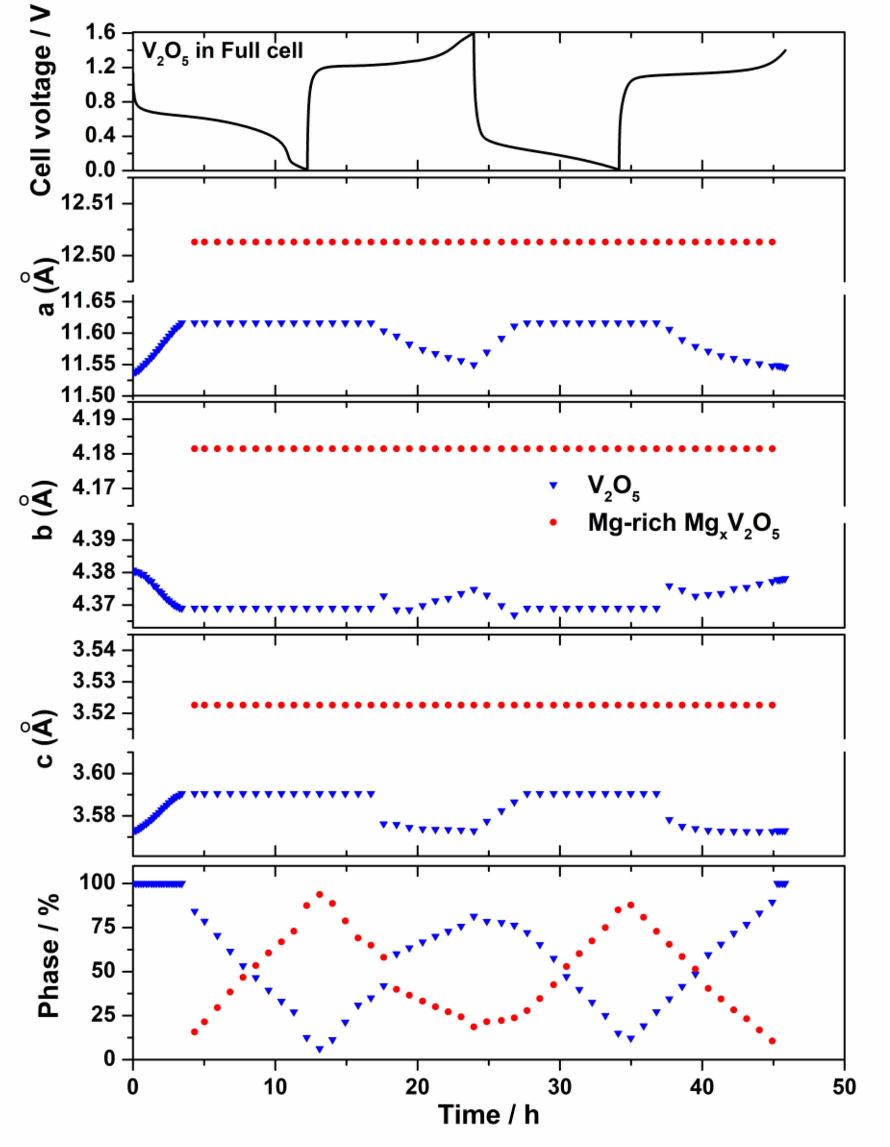

Figure 3.10 The structural parameters and phases ratios from selected diffraction patterns with Rietveld refinement during the first two cycles for V_2O_5

In order to probe the electronic and structural environments of V-ions during the electrochemical process, *in operando* X-ray absorption spectroscopy was performed on the V_2O_5 cathode material in an *in operando* coin cell. For the V K-edge, XAS spectra of V_2O_5, VO_2, and

V_2O_3, where the V-ions exist in +5, +4, and +3 oxidation states, respectively, are used as standard materials. The edge position of V K-edge spectra, collected at different voltages, is compared with reference spectra. The amount of magnesium inserted into the cathode was determined from the charge passed through the cell recorded by EC lab® software for each spectrum. As demonstrated in **Figure 3.11**, in terms of V K-edge, the edge position of the XAS spectrum, corresponding to the initial state, is slightly lower than that of the reference V_2O_5 spectrum. Therefore, it can be confirmed that the oxidation state of V is mainly +5 in the initial state, which is in agreement with the XPS result for pristine V_2O_5 (**Figure 3.15)**. In addition, an intense pre-edge peak on XANES data for the V K-edge of pristine V_2O_5 is observed, which is attributed to the transitions between the 1s and bound p-hybridized d-states[299-300] when the centro-symmetric character of V site is lost. This is because the crystal structure of V_2O_5 is orthorhombic, consisting of layers of $[VO_5]$ square pyramids sharing edges and corners, and the V-ions are five-fold coordinated by oxygens in a distorted tetragonal pyramid as shown in **Figure 1.2**.

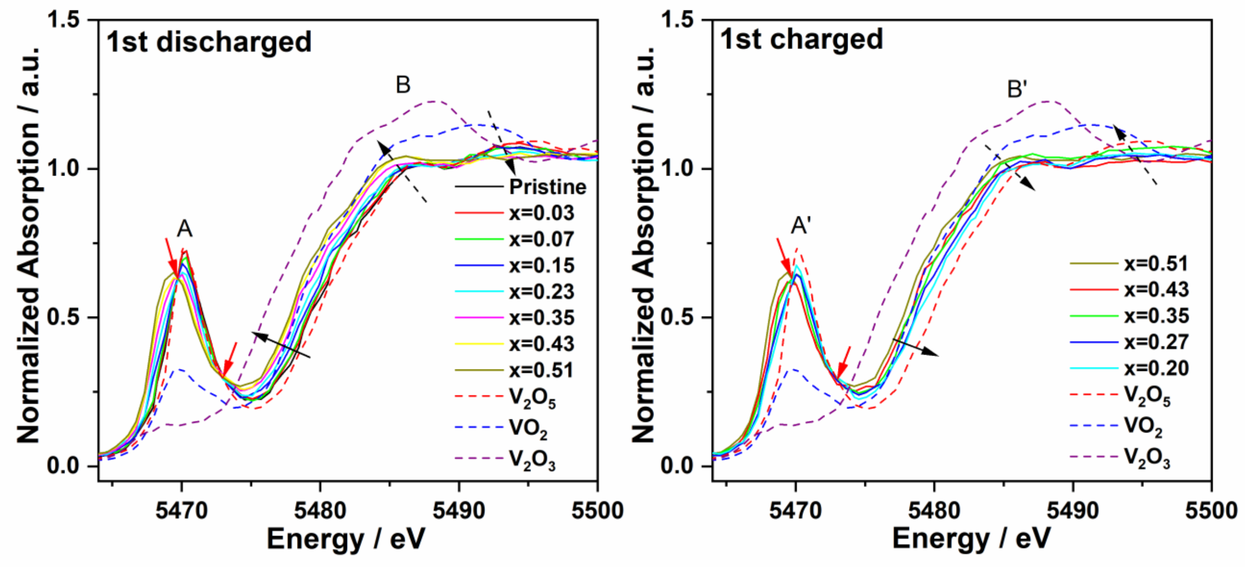

Figure 3.11 *In operando* X-ray absorption near edge structure (XANES) for V K-edge during the first discharge-charge process; the isosbestic points are indicated by red arrows.

During the discharging process, the edge position of the V K-edge continuously shifts to lower energy, indicating a reduction of vanadium ions, which is correlated to the increase of inserted Mg ions into V_2O_5. This is consistent with the electrochemical data (see **Figure 3.12**) and XPS result in **Figure 3.15**. The edge position of the V K-edge for the electrode discharged to 0.01V (0.51 magnesium per mol V_2O_5 inserted) is almost in the middle between that of standard V_2O_3, and

V_2O_5, where a similar result was observed for bilayered V_2O_5 after Mg-ion insertion[278]. The pre-edge peak (A in **Figure 3.11**) also gradually shifts to lower energy and becomes broad, while the pre-edge peak intensity progressively reduces, suggesting the vanadium ions reduction and the deformation of the local V environments during Mg^{2+} insertion. The broadness of the pre-edge peak is attributed to co-existence of distorted tetragonal pyramid and centrosymmetric VO_6 octahedral. The edge resonance (B and B' in **Figure 3.11**) displays significant changes in both intensity and shape, which is related to the energy absorption by core electrons[300-301]. During the discharge process, the shape changes from two broad peaks to a single broad peak (peak B in **Figure 3.11**) and the intensity of one peak at around 5486 eV slightly increases while the other one at around 5493 eV slightly decreases. Moreover, two distinct isosbestic points[302] (red arrows in **Figure 3.11**) are detected at both high and low energy for discharge and charge processes, indicating the two-phase along with the Mg ions insertion into and extraction from V_2O_5. For the charging process, the edge position of V K-edge shows a reversible behavior with a shift to higher energy, indicating the oxidation of V in the material. The pre-edge peak and edge resonance (A' and B' in **Figure 3.11**) also display reversible behavior compared with that of the discharging process. However, unfortunately, the recording of the charging process is not complete due to a beam loss during the experiment at the beamline.

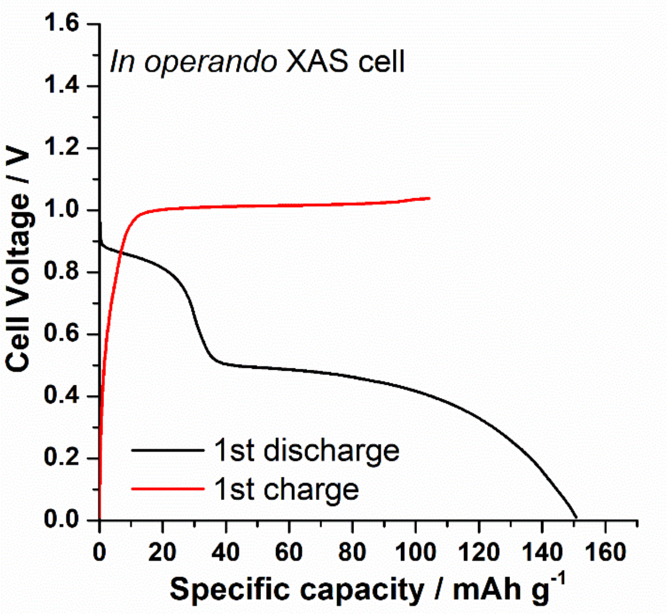

Figure 3.12 Discharge-charge profiles of V_2O_5 | $Mg(ClO_4)_2$/AN | $Mg_xMo_6S_8$ (x ~2) full cell for *in operando* XAS (C/25)

To study the local structure of the samples, Raman scattering was carried out as shown in **Figure 3.13**. As known in the pristine orthorhombic V_2O_5, oxygen atoms occupy four types of sites in a $[VO_5]$ slab, denoted as O(1)–O(4). The stretching mode of the V–O(1) bond is located at 993 cm^{-1} while its bending vibrations are located at 404 and 283 cm^{-1}. Raman peaks at 484 cm^{-1} and 700 cm^{-1} are attributed to the bending vibration of the V–O(2) and the stretching vibration of the V–O(3), respectively. The peaks at 528 and 304 cm^{-1} are assigned to the stretching and bending vibrations, respectively, of the V–O(4) bond. The peaks at lower wavenumbers, 143 and 197 cm^{-1} are due to a weak van der Waals interaction between adjacent $[VO_5]$ slabs. These results are in good agreement with previous work[171, 303]. After Mg^{2+} is inserted, significant changes can be obtained and some peaks from V_2O_5 become weak such as 993 and 143 cm^{-1}, while those at 700, 528, 304, and 283 cm^{-1} completely disappear. Meanwhile, some broad new peaks appear at 159, 246, 360, 460, 509, 751, 896, and 945 cm^{-1}. Similarly, significant changes via *in operando* Raman study are also obtained for V_2O_5 during Li-insertion in the range of $0<x<1.0$ ($Li_xV_2O_5$)[303]. Therefore, these new peaks might be attributed to the new phase of ε-$Mg_{0.6}V_2O_5$, where the broad peaks are probably ascribed to the disordered local structure in the ε-$Mg_{0.6}V_2O_5$ phase. A broad peak centered at 900 cm^{-1} is also obtained for $Mg_{0.5}V_2O_5$ in Gershinsky's work[171]. It can be deduced that Mg ions are inserted into the interlayer of V_2O_5 crystals and bonded with oxygen atoms ($[MgO_6]$ octahedra) in the V_2O_5 structure to form the Mg-rich $Mg_xV_2O_5$ phase. After charging, new peaks observed in the discharged state disappear and those peaks from V_2O_5 return back to the initial state.

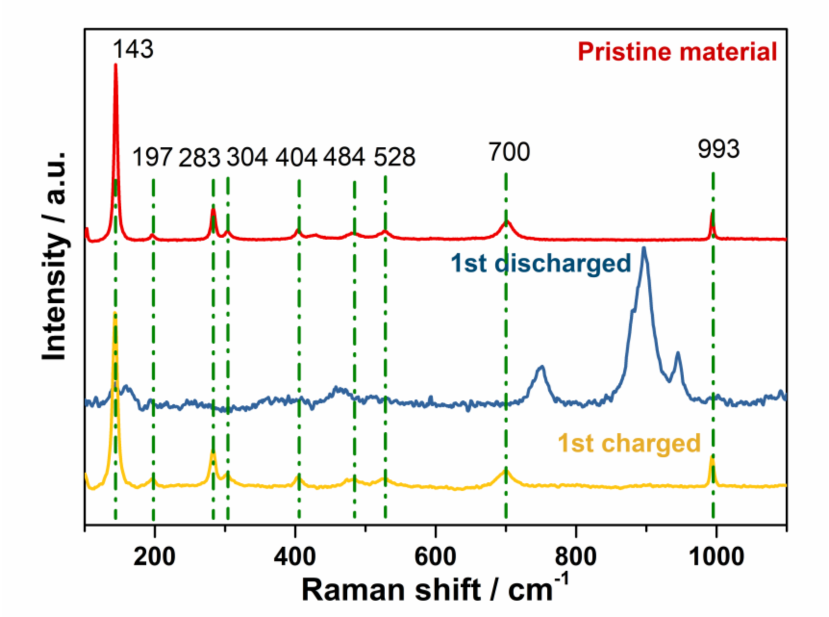

Figure 3.13 Raman spectrum of pristine V_2O_5, 1st discharged V_2O_5, and 1st charged V_2O_5

X-ray photoelectron spectroscopy (XPS) was used to look into the surface chemistry and surface elemental composition of pristine V_2O_5, 1st discharged V_2O_5, and 1st charged V_2O_5 (XPS survey spectra of three materials see **Figure 3.14**).

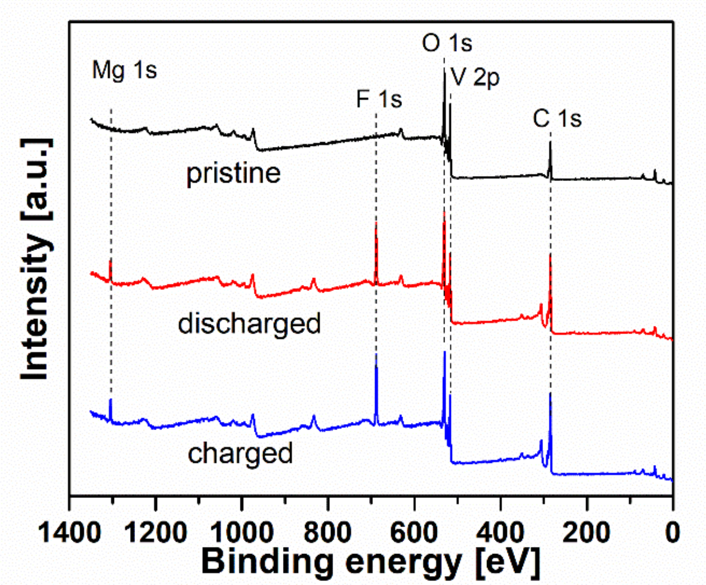

Figure 3.14 XPS survey spectra of pristine V_2O_5, 1st discharged V_2O_5, and 1st charged V_2O_5

According to **Figure 3.15**, the V 2p spectrum of pristine V_2O_5 can be fitted with two doublets: a main one with V $2p_{3/2}$ at 517.2 eV and a second one with weak intensity at 515.7 eV[304], which indicates that V exists mainly in the oxidation state +5 with a minor contribution of vanadium in

+3. It can be seen that the O 1s spectrum of pristine V_2O_5 can be fitted with 3 peaks at 533.6 eV, 532.0 eV, and 530.1 eV, which are corresponding to the O-C, O=C, and V-O groups[305-307]. O-C, O=C could be attributed to the residual surfactant symmetric triblock copolymer P123 during synthesis while the minor V(III) could be assigned to the reduction of residual surfactant P123 during the annealing at 400 °C. The V 2p spectrum in the discharged state could be fitted with 3.6 at% V(IV) at 516.7 eV, 2.6 at% V(V) at 517.3 eV, and 0.7 at% V(III) at 515.7 eV , while the V 2p spectrum in the charged state displays two V $2p_{3/2}$ components at 517.3 eV and 515.7 eV, returning back to the spectrum of pristine V_2O_5, with 5.9 at% V(V) and 0.6 at% V(III). Therefore, ~60 % of V was reduced to V(IV) during the electrochemical discharge and then again fully oxidized upon electrochemical charging, which is consistent with the electrochemical data (x=0.62 in $Mg_xV_2O_5$).

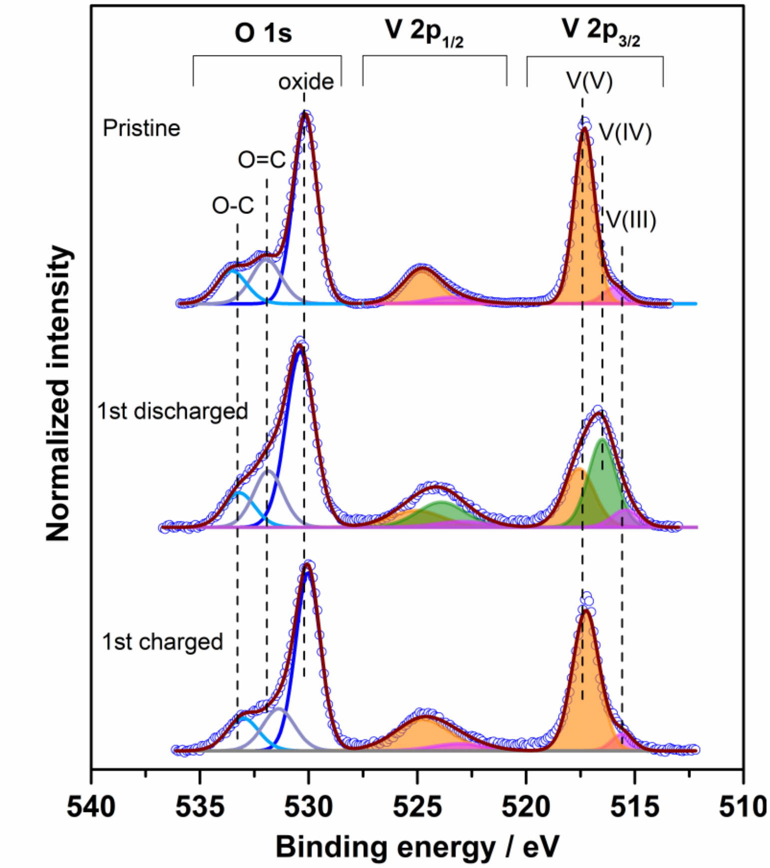

Figure 3.15 V 2p and O1s X-ray photoelectron spectra of pristine V_2O_5, 1st discharged V_2O_5, and 1st charged V_2O_5

3.4 Conclusion

In conclusion, orthorhombic V_2O_5 nanowires were successfully synthesized via a hydrothermal method. In the $V_2O_5 | Mg(ClO_4)_2/AN | Mg_xMo_6S_8$ full cell, the V_2O_5 nanowires deliver an initial discharge/charge capacity of 103 mAh g^{-1}/110 mAh g^{-1} and the highest discharge capacity of 130 mAh g^{-1} in the 6th cycle at a C/20 rate. The reversibility of the magnesium insertion/extraction in the V_2O_5 is clarified through *in operando* synchrotron diffraction and *in operando* XAS together with *ex situ* Raman and XPS. *In operando* synchrotron diffraction and *ex situ* Raman revealed the formation of a new phase of Mg-rich $Mg_xV_2O_5$ during Mg insertion and the recovery of V_2O_5 during Mg extraction. *In operando* XAS and *ex situ* XPS confirmed the reduction/oxidation of vanadium during the Mg insertion/extraction. It is the first time that the structural evolution and charge compensation mechanisms of Mg insertion into V_2O_5 in an electrochemical full cell are elucidated through *in operando* synchrotron diffraction and *in operando* XAS. This will pave the way to study the mechanism of electrode materials not only in the Mg-based batteries, but also in other various different challenging systems.

Detailed information can be found: *J. Am. Chem. Soc.* 2019, 141, 2305−2315

https://pubs.acs.org/doi/10.1021/jacs.8b08998

Chapter 4 *In operando* study of orthorhombic V_2O_5 as cathode material for rechargeable K-ion batteries

4.1 Introduction

Since the first rechargeable potassium battery was designed by Eftekhari[308-309] in 2004, employing Prussian blue (PB) as cathode, KIBs are becoming another promising candidate to replace LIBs for the large-scale EESs. KIBs are similar to LIBs in terms of working principle ("rocking chair"), but the advantages of KIBs are potassium abundance and low cost. Despite the fact that K-ion is larger and heavier than Li^+, Na^+, and Mg^{2+}, the K^+/K couple has a lower standard electrode potential (-2.936 V vs. SHE) than that of Na^+/Na (-2.714 V vs. SHE) and Mg^{2+}/Mg (-2.37 V vs. SHE)[38, 309-311]. At the same, the usage of heavier alkali element (Na, Mg, and K) does not significantly influence the total weight of batteries. Concerning the capacity, it is unfair to compare the atomic weight of metal for gravimetric capacity, instead one should compare the formula weight of cathode electrode materials as stated by Komaba et al.[312-313]. For example, the mass ratio of (P2-type $K_{2/3}CoO_2$):(O3-$LiCoO_2$) is 1.19, giving a 19% increase of mass from cathode material for the whole KIB despite the presence of heavier K atom (M_K:M_{Li}=39/6.9=5.7). In addition, K-ion displays a lower ion-solvent interaction comparing to Li- and Na-ions. The lower desolvation energy and smaller size of solvated K^+ result in fast diffusion kinetic and high rate capability of KIBs[172]. Moreover, Al foil can be used as current collector in both NIBs and KIBs at low potential. On the contrary, undesirable Li alloy is forming with Al[173-174], which obliges the use of the more expensive and heavy Cu foil instead of Al in LIBs. Compared with MBs, higher rate capability is expected for KIBs due to faster solid state diffusion of potassium. Similar to MBs, KIBs are still in their infancy and face large challenges to develop electrode materials for their commercial application. To date, only limited cathode and anode material have been reported as described in Chapter 1 (**1.3.4**). Orthorhombic layered V_2O_5 materials are very promising for the application in KIBs, due to their high capacity and working voltage in LIBs. So far, few works focus on the study of layered V_2O_5 materials. Tian et al.[209] reported about a crystalline V_2O_5 and

V_2O_5·$0.6H_2O$ xerogel cathode, where V_2O_5 has a discharge capacity of only 44.3 mAh g^{-1} at 50 mA g^{-1}. Very recently, amorphous V_2O_5/carbon nanotube sponge was reported by Ye and coauthors[210], which exhibited an initial discharge capacity of 206 mAh g^{-1} at 5 mA g^{-1}. However, only limited capacities have been obtained for V_2O_5 material in KIBs and a detailed storage mechanism of V_2O_5 upon K-ion insertion/extraction is still missing.

As far as we know, *in operando* techniques, namely, *in operando* synchrotron diffraction and *in operando* X-ray Absorption Spectroscopy (XAS), have not yet been employed to look into the detailed storage mechanism of V_2O_5 materials in KIBs. As demonstrated by first-principles calculations, the migration barrier of K^+ in monolayer V_2O_5 is reduced to 0.39 eV, that is much lower than in bulk V_2O_5 (1.66 eV)[277, 314]. Nanostructured V_2O_5 materials are prepared to enhance the electrochemistry of V_2O_5 cathode and to investigate the reaction mechanism during cycling. In this chapter, we investigated the electrochemical property of V_2O_5 nanoparticles in 1M KPF_6/PC and its storage mechanism by *in operando* synchrotron diffraction and *in operando* X-ray absorption spectroscopy (XAS).

4.2 Experimental

Synthesis of V_2O_5 nanoparticles: The V_2O_5 nanoparticles were synthesized with the same method as described in the experimental part in Chapter 3 (**3.2**) except for an intermittent stirring step. Typically, 1.0 ml of 2 M HCl, 0.3 g of ammonium metavanadate (NH_4VO_3), and 0.5 g of surfactant P123 ($EO_{20}PO_{70}EO_{20}$, where EO and PO represent ethylene oxide and propylene oxide, respectively) were mixed into 30 ml of deionized water under ultrasonication for 10 minutes and stirring for 1 h. After that, the mixed solution was transferred to a 50 ml Teflon-lined autoclaves and maintained at 120 ^{o}C for 24 h with intermittent stirring in an oven. The resulting precipitates were filtered and washed with water and acetone several times, then dried under vacuum at 120 ^{o}C for 24 h. The product was annealed at 400 ^{o}C for 2 h in air with a heating rate of 10 ^{o}C/min.

Preparation of electrolyte: The preparation of electrolyte was carried out in glovebox under Ar atmosphere with very low H_2O and O_2 content (<2 ppm). 1 M KPF_6/Propylene carbonate (PC) electrolyte was prepared by dissolving a corresponding amount of KPF_6 powder in Propylene carbonate with vigorous stirring at room temperature in the glovebox. All these chemicals were water free grade and purchased from Sigma-Aldrich.

Morphological and Structural Study: The morphology was studied with a Zeiss Supra 55 Scanning Electron Microscope (SEM) with primary energy of 15 keV. The structural characterization was done using synchrotron radiation (λ = 0.4131 Å, 30 keV) at the Material Science and Powder Diffraction beamline (MSPD) at ALBA synchrotron (Barcelona, Spain)[266]. The powder diffraction patterns were measured in capillary geometry with powders filled in 0.5 mm Ø boro-silicate capillary. A LabRam Evolution HR FROM Horiba equipped with Nd: YAG laser (633 nm, 100 mW) and a CCD detector (Horiba) was used to collect the Raman scattering of the samples. Meanwhile, a 600 grating was used to split the measurement signal with a ×100 objective (NA 0.95) for all the pristine and cycled samples. Each Raman spectrum was collected for 30 seconds with laser source of 10 mW. In addition, the discharged and charged electrodes were sealed in an *in situ* Raman cell with a quartz window inside a glovebox for Raman measurement. For transmission electron microscopy (TEM) measurements, all samples were prepared under an argon atmosphere inside a glovebox. The samples dispersed onto a carbon-coated grid by dry powder deposition were transferred to the TEM by using a Gatan TEM vacuum transfer holder. The TEM samples were examined using a Titan 80–300 electron microscope (FEI), equipped with a CEOS image spherical aberration corrector, high angle annular dark field (HAADF) scanning transmission electron microscopy (STEM) detector and a Tridiem Gatan image filter (GIF). The microscope was operated at an accelerating voltage of 300 kV.

Electrochemical Characterization: The electrode slurry/mixture was prepared by mixing the active material based on V_2O_5 nanoparticles, with Super C65 C (TIMCAL) and polyvinylidene difluoride (PVDF) binder in a ratio of 70:20:10 with N-Methyl-2-pyrrolidone solvent. The slurry was coated on Al foil of 15µm and dried at 70 ^{o}C overnight. The electrodes were cut into 12 mm diameter and were dried in the vacuum oven at 110 °C for 12h. The electrochemical performance was studied in 2032-type coin cell using potassium anode and V_2O_5 cathode with Whatman separator in 1 M KPF_6/PC electrolyte in glovebox filled with Ar. Galvanostatic cycling experiments were conducted with a rate of C/12 on a multichannel electrochemical workstation (Bio-Logic VMP) the (theoretical capacity is calculated based on the insertion of 2 mol K^+ per V_2O_5). For *ex situ* Raman and XPS, the cells were disassembled after cycling and the electrodes were washed with PC in Ar-filled glovebox. Specifically, two samples were prepared: at 1.5 V after the 1st discharge (K-insertion) and at 4.0 V after the 1st charge (after K-deinsertion).

***In operando* synchrotron diffraction and *in operando* X-ray absorption spectroscopy:** *In operando* synchrotron diffraction was performed at Material Science and Powder Diffraction beamline (MSPD) at ALBA synchrotron. The *in operando* cells were built using 2025-type coin cells with glass windows of 5 mm diameter beam entrance. The cathode was prepared by pressing the electrode mixture on Al mesh having a 5 mm hole in the center. In the same way, the anode was prepared by sticking a metallic K on Al mesh with a 5 mm hole in the center. More details of this setup can be found in Chapter 2[28]. *In operando* synchrotron diffraction data were collected at room temperature with radiation λ= 0.4131 Å wavelength (30keV) and position sensitive detector MYTHEN. Data were collected with effective exposure time of 60 s in steps of 0.006^o over angular range of 1.8^o - 42^o in 2theta during the first cycles with C/15 rate. The coin cells were continuously oscillated +/-5^o around the incoming beam direction to improve the powder averaging (increasing the number of crystallites contribution). The diffraction data analysis was carried out by the Rietveld method using the Fullprof software package[287].

In operando XAS measurements were performed at synchrotron beamline P65 at PETRA III (DESY, Hamburg). The galvanostatic charge and discharge cycle was performed at C/14 rate in 2025-type coin cells with 5mm-diameter Kapton window. XAS spectra of vanadium were recorded in quick-XAS (6 min/spectrum) mode in fluorescence geometry using PIPS (passivated implanted planar silicon) diode. The V K-edge for V_2O_5 was measured during the 1st cycle. The energy was calibrated utilizing a vanadium foil as commonly applied in XAS experiments. V_2O_3, VO_2, and V_2O_5 were used as standard materials. All the data were collected at room temperature with a Si(111) double crystal monochromator (DCM) and all the XAS spectra were processed using the DEMETER software package[289].

4.3 Results and discussion

4.3.1 Structural and morphological characterization

Figure 4.1 displays the synchrotron diffraction pattern of pristine V_2O_5 nanoparticles, suggesting the high crystallinity of V_2O_5 nanoparticles. All reflections can be indexed in the orthorhombic α-V_2O_5 with space group $Pmn2_1$, and the lattice parameters are a=11.509 Å, b=4.374

Å, and *c*=3.564 Å, in consistecy with a previously reported work[40]. Scanning electron microscopy (SEM), inset image in **Figure 4.1**, confirms that the V_2O_5 is consisting of nanoparticles.

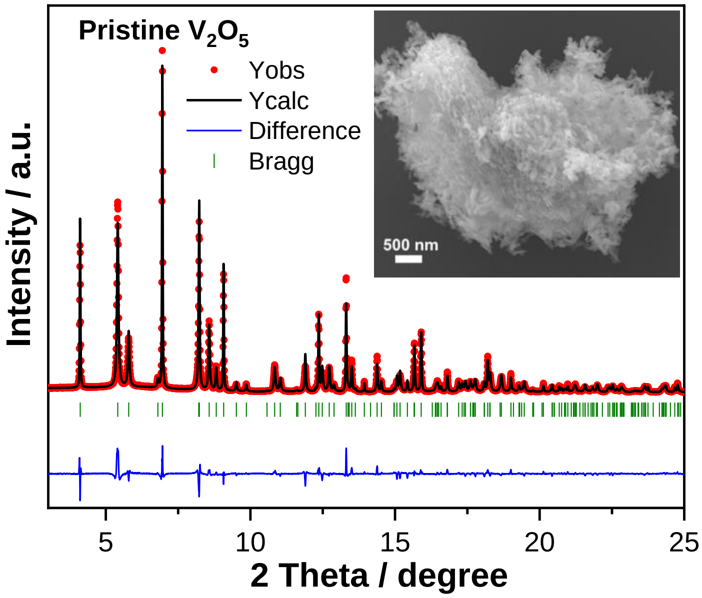

Figure 4.1 Rietveld refinement from synchrotron diffraction data of V_2O_5 nanoparticles (inset: SEM image)

4.3.2 Electrochemical properties

Figure 4.2a displays the voltage-capacity curves of the V_2O_5 nanoparticles based electrode in 1 M KPF_6/PC electrolyte with a rate of C/12 in the potential range of 1.5 - 4.0 V vs K^+/K. During the first discharge, a short slope is observed until around 1.8 V, followed by a long plateau at about 1.7 V. In contrast, only one slope can be observed up to 4.0 V during the first charge process. During the second cycle, only sloped curves can be observed, while a pair plateau of 2.6 V/2.85 V can be seen in the 5th cycle for the discharge and charge process, respectively. Although the discharge-charge capacities in the first cycle are high (200 mAh g^{-1}, corresponding to the insertion of 1.36 K^+)/217 mAh g^{-1}, the cell shows a continuous capacity loss delivering a discharge capacity of 94 mAh g^{-1} for the 5th cycle. The discharge capacity reaches the minimum value of 54 mAh g^{-1} at the 31st cycle. After that, it slowly increases up to 80 mAh g^{-1} at the 200th cycle, as shown in **Figure 4.2b**.

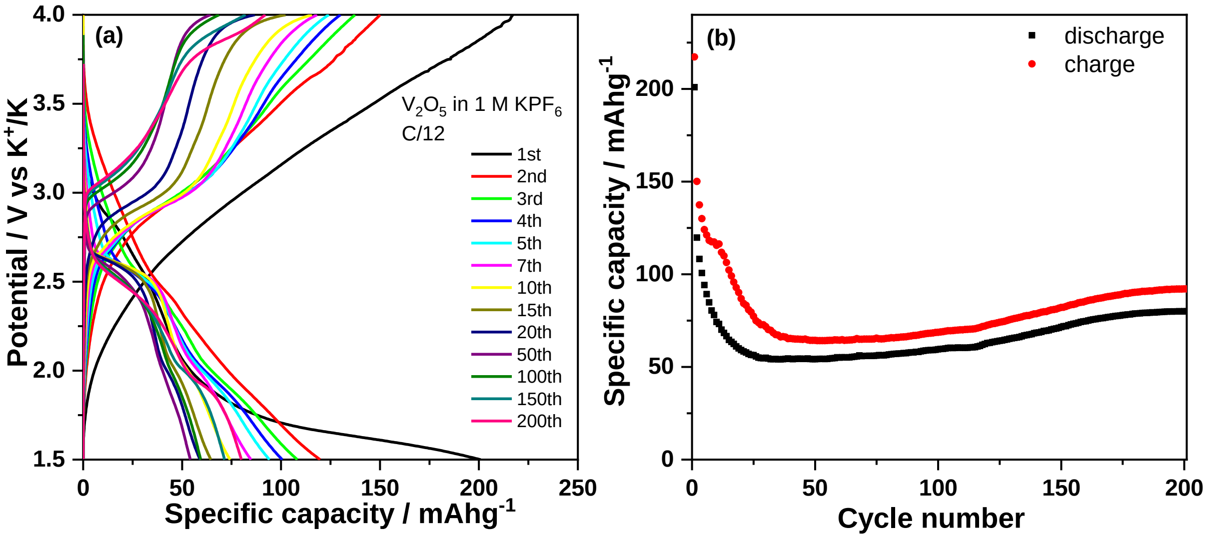

Figure 4.2 Discharge-charge profiles (a) and cycling property (b) of V_2O_5 nanoparticles in 1 M KPF_6/PC (C/12)

4.3.3 Electrochemical mechanism

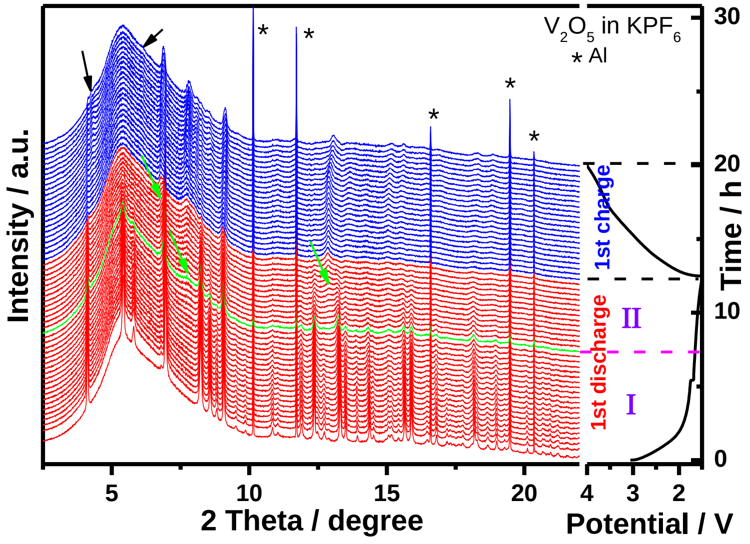

Figure 4.3 *In operando* synchrotron diffraction of V_2O_5 during the first cycle and the corresponding voltage profile at a rate C/15

In order to elaborate the electrochemical storage mechanism upon K ions insertion and extraction in V_2O_5, *in operando* synchrotron diffraction was collected during the first discharge-charge processes as shown in **Figure 4.3**. At the initial stage of discharge (before starting the electrochemistry), all reflections except those marked with Asterisk from Al could be indexed on an orthorhombic α-V_2O_5 phase crystallized in space group *Pmn*2₁ (see in **Figure 4.4a** for the

Rietveld refinement of pristine V_2O_5). In the beginning of the 1st discharge (K insertion, **Region I** with a capacity up to 89 mAh g^{-1}), some reflections of V_2O_5, such as 5.41°, 6.96°, 8.58°, 9.07°, 13.30°, 13.94°, 14.37°, 15.66°, and 15.90°, gradually shift to lower angles, indicating a solid solution process with an expansion of the unit cell till the stoichiometry $K_{0.6}V_2O_5$. In contrast, other reflections such as 4.11°, 5.79°, 6.80°, 8.24°, 8.82°, 9.86°, 10.85°, 11.04°, 12.37°, and 13.51°, keep in the same position and their intensities also slowly reduce. Along with further K ions insertion (1.65V, **Region II**), the reflections continuously shift to lower angles or keep in the same positions, while three new broad reflections, 6.78°, 7.75°, and 12.86° (pointed out by green arrows), appear. The intensities of the new reflections slowly increase until the end of first discharge at the lower limit potential cut-off of 1.5 V, indicating a coexistence of two-phase transition and solid solution mechanisms of insertion. Among all reflections, the one at 7.75° emerges at the potential of 1.65 V when 0.6 mol of K^+ per mol V_2O_5 (89 mAh g^{-1}) is inserted. At the end of discharge at 1.5 V (189 mAh g^{-1}), most of the reflections related to the initial V_2O_5 disappear and only some broad reflections related to the $K_xV_2O_5$ phase (x=1.28) can be observed (see the diffraction at discharged state of 1.5 V in **Figure 4.4b**, pattern 69th), which might be attributed to the dissolution of V_2O_5 into the electrolyte or the formation of a $K_xV_2O_5$ compound with low crystallinity. The crystal structure of the new phase has not yet been clarified. Unfortunately, the diffraction data are not good enough to perform Rietveld refinement and to determine the new phase formed at the end of discharge.

During the 1st charge, two broad new reflections at 4.13° and 6.11° emerge (pointed out by black arrows in **Figure 4.3**) and their intensities increase. At the same time some reflections, such as 6.79°, 6.90°, 7.73°, 8.04°, 9.03°, 12.85°, 13.56°, and 15.01°, shift to higher angles and slightly grow up. The other small broad peaks keep unchanged. The reflections cannot recover to its initial positions of pristine V_2O_5, suggesting irreversibility of the V_2O_5 material during K ions insertion/extraction (see **Figure 4.4b**). Obviously, the K insertion/extraction into V_2O_5 occurs via different reaction mechanism comparing to Li ions insertion in LIBs, where α-, ε-, δ-, γ-, and ω-phase can be observed depending on the amount of inserted Li-ions (x)[15, 70-72]. Particularly, in LIBs, the α-phase ($x<0.1$) and ε-phase ($0.35<x<0.7$) are fully reversible and the δ-phase is observed when x is 1 for $Li_xV_2O_5$. An irreversible transformation of δ-phase into γ-phase is observed when x is over 1, and the γ-phase can be reversibly cycled in the range of $0 \leq x \leq 2.0$, while maintaining the γ-type structure.

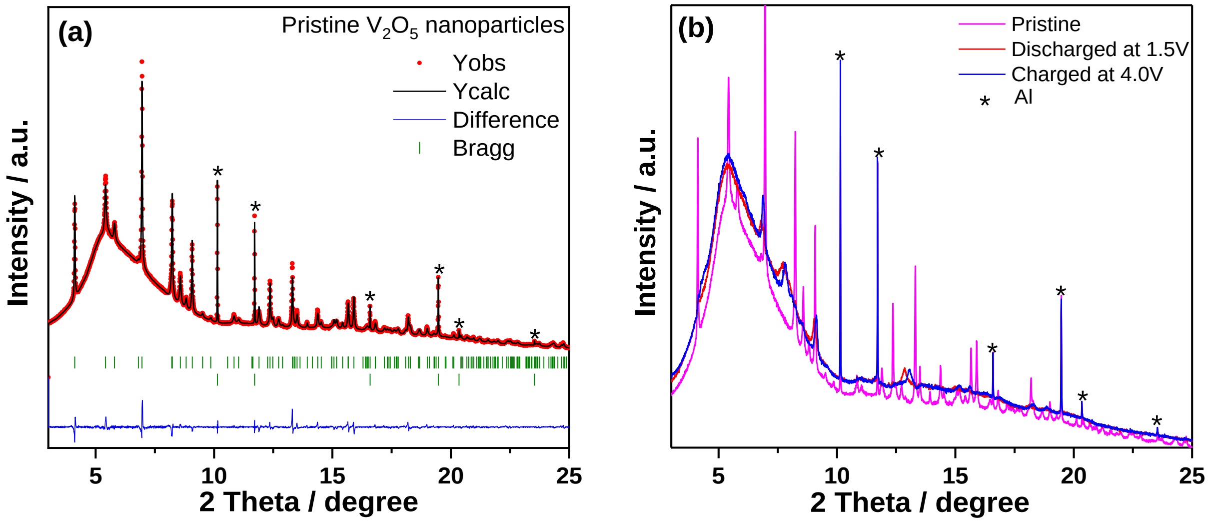

Figure 4.4 Rietveld refinement of the pristine V_2O_5 (a), the comparison of discharged at 1.5 V and charged at 4.0 V with pristine V_2O_5 (b),

In operando XAS was performed on the V_2O_5 cathode material to probe the electronic and structural environments of V-ions during the electrochemical process. As displayed in **Figure 4.6**, the edge position of V K-edge spectrum of the material at the initial state (i.e. OCV) is slightly lower than that of reference V_2O_5 spectrum, where V_2O_5, VO_2, and V_2O_3 are referred as standard materials with +5, +4, and +3 oxidation states, respectively. Hence, it can be confirmed that the oxidation state of V is mainly +5 in the initial state. Moreover, an intense pre-edge peak on XANES data is observed for the V K-edge of pristine V_2O_5, which is due to the transitions from 1s to bound p-hybridized d-states[299-300], with the loss of the centrosymmetric nature of V site. The orthorhombic crystal structure V_2O_5 is composed of square pyramids [VO_5] layers by sharing corners and edges. The V-ions are five-fold coordinated by oxygens in a distorted tetragonal pyramid as shown in **Figure 1.2**.

During the first discharge, the edge position of V K-edge continuously shifts to lower energy, suggesting the reduction of vanadium ions due to the insertion of K ions into the V_2O_5 structure. The edge position of the V K-edge related to the electrode discharged to 1.5V (x=0.91 in $K_xV_2O_5$) is almost in the middle between that of standard VO_2 and V_2O_5, which is in good agreement with the electrochemical data (**Figure 4.5**). Meanwhile, the pre-edge peak (A in **Figure 4.6a**) slowly shifts to lower energy and its intensity gradually decreases, implying the reduction of the vanadium and the changes of the local V environments during K^+ insertion, owing to the co-existence of distorted tetragonal pyramid and centrosymmetric VO_6 octahedral. The edge resonance (B and B' in **Figure 4.6**) related to the energy absorption by core electrons[300-301] does not show remarkable changes in both shape and intensity. This result is quite different from that obtained with V_2O_5 in MBs (Chapter 3). Furthermore, only one distinct isosbestic point[302] (red arrows in **Figure 4.6a**) is obtained at ~ 5474 eV energy for the discharge process, implying the two-phase reaction upon K ions insertion into the V_2O_5, in agreement with the result obtained from the *in operando* synchrotron diffraction.

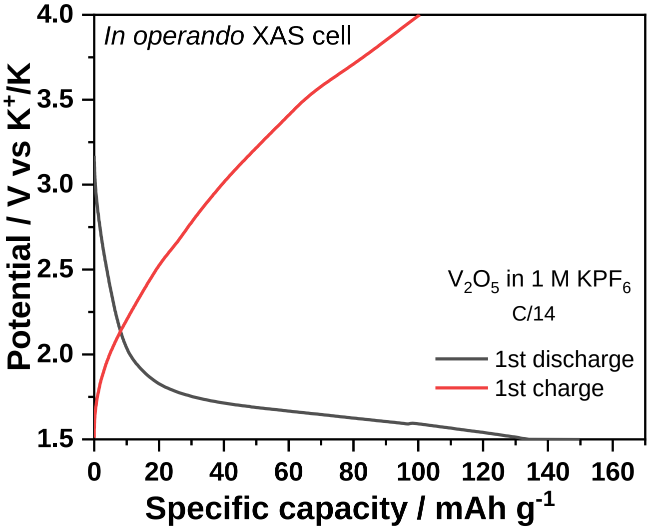

Figure 4.5 Discharge-charge profiles of V_2O_5 in 1 M KPF_6 electrolyte for *in operando* XAS (C/14)

During the first charge (K de-insertion), both the edge position of V K-edge and pre-edge peak (A' in **Figure 4.6b**) exhibit a reversible behavior and shift to higher energy, indicating the oxidation of V in the material. The intensity of pre-edge peak continuously increases during the K ions extraction from the materials, indicating the reduction of the symmetry of the V ions. Moreover, one distinct isosbestic point (red arrows in **Figure 4.6b**) is also obtained at ~ 5474 eV energy in the charge process, indicating a two-phase reaction upon K ions extraction from the structure. However, the edge position of V K-edge and pre-edge peak at the charged state of 4.0V do not return to their initial positions and are slightly lower than that related to the pristine V_2O_5, which is consistent with the *in operando* synchrotron result and suggests an irreversible process.

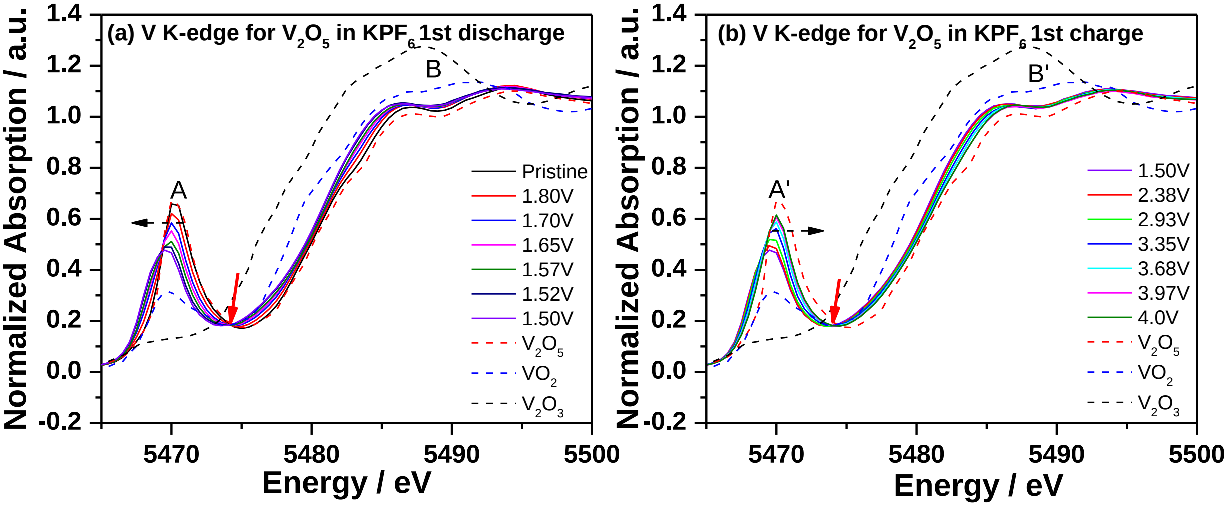

Figure 4.6 *In operando* V K-edge XANES spectra during the 1st cycle in 1 M KPF_6; the isosbestic points are indicated by red arrows.

To further study the local structure of the material upon K ions insertion/extraction, Raman spectra were collected on pristine, potassiated and depotassiated V_2O_5 electrodes, as shown in **Figure 4.7** As known in the pristine orthorhombic V_2O_5, oxygen atoms occupy four types of sites in a [VO_5] slab, denoted as O(1)–O(4). The detailed Raman peaks are clearly described in **Chapter 3** (3.3.3) and these results are consistent with previous works[171, 303]. After K ions insertion (1st discharge), significant changes can be observed and some peaks related to V_2O_5 at 994, 528, and 284 cm^{-1} become weak and broad, while those at 701, 304, and 284 cm^{-1} completely disappear. Meanwhile, some broad and distinct new peaks appear at 226, 340, 455, 763, 880, and 931 cm^{-1}. Similarly, these significant changes in the Raman spectra are also obtained on V_2O_5 after Mg ions insertion, as reported in Chapter 3 (3.3.3). Hence, these new peaks might be ascribed to the new phase of $K_xV_2O_5$, where the broad peaks are probably attributed to the disordered local structure in the $K_xV_2O_5$ phase. It can be deduced that K ions are inserted into the interlayer of V_2O_5 crystals and bonded with oxygen atoms ([KO_6] octahedra) in the V_2O_5 structure to form the K-rich $K_xV_2O_5$ phase. On the charged sample, after (partial) K ions extraction ($K_{x-y}V_2O_5$), some new peaks observed at 763, 880, and 931 cm^{-1} still remain in the same positions and several additional broad peaks can be observed between 200 to 700 cm^{-1}, suggesting the similar structure of $K_xV_2O_5$ and $K_{x-y}V_2O_5$ and the existence of a second phase in the charged sample. The appearance of peaks at 163 and 996 cm^{-1} indicates the existence of layered structure similar to that of pristine V_2O_5, but the material could not return back to the initial state of V_2O_5 after K ions extraction These results confirm that the K ions insertion leads to the formation of $K_xV_2O_5$ phase and partial irreversibility occurs during the first cycle as identified by *in operando* synchrotron diffraction and XAS.

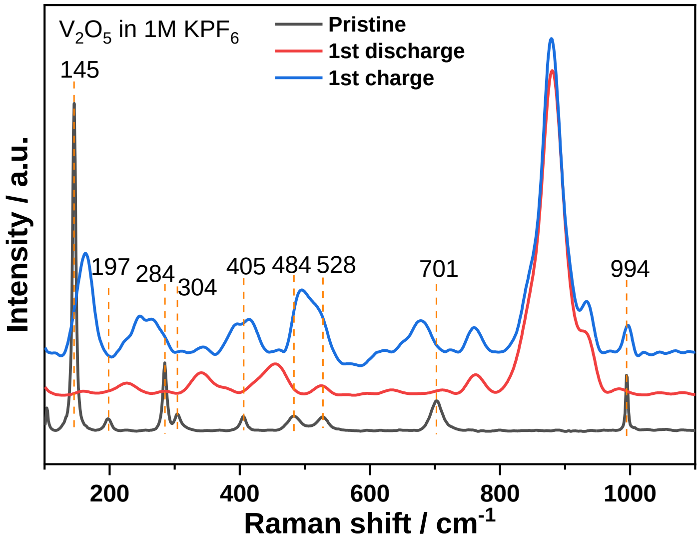

Figure 4.7 Raman spectrum of pristine V_2O_5, 1st discharged V_2O_5, and 1st charged V_2O_5

The microstructural and chemical properties of V_2O_5 before and after discharge/charge were studied by Transmission electron microscopy (TEM). **Figure 4.8a** and **b** display the STEM-HAADF and high resolution TEM images of the pristine V_2O_5, respectively, demonstrating the nanoparticles of V_2O_5. The lattice fringes with a distance of 0.44 nm correspond to the (010) planes of V_2O_5, in good agreement with the result confirmed by Rietveld refinement. **Figure 4.8c** provides the mapping of C, O, K and V, confirming the uniform distribution of K element after insertion into the V_2O_5 crystal structure. **Figure 4.8d** and **e** demonstrate the non-uniform distribution of K element in the V_2O_5 electrode between the surface area and central area after K ions extraction. This result implies that part of K ions still remain in the structure after charging and further confirms the irreversibility of V_2O_5 during cycling.

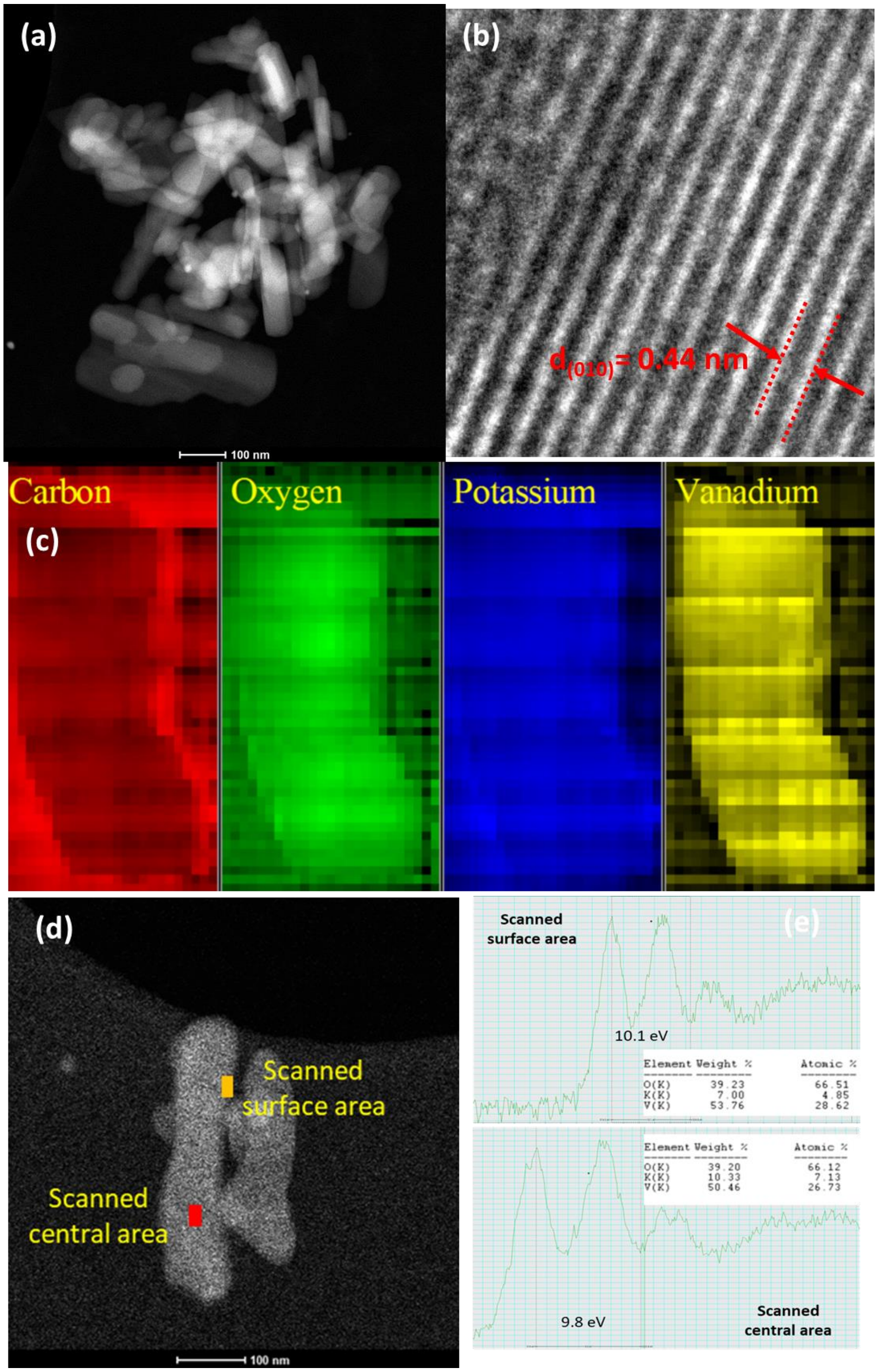

Element	Weight %	Atomic %
O(K)	39.23	66.51
K(K)	7.00	4.85
V(K)	53.76	28.62

Element	Weight %	Atomic %
O(K)	39.20	66.12
K(K)	10.33	7.13
V(K)	50.46	26.73

Figure 4.8 STEM-HAADF and high resolution TEM images of the pristine V_2O_5 (a and b), Mapping of the 1st discharged V_2O_5 (c), and STEM-HAADF and EELS of the 1st charged V_2O_5 (d and e, inset: EDS)

4.4 Conclusion

In conclusion, pure orthorhombic V_2O_5 nanoparticles with high crystallinity were successfully prepared via a hydrothermal approach. In the 1 M KPF_6/PC electrolyte, V_2O_5 nanoparticles deliver an initial discharge/charge capacity of 200 mAh g^{-1} (1.36 K^+)/217 mAh g^{-1} in the potential range of 1.5 - 4.0 V at a rate of C/12. The electrode shows a rapid capacity loss, which drops to 54 mAh g^{-1} after 31 cycles. After that, the discharge capacity slowly increases up to the value of 80 mAh g^{-1} at the 200th cycle. The storage mechanism upon K ions insertion into V_2O_5 is studied by *in operando* synchrotron diffraction and *in operando* XAS. At the beginning, the K insertion goes via solid solution mechanism until 1.65 V. At higher degree of insertion, by further decreasing the potential, it is recognised that a solid solution mechanism and two-phase transition coexist. The analysis of the charge process (K extraction) identifies irreversible processes. *In operando* XAS confirms the reduction/oxidation of vanadium during the K insertion/extraction with part of irreversibility. It is important to notice that V_2O_5 in KIBs displays a completely different electrochemical mechanism from that observed in MBs, which might be attributed to the large size of K ions. The irreversibility of V_2O_5 upon K ions insertion/extraction in KIBs is well identified by *in operando* synchrotron diffraction and *in operando* XAS and *ex situ* Raman and TEM.

Chapter 5 *In operando* study of orthorhombic V_2O_5 as cathode material for rechargeable aqueous Zn batteries

5.1 Introduction

In comparison to the previous discussed technologies, rechargeable aqueous ZBs are much more promising candidates for large-scale EESs due to their high safety, abundant resources, and low cost[19, 215]. Additionally, the nontoxic, inflammable, and water-based electrolyte and low humidity demand during assembly process reduce the manufacturing cost as well[217-218]. Compared with non-aqueous electrolyte (about 1^{-10} mS cm^{-1}), the ionic conductivity of the aqueous electrolyte (up to 1 S cm^{-1}) is much higher[19]. Meanwhile, aqueous electrolytes can lower the activation energy for charge transfer at the electrode/electrolyte interface. The high overpotential for hydrogen evolution on Zn (-0.76 V vs. SHE) makes it stable in water[216]. Meanwhile, the utilization of metallic Zn results in specific capacity of 820 mAh g^{-1} and a volumetric capacity of 5854 mAh cm^{-3}, providing high energy density. To date, many alternative cathode materials for aqueous ZBs have reported as described in the introduction part of the first Chapter (**1.3.4**).

Among them, vanadium-based oxides with open framework show high potential as the cathode materials for aqueous ZBs. As discussed in the introduction part of the first Chapter (**1.3.4**), several vanadium-based oxides are studied as cathode materials. V_2O_5 as a typical layered material is also investigated in aqueous ZBs. For example, Zhou and co-authors[259] recently reported that V_2O_5 shows high performance in 3 M $ZnSO_4$ electrolyte compared within different concentration and in different types of salts like $Zn(NO_3)_2$, $Zn(CH_3COO)_2$, and $ZnCl_2$. It delivers a high capacity of 224 mAh g^{-1} at 100 mA g^{-1} and good cycling stability at high current density of 1 and 2 A g^{-1} in 3 M $ZnSO_4$ electrolyte. Moreover, *ex situ* XRD demonstrated that a new phase of $Zn_xV_2O_5$ is formed upon Zn-ions insertion into V_2O_5. Besides, Zhang et al.[260] reported the study of V_2O_5 as cathode material in aqueous ZBs employing 3 M $Zn(CF_3SO_3)_2$ as electrolyte. In this electrolyte, V_2O_5 exhibits a capacity of 470 mAh g^{-1} at 0.2 A g^{-1} and high capacity retention of 91.1% up to 4000 cycles at 5 A g^{-1}. Moreover, it displays good performance also in rough conditions at both high (50 °C) and low (-10 °C) temperatures. The co-intercalation of hydrated Zn ions into V_2O_5 crystal structure was proposed as well, confirming by *ex situ* XRD, XPS, and TEM. However, a detailed investigation of structural changes of V_2O_5 upon Zn-ion insertion/extraction is still missing and is, therefore, the aim of this work.

5.2 Experimental

Synthesis of V_2O_5 nanowires: V_2O_5 nanowires were prepared via a modified hydrothermal method followed by heat treatment[53, 88]. Briefly, 0.18 g of commercial V_2O_5 powder (Alfa Aesar, 99.99%) was added to 30 ml of deionized water under mechanical stirring for few minutes to form a light orange suspension. Then, 2.5 ml 30 % hydrogen peroxide (H_2O_2) was dropwise added to the above suspension and kept stirring for 30 mins to get a transparent orange solution. The obtained solution was transferred to a 50 ml Teflon-lined stainless-steel autoclave and kept at 190 °C for 4 days. The precipitates were collected and washed with deionized H_2O several times and dried at 80 °C for 12 h. Finally, the product was annealed at 400 °C for 2 h with a heating rate of 5 °C min^{-1} in air atmosphere.

Preparation of electrolyte: The 1 M $ZnSO_4$ electrolyte was prepared by dissolving a corresponding amount of $ZnSO_4 \cdot 7H_2O$ powder in distilled H_2O with vigorous stirring at room temperature.

Morphological and Structural Study: The morphology was studied with a Zeiss Supra 55 Scanning Electron Microscope (SEM) with primary energy of 15 keV. The structural characterization was performed using synchrotron radiation ($\lambda = 0.4132$ Å, 30 keV) at the Material Science and Powder Diffraction beamline (MSPD) at ALBA synchrotron (Barcelona, Spain)[266]. The powder was filled in 0.5 mm Ø boro-silicate capillary and diffraction pattern was collected in capillary geometry.

Electrochemical Characterization: The electrode was prepared by mixing active material V_2O_5 nanowires with Super C65 C (TIMCAL) and polyvinylidene difluoride (PVDF) binder in a ratio of 70:20:10 with N-Methyl-2-pyrrolidone solvent. The dried electrode mixture was pressed on stainless steel mesh of 12 mm and dried at 120 °C overnight under vacuum. CR2032-type coin cells for electrochemical measurements were assembled in air at room temperature. The cells were built with V_2O_5 cathode, Zn foil as anode, 1 M $ZnSO_4$ as electrolyte, and a piece of glass microfiber

(Whatman) as separator. The GCPL and CV measurements were performed between 0.3 and 1.6 V (vs. Zn^{2+}/Zn) on a VMP3 potentiostat (BioLogic) at 25 °C. GCPL were performed at different current densities from 50 to 1600 mA g^{-1} to determine the rate capability of the battery, CV measurements were performed at 0.1 mV/s.

In operando synchrotron diffraction and in operando X-ray absorption spectroscopy (XAS): *In operando* synchrotron diffraction was performed at Material Science and Powder Diffraction beamline (MSPD) at ALBA synchrotron. Electrochemistry was performed in 2025-type coin cell with glass windows of 5 mm diameter beam entrance. The cathode was prepared by pressing the electrode mixture (as described above) on stainless steel mesh within a 5 mm hole in the center, a Zn foil with a 5 mm hole in the center was used as anode. *In operando* synchrotron diffraction was conducted with radiation λ= 0.4132 Å wavelength (30keV) and position sensitive detector MYTHEN. Data were gathered with effective exposure time of 60s in steps of 0.006^o over angular range of 1.8^o - 42^o in 2theta during the first cycles with current density of 50 mA g^{-1}. The coin cell was continuously oscillated +/-5^o around the incoming beam direction to improve the powder averaging (i.e. increasing the number of crystallites contribution). The diffraction data analysis was carried out by the Rietveld method using the Fullprof software package[287]. *In operando* XAS measurements were performed at synchrotron beamline P65 at PETRA III (DESY, Hamburg). Electrochemistry was conducted in 2025-type coin cell with 5mm-diameter Kapton window for the first discharge-charge processes at current density of 50 mA g^{-1}. XAS spectra of Vanadium were recorded in quick-XAS (6 min/spectrum) mode in fluorescence geometry using PIPS (passivated implanted planar silicon) diode. The V K-edge for V_2O_5 was measured during the 1st cycle and the energy was calibrated utilizing a vanadium foil as commonly applied in XAS experiments. V_2O_3, VO_2, and V_2O_5 were used as standard materials. All the data were collected at room temperature with a Si(111) double crystal monochromator and all the XAS spectra were processed using the DEMETER software package[289].

5.3 Results and discussion

5.3.1 Structural and morphological characterization

The crystal structure of the prepared V_2O_5 nanowires was investigated by synchrotron diffraction, as displayed in **Figure 5.1**. All reflections could be indexed to the orthorhombic α-V_2O_5 with space group $Pmn2_1$, and the lattice parameters are a = 11.5143 Å, b = 4.3734 Å, c = 3.5653 Å, which are in good agreement with previous work[40]. The strong intensities of the reflections confirm the high crystallinity of the obtained V_2O_5 nanowires material. The SEM image (inset in **Figure 5.1**) demonstrates that V_2O_5 material is composed of nanowire-like nanostructure with length up to several micrometers.

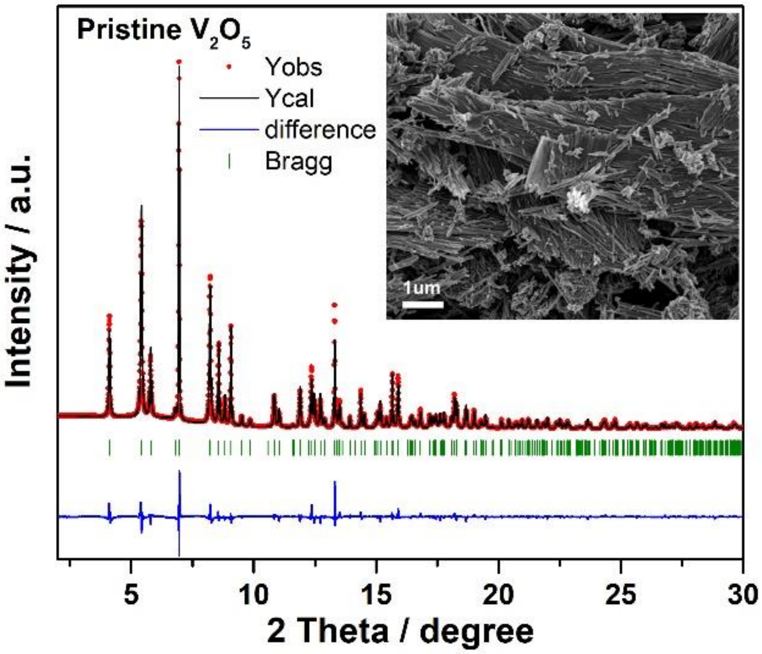

Figure 5.1 Rietveld refinement from synchrotron diffraction data of V_2O_5 nanowires (inset: SEM image)

5.3.2 Electrochemical properties

As displayed in **Figure 5.2a,** the prepared V_2O_5 nanowires were electrochemically evaluated by galvanostatic cycling at a current density of 50 mA g^{-1} and 200 mA g^{-1} in the potential range of 0.30 - 1.60 V vs Zn^{2+}/Zn. The open-circuit voltage (OCV) of the cell is 1.23 V. During the 1st discharge (Zn ions insertion), V_2O_5 nanowires electrode displays a flat discharge plateau at around

1.00 V, followed by a sloping-like plateau at about 0.50 V. During the 1st charge process (Zn ions de-insertion), a sloping-like plateau at 1.0 V and a flat plateau at 1.20 V together with a slope up to 1.6 V can be observed. Compared with the 1st discharge, the 2nd discharge profile shows a shorter plateau at around 1.00 V and similar sloping-like plateau at 0.50 V. In the 2nd charge process, a sloping-like plateau at 1.0 V similar as for the 1st charge is observed, but no clear plateau at 1.20 V can be seen. During cycling, the voltage profiles significantly change, the plateau at 1.20 V disappears and only one slope and a sloping-like plateau at 0.50 V can be observed (see the 5th discharge profile). On the 5th charge profile, two sloping-like plateau at 0.70 V and 1.0 V are observed. The V_2O_5 nanowires electrode delivers an initial discharge and charge capacity of 277 and 432 mAh g^{-1}, respectively, at a current density of 50 mA g^{-1}. It almost reaches its theoretical capacity of V_2O_5 based on the insertion of 1 mol of Zn^{2+} (294 mAh g^{-1}), suggesting the good electrochemical activity in the aqueous Zn battery system. The electrode delivers a discharge capacity of 302 mAh g^{-1} at the 2nd cycle, a value higher than that for the first cycle, which might be due to an activation of the active material, as also reported by other previous studies[219, 255]. The V_2O_5 cathode exhibits a dramatic decrease of capacity during the following 20 cycles at 50 mA g^{-1} (94 mAh g^{-1} for 22nd) and only delivers a discharge capacity of 21 mAh g^{-1} after 100 cycles. Moreover, the cycling stability of V_2O_5 cathode was studied at a higher current density of 200 mA g^{-1}, as presented in **Figure 5.2b**. An initial discharge capacity of 278 mAh g^{-1} is obtained, followed with a sudden capacity decline down to 180 mAh g^{-1} at the 2nd cycle. In the following four cycles, the behavior differs from the electrode cycled at 50 mA g^{-1}: it displays a capacity increase, indicating a long activation process of the active material, which is often observed in cathode materials for aqueous ZBs[219, 255]. However, this activation phenomenon takes more cycles under high current density, demonstrating its possible correlation with the involved chemical ion kinetics during cycling[235].

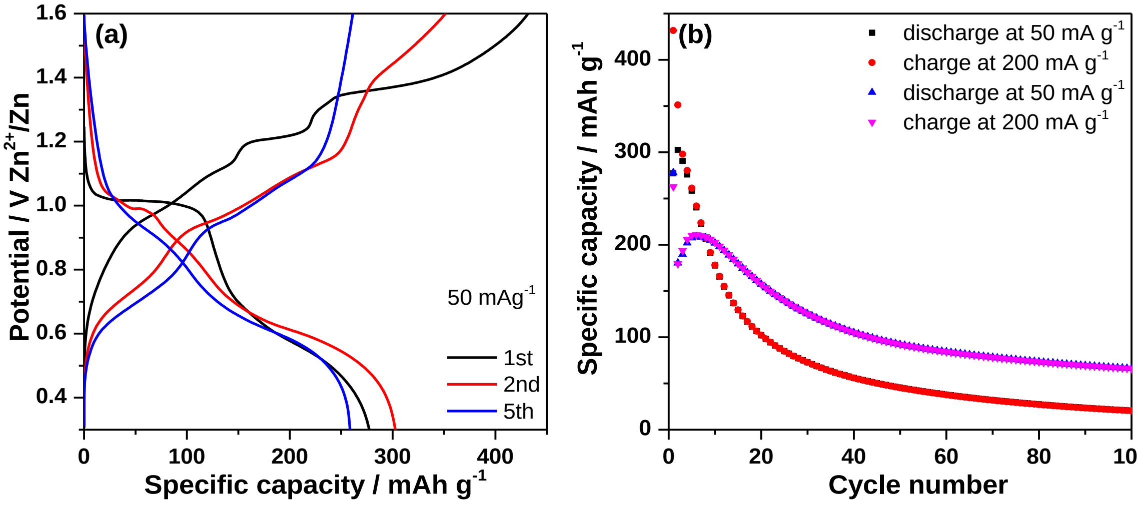

Figure 5.2 Discharge-charge profiles (a) and cycling performance (b) of V_2O_5 nanowires in 1 M $ZnSO_4$

5.3.3 Electrochemical mechanism

In order to clarify the Zn-ion storage mechanism in the V_2O_5 material, CV was performed at a scan rate of 0.1 mV s^{-1} in the voltage range of 0.30 - 1.60 V (vs. Zn^{2+}/Zn). **Figure 5.3** displays two peaks centered at 0.92 and 0.50 V for the 1st reduction process and a broad peak at 1.20 V with a shoulder at 1.05 V for the 1st oxidation process. In the following scans, three features are observed for both reduction and oxidation processes, respectively. The reduction peak at 0.92 V gradually shifts to higher potential, becomes weaker and finally disappears. A new reduction peak at 0.88 V emerges and grows up. The reduction peak at 0.50 V gradually shifts to 0.57 V. A new oxidation peak appears at 0.74 V. The oxidation peak at 1.05 V shifts to 1.00 V after first cycle and increases upon cycling. The oxidation peak at 1.20 V shifts to 1.12 V in the 3rd cycle, this shift is accompanied by decreasing its intensity.

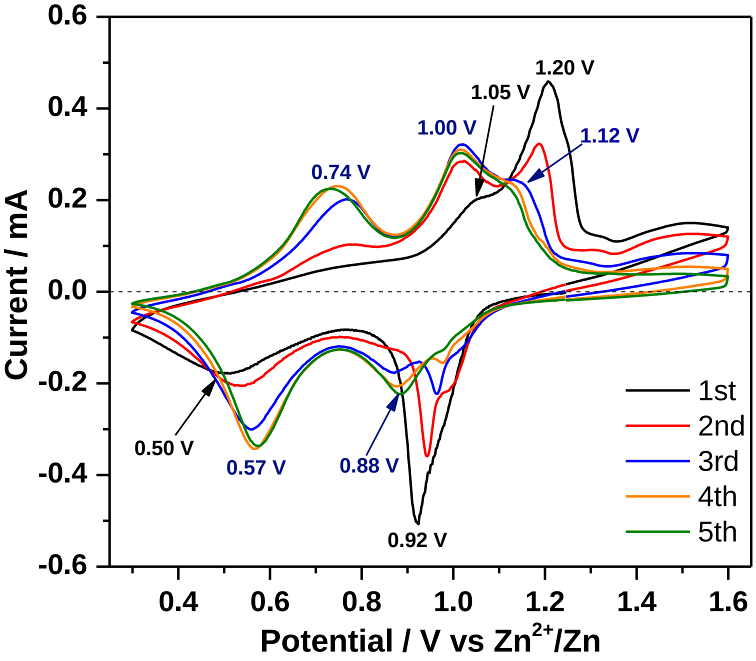

Figure 5.3 CV curves of V_2O_5 nanowires at a scan rate of 0.1 mV s^{-1} in 1 M $ZnSO_4$

To further investigate the structural evolution of V_2O_5 upon Zn-ion insertion/extraction, *in operando* synchrotron diffraction was performed during the initial 1.5 cycles. The selected diffraction patterns and corresponding voltage-time profile are provided in **Figure 5.4**.

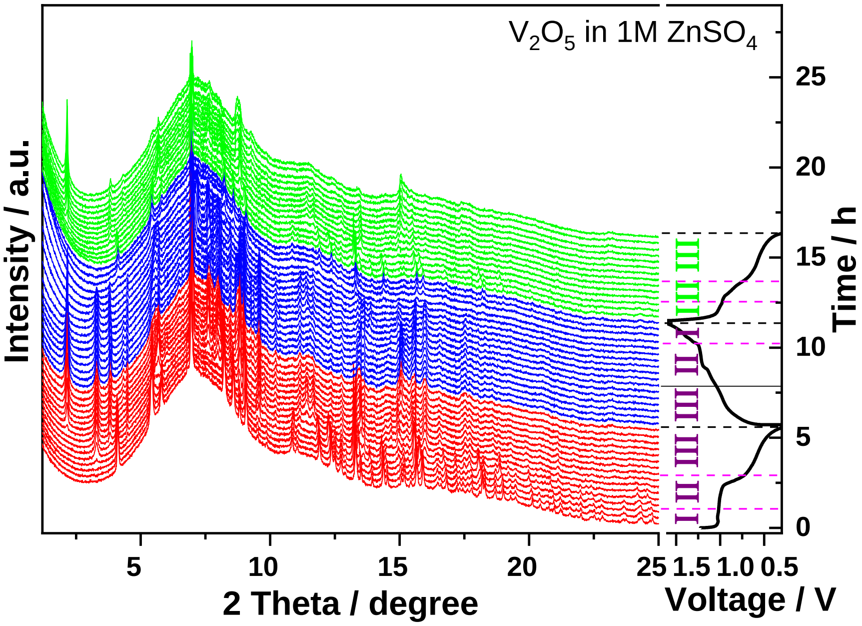

Figure 5.4 *In operando* synchrotron diffraction of V_2O_5 during the first one and half cycles and the corresponding voltage profile at a current density of 50 mA g^{-1}

At the initial stage of discharge, all reflections of the parent material can be indexed on the orthorhombic V_2O_5 in the space group *Pmn2₁* (see **Figure 5.5a** for the Rietveld refinement of pristine V_2O_5). In the beginning of the 1st discharge (**Region I**), most of the characteristic reflections of V_2O_5, such as ones at 4.12°, 6.96°, 8.24°, 8.58°, 9.08°, 11.90°, 12.37°, 13.31°, 14.38°, 15.67°, and 15.91°, continuously shift towards lower 2θ accompanied by a slight reduce of their intensity. Therefore, a solid solution reaction upon Zn ions insertion into the V_2O_5 structure can be proposed up to the stoichiometry $Zn_{0.13}V_2O_5$. While few reflections at 5.42°, 10.85°, and 11.04° slightly shift to high angles, few other reflections at 5.80°, 12.49°, 12.73°, and 16.46° keep in the same positions. Upon discharge capacity of 47 mAh g^{-1} (**Region II**, $Zn_{0.16}V_2O_5$), two small reflections at 3.29° and 7.98° emerge, which belong to a new phase of zinc pyrovanadate, $Zn_3(OH)_2V_2O_7{\cdot}2(H_2O)$ (see **Figure 5.5b** for the Rietveld refinement of 11st pattern at discharged V_2O_5). Other reflections from this phase become visible at 4.49°, 7.78°, 7.99°, 8.46°, 9.57°, 10.20°, 11.16°, 15.97° and 17.54°. At the same time other reflections at 2.16°, 3.82°, 5.67°, 7.01°, 7.61°, 11.39°, and 11.66° appear and grow. These reflections except ones at 3.82° and 7.01° are attributed to the formation of byproduct of $ZnSO_4Zn_3(OH)_6{\cdot}5H_2O$. In addition, the $Zn_{0.22}V_2O_5$ is obtained from the formed phase $Zn_{0.13}V_2O_5$, which was present in **Region I** via a fast solid solution reaction occurring in **Region II** until a discharge capacity of 65 mAh g^{-1} is reached. On the other hand, two reflections at 3.82° and 7.01° may belong to the new phase Zn-rich $Zn_xV_2O_5$ transformed from $Zn_{0.22}V_2O_5$ through two-phase reaction. Meanwhile, the reflections of new phase Zn-rich $Zn_xV_2O_5$ remain their positions unchanged together with the decrease of their intensities of $Zn_{0.22}V_2O_5$. At the end of the **Region II**, most of the reflections from the parent V_2O_5 phase disappear and the new phase grows up. It implies the coexistence of solid solution and two-phase transition during the Zn ions insertions in **Region II**. Therefore, the Zn-rich $Zn_xV_2O_5$ is determined as $Zn_{0.38}V_2O_5$ obtained after the two-phase reaction (capacity of 120 mAh g^{-1}) accompanied with the formation of two byproducts $Zn_3(OH)_2V_2O_7{\cdot}2(H_2O)$ and $ZnSO_4Zn_3(OH)_6{\cdot}5H_2O$. It is worthy to note that the x value is determined without the consideration of the consumption of V_2O_5 to form the byproduct $Zn_3(OH)_2V_2O_7{\cdot}2(H_2O)$ and the possible dissolution of V_2O_5. Upon further Zn ions insertion, most of the reflections maintain their positions along with the increase of their intensities (**Region III**), while only two reflections of $Zn_{0.38}V_2O_5$ at 3.81° and 7.01° shifts to high angles with the increase of intensity and low angle with the decrease of intensity, respectively. It indicates that a solid solution process happens in **Region III** to form a final phase $Zn_{0.94}V_2O_5$ together with the above mentioned two byproducts with a total discharge capacity of 277 mAh g^{-1} (see **Figure 5.5c** for the Rietveld refinement of 36th pattern at first fully discharged V_2O_5). During the 1st charge, the reflections undergo in a reverse way except the appearance and disappearance of a small reflection at 7.17°. The reflections return back to their original positions as the pristine V_2O_5 but with much less intensities (see **Figure 5.5d** for the Rietveld refinement of 69th pattern at fully charged V_2O_5). This is possibly caused by the amorphization of the crystalline active material or by the vanadium dissolution in the electrolyte[245, 249]. Interestingly, both byproducts disappear along with the 1st charging process. The evolution of the reflections in the 2nd discharge is analogous to that during the 1st cycle. Briefly, in **Region I**, the reflections show the same behavior as those for the first discharge process, suggesting a solid solution reaction. In **Region II and III**, the electrode undergoes the same process (a two-phase transition and solid solution, respectively) as that observed in the first discharge, but without the appearing of the reflections related to the byproduct $Zn_3(OH)_2V_2O_7 \cdot 2(H_2O)$ (see **Figure 5.5e** for the Rietveld refinement of 97th pattern at the 2nd fully discharged V_2O_5). Moreover, the other byproduct is also observed as can be seen in the first discharge process. Indeed, the $Zn_3(OH)_2V_2O_7 \cdot 2(H_2O)$ has an open layered structure and has been used as cathode materials in aqueous ZBs with a high capacity of 213 mAh g^{-1} at 50 mA g^{-1} reported by Alshareef et al.[239], who shows a shift of the reflection 001 during Zn ions insertion and extraction[239]. This means that the presence of $Zn_3(OH)_2V_2O_7 \cdot 2(H_2O)$ can be beneficial for the material capacity. However, in our case, the shift of the 001 reflection is not observed and the reason is still unknown yet. The new phase $Zn_3(OH)_2V_2O_7 \cdot 2(H_2O)$ was also found in a recent work related to an aqueous Zn-V_2O_5 battery[315]. The phase $Zn_3(OH)_2V_2O_7 \cdot 2(H_2O)$ is formed because of the two-phase transition and then being as host structure for Zn ions storage, also with a shift of reflection 001 during Zn ions insertion. Furthermore, it has been reported that complex byproducts, like $ZnSO_4Zn_3(OH)_6 \cdot xH_2O$[237, 248, 251] were produced and decomposed during discharge-charge cycling when applying a $ZnSO_4$ based aqueous electrolyte.

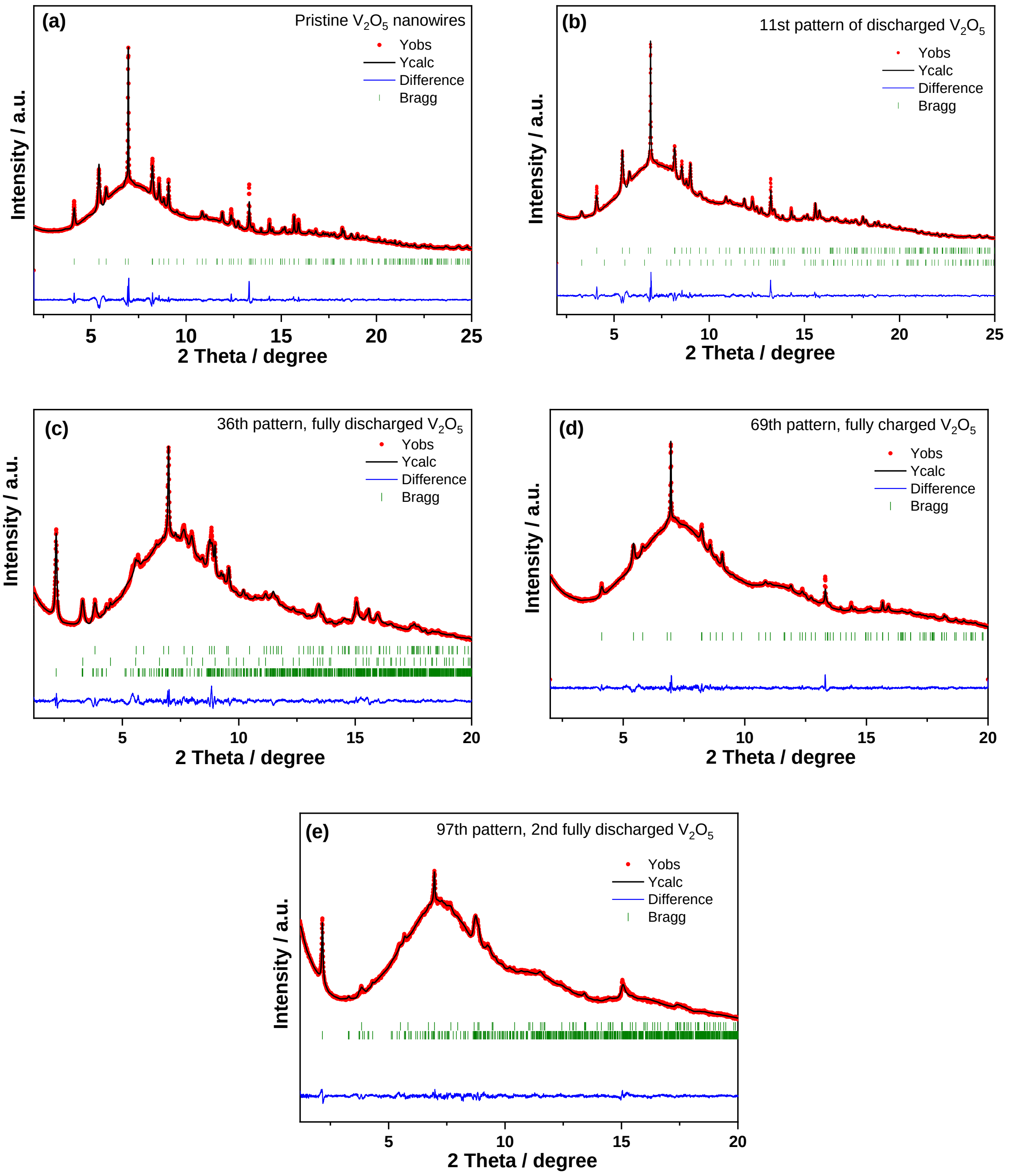

Figure 5.5 Rietveld refinement of the pristine V_2O_5 (a), discharged state in the beginning of Region II with capacity of 47 mAh (11^{st} pattern) (b), first fully discharged V_2O_5 electrode at 0.3 V(36^{th} pattern) (c), fully charged at 1.6 V(69^{th} pattern) (d), and 2^{nd} fully discharged V_2O_5 electrode at 0.3 V(97^{th} pattern) (e)

In order to investigate variation of the oxidation state and the local electron environment of vanadium during the discharge/charge (i.e. Zn insertion/extraction) process, *in operando* XAS was performed on the V_2O_5 nanowires cathode within an *in operando* coin cell. **Figure 5.6** shows the normalized V K-edge XANES spectra collected during the initial discharging and charging processes with those references spectra of standard vanadium oxides, where V_2O_5, VO_2 and V_2O_3 have oxidation state of +5, +4, and +3, respectively. The edge position of V K-edge in the pristine V_2O_5 cathode overlaps with that of standard V_2O_5 reference, indicating that the oxidation state of V in V_2O_5 is +5. Moreover, an intense pre-edge peak for the V K-edge of pristine V_2O_5 is observed, which is ascribed to the transitions between the 1s and bound p-hybridized d-states[299-300]. Along with progressive discharging, the main absorption edge shifts towards lower binding energies, confirming the reduction of the oxidation state of vanadium upon the Zn-ion intercalation. Meanwhile, the pre-peak (A in **Figure 5.6a**) also shifts gradually to lower binding energy with the simultaneous decrease of intensity, confirming the reduction of V and the deformation of the local V environments during Zn ions insertion. This is due to the co-existence of distorted tetragonal pyramid and centrosymmetric VO_6 octahedral. The edge resonance (B in **Figure 5.6a**) displays distinct changes in both intensity and shape, which is caused by the energy absorption of core electrons[300-301]. During the discharge process, two broad peaks centered at 5494 eV and 5507 eV shift to lower energy with the decrease of their intensities and change into a very broad peak centered at 5500 eV from initial stage to 0.99V (peak B in **Figure 5.6a**). After that, the formed broad peak centered at 5500 eV with the peak at 5486.5 eV continuously shift to lower energy accompanying with the increases of both intensities (from 0.99V to 0.3V). Moreover, two distinct isosbestic points[302] at ~ 5474 eV and ~5502 eV (red arrows in **Figure 5.6a** and **b**) are obtained during both discharge (from 0.99 V to 0.3 V) and charge (from 0.3 V to 1.32 V) processes. This suggests the two-phase transition upon the Zn ions insertion/extraction into/from V_2O_5 structure, which corresponds to the two-phase region as proved through *in operando* synchrotron diffraction. At the fully discharged state of 0.30 V, the edge position of V K-edge lies almost in the middle of the spectra of standard V_2O_5 and VO_2, suggesting that the oxidation state of V is very close to V^{4+}, in good agreement with the electrochemistry data (see **Figure 5.7**). However, its edge position does not completely overlap with the spectrum of VO_2, that could be mainly due to the different symmetry/structure between the discharged sample (x=1.00 in $Zn_xV_2O_5$) and the selected standard. During the charge process (Zn-ion extraction), a completely reversible behavior can be observed. Pre-peak and edge resonance (A' and B' in **Figure 5.6a** and **b**) also show a reversible process. At the fully charged state of ~1.6V, the V spectrum returns back to its initial state, indicating that the V ions are fully oxidized to its oxidation state of +5. The evolution of V K-edge spectra reveals that the V ions are reduced and reversibly oxidized during the Zn-ion intercalation and extraction, respectively, accompanied by the local structure changes of V ion, as fully proved by *in operando* synchrotron diffraction.

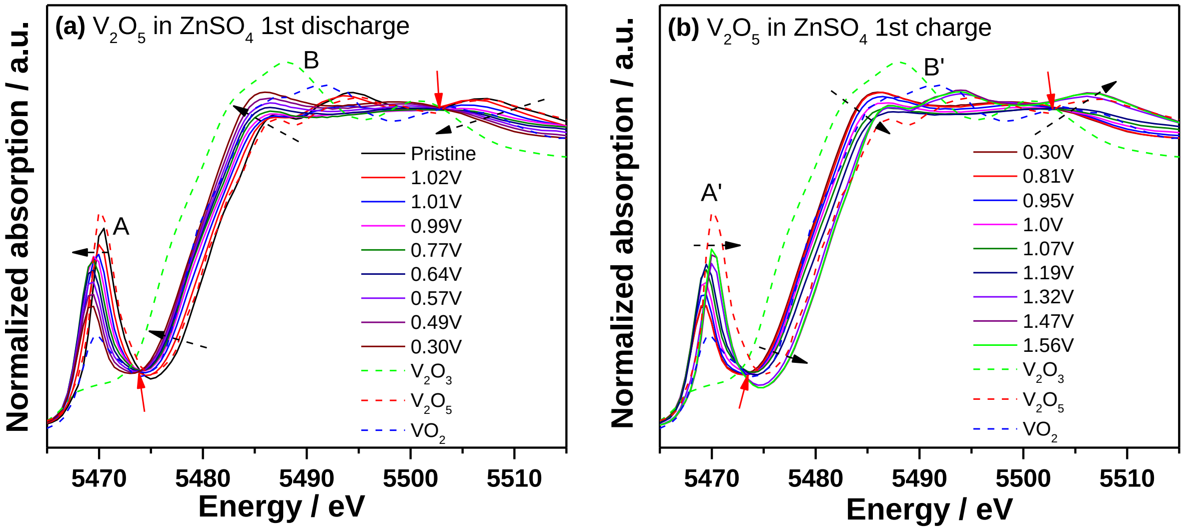

Figure 5.6 *In operando* V K-edge XANES spectra during the 1st cycle in 1 M $ZnSO_4$; the isosbestic points are pointed out by red arrows.

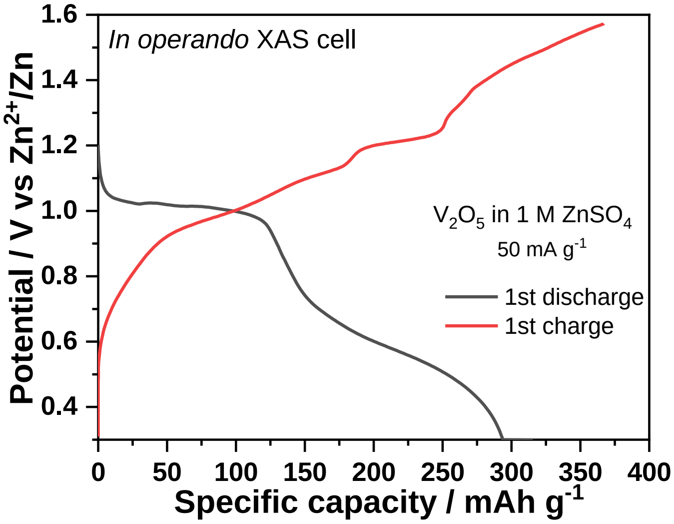

Figure 5.7 Discharge-charge profiles of V_2O_5 in 1 M $ZnSO_4$ electrolyte for *in operando* XAS (50 mA g^{-1})

5.4 Conclusion

In summary, orthorhombic V_2O_5 nanowires were easily prepared via a hydrothermal approach. In the 1 M $ZnSO_4$ electrolyte, V_2O_5 nanowires deliver an initial discharge/charge capacity up to 277 and 432 mAh g^{-1}, respectively, at a current density of 50 mA g^{-1}, which almost reaches the theoretical capacity based on 1 mol of Zn^{2+} insertion per V_2O_5 (294 mAh g^{-1}). The V_2O_5 cathode exhibits a dramatic decrease of capacity during the following 20 cycles at 50 mA g^{-1} (94 mAh g^{-1} for 22nd) and delivers a very low discharge capacity of 21 mAh g^{-1} after 100 cycles. Moreover, it delivers an initial discharge capacity of 278 mAh g^{-1} at 200 mA g^{-1}, followed by an activation process of the active material. CV displays, in the first scan, two reduction peaks centered at 0.92 and 0.50 V and a broad oxidation peak at 1.20 V with a shoulder at 1.05 V. In the following scans, the CV curves reveal significant changes in both reduction and oxidation peaks, respectively. Briefly, the reduction peak at 0.92 V disappears and a new reduction peak at 0.88 V grows up while the reduction peak at 0.50 V gradually shifts to 0.57 V. On the other hand, the oxidation peaks at 0.74 V and 1.05 V rises up, while, especially the oxidation peak at 1.20 V becomes a small shoulder of the peak at 1.00 V, with a notable current peak decrease. *In operando* synchrotron diffraction reveals that V_2O_5 first undergoes a solid solution and then a coexistence of solid solution and two-phase reaction upon Zn ions insertion. Meanwhile it also confirms the formation of two byproducts $Zn_3(OH)_2V_2O_7 \cdot 2(H_2O)$ and $ZnSO_4Zn_3(OH)_6 \cdot 5H_2O$ during the Zn ions insertion. The electrode undergoes a reversible progress upon Zn ions extraction with the decomposition of both byproducts. The V_2O_5 electrode, in the 2nd discharge process, goes through the same two-phase reaction as that in the 1st discharge without the formation of the byproduct $Zn_3(OH)_2V_2O_7 \cdot 2(H_2O)$. *In operando* XAS confirms the reduction/oxidation of vanadium during the Zn insertion/extraction with part of irreversibility. It is, as far as we know, the first time that the structural evolution and charge compensation mechanisms of Zn ions insertion into V_2O_5 in an electrochemical cell are elucidated through *in operando* synchrotron diffraction and *in operando* XAS.

Chapter 6 Determination of the preferred location of cation doping in the orthorhombic M-doped V_2O_5 (M=Mn, Ni, Fe) materials

6.1 Introduction

Cation doping is an effective method to modify the structure and electronic state of electrode materials. In the past decades, a lot of work has been focused on the doping of V_2O_5 nanostructure with various elements to overcome the capacity fading and improve the rate capability. The doping can increase electronic conductivity, stabilize the crystal structure of V_2O_5 during cycling and facilitate the charge transfer. Moreover, it can alter the morphology, leading to an enhanced electrochemical performance of V_2O_5 [24, 159]. However, an excess of dopant may block the pathway where the ions should insert and electrochemically inactive dopant could reduce the usage of active materials, thus affecting the capacity. Moreover, impurity or second phase might be induced with an excess of doping cations, which might, in turn, have a negative effect on the electrochemical performance of materials. Although the cation doping was proven to have positive impact on the electrochemical performance for LIBs has been proved, a fundamental study of the location of doped cation (substitutional or interstitial position) in V_2O_5 is rarely reported. Here, substitutional and interstitial doping mean that the doped element M replaces the V ions and resides between the V_2O_5 layers, respectively.

So far, it is unknown whether the preferred site depends on the synthesis route or is associated with the nature of doped cation or maybe both. As demonstrated in previous works, the dopant cations, for example, Zn^{2+} [316-317] and Cu^{2+} [316-317] in V_2O_5 aerogel/xerogel, Cr^{3+} [148] and Fe^{3+} [142] in crystalline V_2O_5, prefer to locate in the interlayer spacing/residing between the V_2O_5 layers. In above work, a pre-prepared V_2O_5 hydrogel ($V_2O_5 \cdot nH_2O$) was used as starting material to obtain the above doped material by mixing with stoichiometric amount of Zn or Cu powder or $Cr(NO_3)_3$ or $FeCl_3$ solution, without or with a following heat treatment. Consequently, it is not appropriate to study the preferred location associated to the nature of doped cation by starting with a formed layered structure material of $V_2O_5 \cdot nH_2O$. In order to properly study the preferred locations, a uniform solution should be prepared during the synthesis of M doped V_2O_5. In this purpose, M-doped V_2O_5 (M= Mn, Ni, and Fe; x=0, 0.1 and 0.2) materials are designed and synthesized through hydrothermal method. In this way, all the starting materials are dissolved into the aqueous solution and the V and M ions can uniformly distribute in the precursor material to obtain a homogenous target material after heat treating the precursor.

To gain a complete understanding of the cations doping in the V_2O_5 structure, several techniques are used such as chemical analysis, synchrotron diffraction, Pair distribution function (PDF), SEM, Raman, XPS, ^{51}V NMR, and XAS (XANES and EXAFS).

6.2 Experimental

Synthesis of M dope V_2O_5 materials: The doped V_2O_5 materials are designed as $M_xV_{2-x}O_5$ (M= Mn, Ni, and Fe; x=0, 0.1 and 0.2). $MnCl_2$, $NiCl_2$, and $Fe(NO_3)_3$ are used as starting materials to provide corresponding amount of Mn, Ni, and Fe, respectively. The V_2O_5-based materials were synthesized with the hydrothermal method as described in Chapter 3 (Experimental part **3.2**) except an additional stirring step applied. 1.0 ml of 2 M HCl, ammonium metavanadate (NH_4VO_3, 0.3 g for x=0) with a molar ratio of (M:V=x:2-x), and 0.5 g of surfactant P123 ($EO_{20}PO_{70}EO_{20}$, where EO and PO represent ethylene oxide and propylene oxide, respectively) were mixed into 30 ml of deionized water under ultrasonication for 10 mins and a consequent stirring for 1 h. After that, the mixed solution was transferred to 50 ml Teflon-lined autoclaves and maintained at 120 ^oC for 24 h with intermittent stirring in an oven. The resulting precipitates were filtered and washed with water and acetone several times, then dried under vacuum at 120 ^oC for 24 h. The products were annealed at 400 ^oC for 2 h in air with a heating rate of 10 ^oC/min.

Morphological, Structural and Surface Characterization: The morphology was studied with a Zeiss Supra 55 Scanning Electron Microscope (SEM) with primary energy of 15 keV. The structural characterization was performed using synchrotron radiation (λ = 0.4132 Å, 30 keV) at the Material Science and Powder Diffraction beamline (MSPD) at ALBA synchrotron (Barcelona, Spain)[266]. The diffraction pattern was collected in capillary by powder filled in 0.7 mm Ø boro-silicate capillary. The synchrotron diffraction data were analyzed by the Rietveld method using the Fullprof software package[287]. The crystallographic model was chosen from Shklover and Haibach[40]'s work for the Rietveld refinement of doped samples.

Pair distribution function (PDF) X-ray total scattering data, suitable for PDF analysis, were performed using synchrotron radiation (λ = 0.2072 Å, 60 keV) at beamline P02.1, PETRAIII, DESY, Hamburg. The powder material was filled in 0.7 mm Ø boro-silicate capillary for PDF measurements and an empty capillary of borosilicate type was tested for background corrections. A LaB_6 standard material (NIST SRM 660b) was measured at similar conditions to get the instrumental resolution. The measurements were carried out with a fast area detector from Perkin Elmer to collect 2D diffraction images and then the data were converted into one dimensional X-ray powder diffraction data with the FIT2D software[318]. The data were corrected for background scattering, Compton scattering, and detector effects. Data was Fourier transformed to Q_{max} = 23 $Å^{-1}$ to obtain the PDF G(r) within PDFgetX2[319]. Structure models were refined against the PDF data within PDFgui[320].

X-ray photoelectron spectroscopy (XPS) was performed using a Thermo Fisher K-Alpha$^+$ XPS spectrometer with a micro-focused, monochromatized Al K_α X-ray source for all samples, detailed description can be found in Chapter 3 (3.2 Experimental).

Raman measurements were carried out with a LabRam Evolution HR FROM Horiba equipped with Nd: YAG laser (633 nm, 100 mW) and a CCD detector (Horiba). To collect the Raman spectra of all samples, a 600 grating was used to split the measurement signal with a ×100 objective (NA 0.95) and the data collection was conducted for 30 seconds with laser source of 1 mW.

^{51}V magic-angle spinning (MAS) nuclear magnetic resonance (NMR) spectroscopy was performed with a Bruker Avance 200 MHz spectrometer at a magnetic field of 4.7 T, corresponding to a Larmor frequency of 52.6 MHz. Spinning was performed with 1.3 mm zirconia MAS rotors at 55 kHz. The spectra were acquired with a Hahn-echo pulse sequence, a $\pi/2$ pulse length of 1.5 μs, and a recycle delay of 5 s. The chemical shift of ^{51}V was referenced to $VOCl_3$.

Ex situ XAS measurements were performed at synchrotron beamlines P64 and P65 at PETRA III (DESY), Hamburg. XAS spectra of Vanadium were recorded in quick-XAS (6 min/spectrum) mode in fluorescence geometry using a PIPS (passivated implanted planar silicon) diode. The V, Mn, Ni, and Fe K-edge for doped V_2O_5 were measured and the energy was calibrated utilizing a corresponding foil V, Mn, Ni, and Fe as commonly applied in XAS experiments. V_2O_3, VO_2, and V_2O_5 MnO, Mn_2O_3, MnO_2, NiO, FeO, Fe_3O_4, and Fe_2O_3 were used as standard materials, respectively. All the data were collected at room temperature with a Si(111) double crystal monochromator and all the XAS spectra were processed using the DEMETER software package[289].

6.3 Results and discussion

6.3.1 Chemical analysis

The doped samples were analyzed by using the inductively coupled plasma optical emission spectroscopy (ICP-OES)[321] to check the content of doped element M in the $M_xV_{2-x}O_5$ materials. **Table 6.1** provides the desired and determined V/M molar ratio and estimated stoichiometry for M_x doped V_2O_5 (M= Mn, Ni, and Fe; x= 0.1 and 0.2) samples. The ICP result demonstrates the molar ratio of V/M is 208.7, 119.6, 164.3, 88.2, 18.3, and 8.3 for $Mn_{0.1}$, $Mn_{0.2}$, $Ni_{0.1}$, $Ni_{0.2}$, $Fe_{0.1}$, and $Fe_{0.2}$ doped samples. However, the atomic ratio of V/M for Mn and Ni is far away from the designed value (V/M ratio is 19 and 9 for x=0.1 and 0.2, respectively). This could be due to the loss during the hydrothermal synthesis, where only a small amount of Ni and Mn can dope inside the structure and most of it remains in the solution and is washed away. Meanwhile, the atomic ratio of Fe-doped samples is close to the theoretical molar ratio. Therefore, the chemical formula for doped samples are estimated as $Mn_{0.01}V_2O_5$, $Mn_{0.016}V_2O_5$, $Ni_{0.012}V_2O_5$, $Ni_{0.023}V_2O_5$, $Fe_{0.11}V_2O_5$ and $Fe_{0.24}V_2O_5$. In order to easy describe and discuss, M_x doped V_2O_5 (M= Mn, Ni, and Fe; x=0, 0.1 and 0.2) are used for each doped sample in the whole work.

Table 6.1 The desired and determined V/M molar ratio and estimated stoichiometry for M_x doped V_2O_5 (M= Mn, Ni, and Fe; x=0.1 and 0.2) samples

	V/M molar ratio desired	V/M molar ratio determined	Stoichiometry
Mn, x=0.1	19	208.7	$Mn_{0.01}V_2O_5$
Mn, x=0.2	9	119.6	$Mn_{0.016}V_2O_5$
Ni, x=0.1	19	164.3	$Ni_{0.012}V_2O_5$
Ni, x=0.2	9	88.2	$Ni_{0.023}V_2O_5$
Fe, x=0.1	19	18.3	$Fe_{0.11}V_2O_5$
Fe, x=0.2	9	8.3	$Fe_{0.24}V_2O_5$

6.3.2 Morphological and structural characterization

The crystal structure of the M_x doped V_2O_5 (M= Mn, Ni, and Fe; x=0, 0.1 and 0.2) was investigated by synchrotron diffraction as shown in **Figure 6.1**. The strong intensities of reflections reveal the high crystallinity of the obtained M_x doped V_2O_5 materials. For the pristine, Mn-doped and Ni-doped V_2O_5 (**Figure 6.1a-e**), all reflections could be indexed to the orthorhombic α-V_2O_5 with space group $Pmn2_1$, while some additional reflections are obtained for Fe-doped V_2O_5. The reflections were found to belong to $Fe_2V_4O_{13}$ phase with a space group of $P12_1/c1$. **Table 6.2** displays the atomic coordinates of the structural model ($M_xV_2O_5$)[40] for Rietveld refinement. M1 and M2 represent the substitution of V sites and the interstitial position between the layers for doped element M, respectively. The lattice parameters are listed in **Table 6.3** after Rietveld refinement. The pristine V_2O_5 has a = 11.5084 Å, b = 4.3739 Å, c = 3.5640 Å, which are in good agreement with previous work[40]. The lattice parameter c remains almost unaffected by the doping. The lattice parameter a shows a slight decrease for both Mn-doped samples while a shows a slight increase for Ni-doped samples compared with pristine one. The lattice parameter b for all Mn- and Ni-doped samples first slight decrease and then increase along with the content increase of doping cation, compared with that of pristine. For Fe-doped samples, the lattice parameter a and b show a larger changes with the continuous increase of a and decrease of b. The negative values of occupy of M1 are observed for all doped samples during the Rietveld refinement. Afterward, occupy of M1 was fixed to be 0. Rietveld refinement confirmed that occupy of M2 is positive for M-doped V_2O_5 and all of them have the same occupy of V. This might suggest that the interstitial position is the preferred location in all doped cases though the amount could not match well with the ICP result.

Table 6.2 Atomic coordinates of the structural model ($M_xV_2O_5$) for Rietveld refinement

	x	**y**	**z**
V1	0.14878	0.3913	0
M1	0.14878	0.3913	0
M2	0.5	0.077	-0.001
O1	0.1461	0.0324	-0.0009
O2	0.3193	0.5056	-0.0032
O3	0	0.5017	-0.0033

The SEM image demonstrates that the two Ni doped samples are composed of both nanowires and nanoparticles, while all the other samples are consisting of nanoparticles.

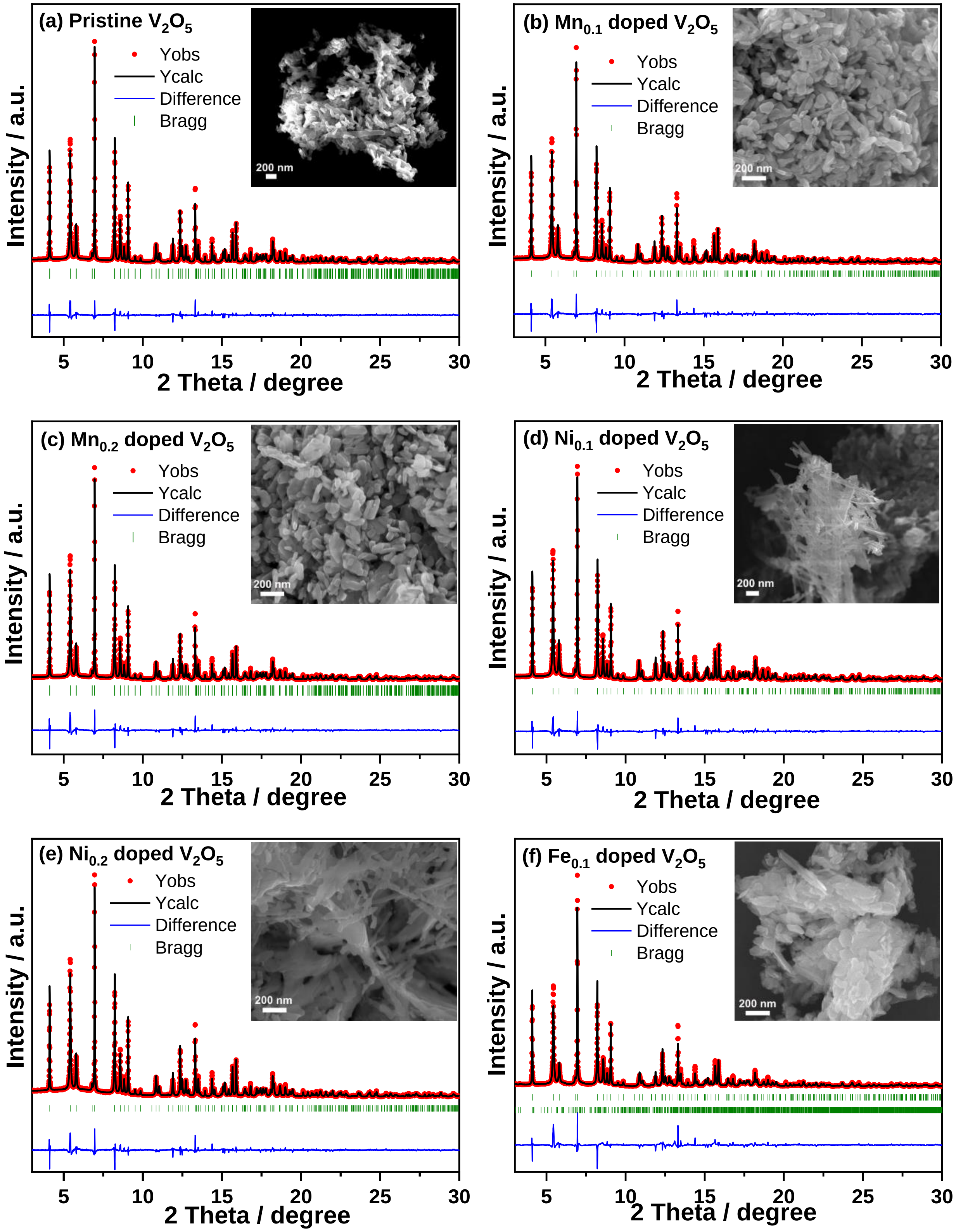

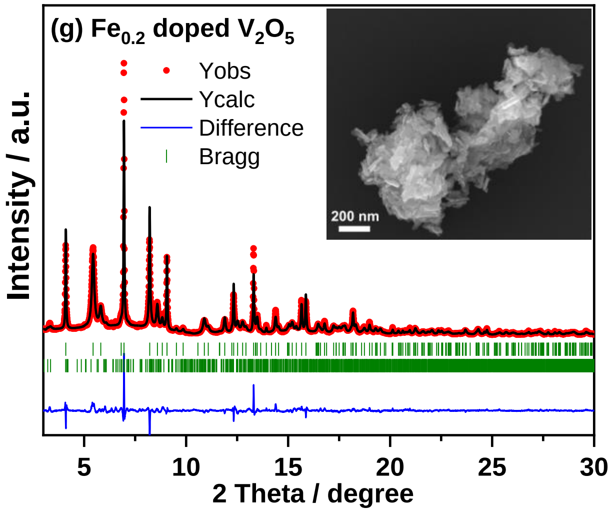

Figure 6.1 Rietveld refinement from synchrotron diffraction data of M_x doped V_2O_5 (M= Mn, Ni, and Fe; x=0, 0.1 and 0.2) (insets: SEM images)

Table 6.3 Lattice parameters and occupy of M for doped materials $M_xV_{2-x}O_5$ (M= Mn, Ni, and Fe; x=0, 0.1 and 0.2)

Sample	*a*	*b*	*c*	Occupancy of V	Occupancy of M1	Occupancy of M2
Pristine V_2O_5	11.5084(1)	4.3739(1)	3.5640(1)	0.957(4)	--	--
$Mn_{0.1}$ doped V_2O_5	11.5077(1)	4.3727(1)	3.5644(1)	0.949(4)	-	0.004(1)
$Mn_{0.2}$ doped V_2O_5	11.5074(1)	4.3743(1)	3.5642(1)	0.953(4)	-	0.004(1)
$Ni_{0.1}$ doped V_2O_5	11.5097(1)	4.3727(1)	3.5642(1)	0.950(4)	-	0.004(1)
$Ni_{0.2}$ doped V_2O_5	11.5098(1)	4.3738(1)	3.5638(1)	0.958(5)	-	0.004(1)
$Fe_{0.1}$ doped V_2O_5	11.5374(2)	4.3554(1)	3.5637(1)	0.947(7)	-	0.009(1)
$Fe_{0.2}$ doped V_2O_5	11.5393(2)	4.3531(1)	3.5649(1)	0.941(6)	-	0.003(1)

In order to further study the effect of cations doping on the local structure of V_2O_5, Raman spectra were collected for pristine and doped $M_xV_{2-x}O_5$ materials as shown in **Figure 6.2**. Compared with the pristine V_2O_5 (corresponding peaks are clearly described in Chapter 3, 3.3.3) the Raman spectra of all doped materials do not show a significant shift on the main peak of V_2O_5. Two additional peaks at 651 and 867 cm^{-1} can be observed and they increase along with the increase of doped Mn amount. Several additional peaks between 750 and 1200 cm^{-1} are also obtained for Fe doped samples, some of them might be attributed to the impurity $Fe_2V_4O_{13}$. Interestingly, no clear difference can be observed for two Ni-doped sample.

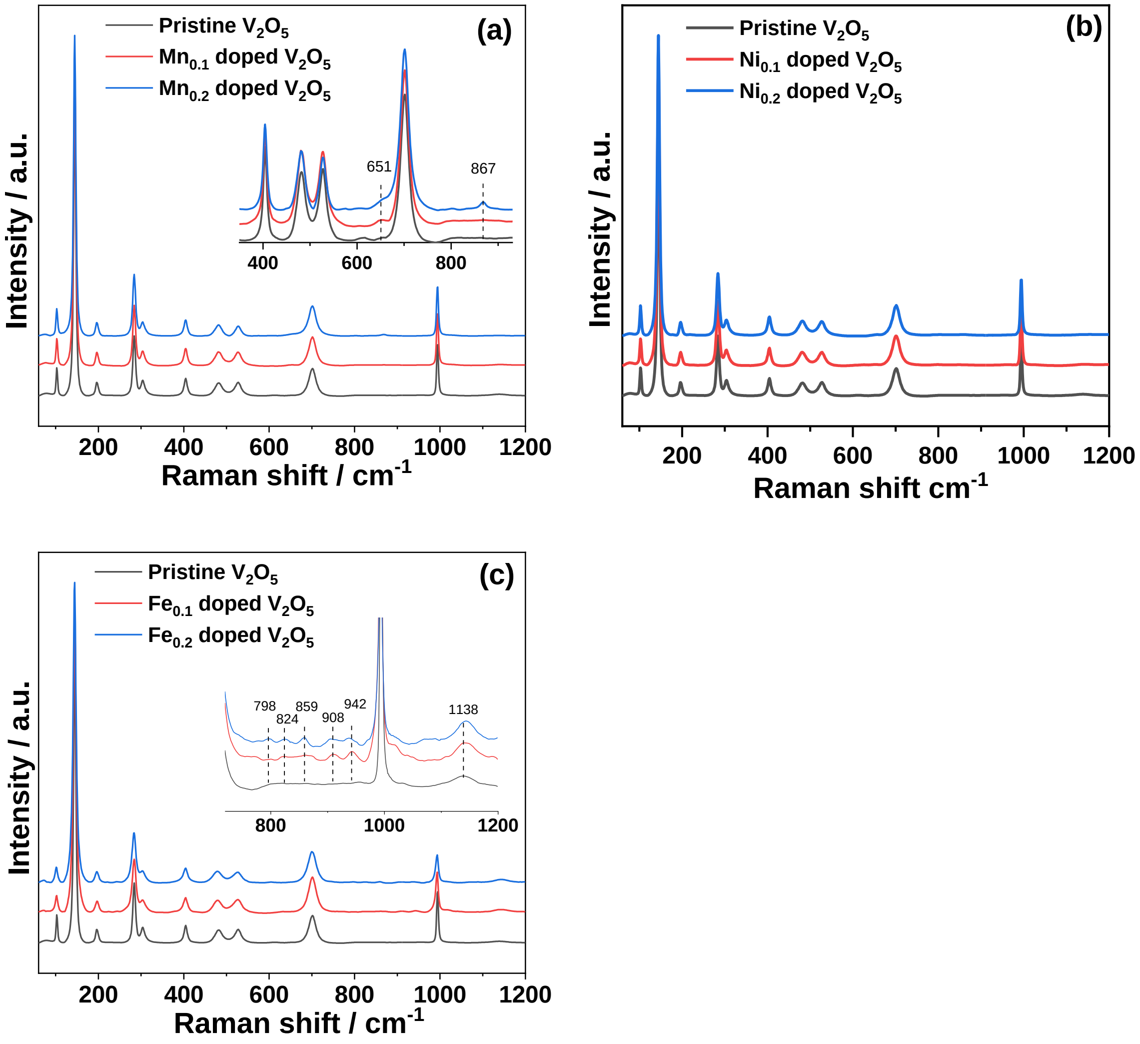

Figure 6.2 Raman spectra of all materials M_x doped V_2O_5 (M= Mn, Ni, and Fe; x=0, 0.1 and 0.2)

X-ray photoelectron spectroscopy (XPS) was used to look into the surface chemistry and surface elemental composition of pristine V_2O_5, and M_x doped V_2O_5 materials (M= Mn, Ni, and Fe; x=0, 0.1 and 0.2). According to **Figure 6.3a**, the C 1s spectrum of all samples can be fitted with 3 peaks at 285.0 eV, 286.7 eV, and 289.0 eV, which are ascribed to the C-C/C-H, C-O-C, and O-C=O group. O-C, O=C could be attributed to the residual surfactant symmetric triblock copolymer P123 which was present during synthesis. The V 2p spectrum of all samples (**Figure 6.3b**) can be fitted with two doublets: a main one with V $2p_{3/2}$ at 517.9 eV and a second one with weak intensity at 516.7 eV[304], which indicates that V exists mainly in the oxidation state +5 with a minor contribution of vanadium in +4 with very similar ratios of $V^{5+}/(V^{4+} + V^{5+})$ (93.4%, 93.8%, 93.1%, 93.6%, 94.9%, 94%, and 93.1% according to the order from top to bottom in **Figure 6.3b**).

The minor V(IV) could be assigned to the reduction of residual surfactant P123 during the annealing at 400 °C. It implies that the oxidation state of V is slightly influenced by the cations doping. It can be seen that the O 1s spectrum of pristine V_2O_5 can be fitted with 3 peaks at 533.1 eV, 531.8 eV, and 530.7 eV, which are corresponding to the O-C, O=C, and V-O groups[305-307], respectively. However, it is really difficult to get a clear analysis of the Mn 2p spectrum for Mn-doped samples due to its overlapping with V 2s. Meanwhile, due to the low intensity of Ni 2p and Fe 2p, it is also very difficult to get clear oxidation state of the metal M.

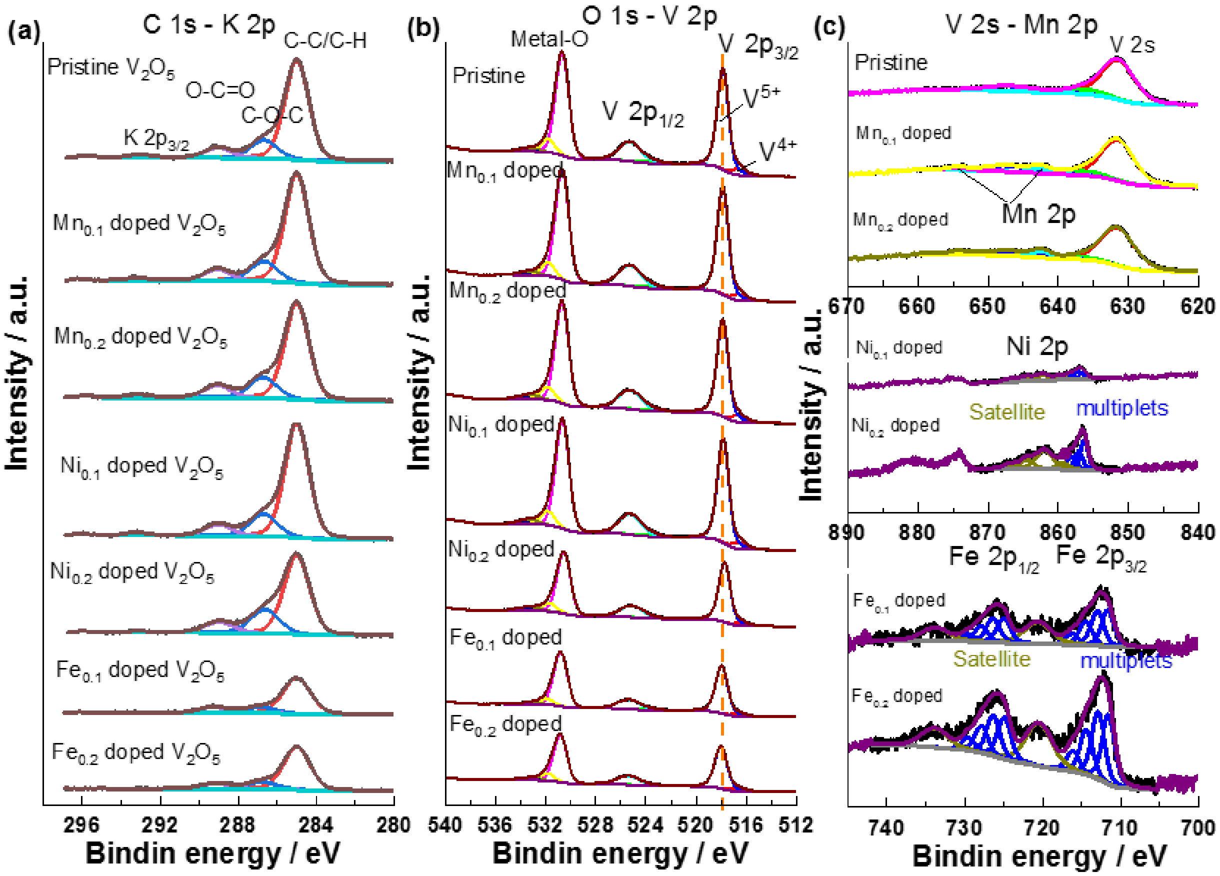

Figure 6.3 O 1s and C 1s (a), V 2p (b), and M 2p (c) X-ray photoelectron spectra of all materials M_x doped V_2O_5 (M= Mn, Ni, and Fe; x=0, 0.1 and 0.2)

Figure 6.4 displays the ^{51}V MAS NMR spectra of all the samples $M_xV_{2-x}O_5$. The spectrum of pristine V_2O_5 exhibits an isotropic shift of -609 ppm which is attributed to the characteristic of V_2O_5[322]. Furthermore, this spectrum shows a broad pattern of spinning sidebands reflecting the large nuclear quadrupolar moment of the ^{51}V nucleus[323] and the asymmetric environment around V in the crystal structure of V_2O_5. In this sample, V should be exclusively in the diamagnetic state V^{5+} ($3d^0$). For the samples doped with Mn, Ni, and Fe, the intensity of the spectra is significantly reduced. This is probably caused by partial reduction of V^{5+} resulting in paramagnetic V states, in good agreement with XPS results, where only V^{5+} cannot be detected by NMR. Furthermore, the Fe doped samples show a weak signal at -268 ppm. This reveals that the dopands cations for Mn, Ni, and Fe, have been incorporated into the crystal structure of V_2O_5.

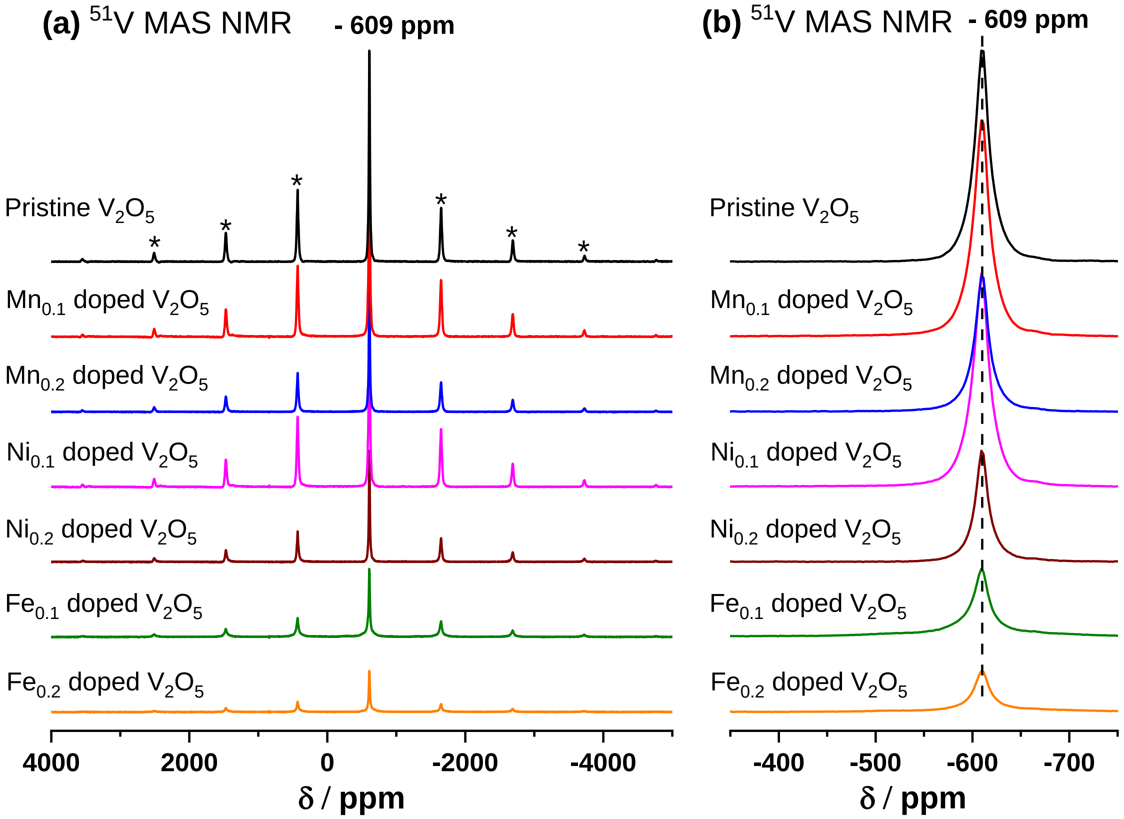

Figure 6.4 ^{51}V MAS NMR spectra of all the M_x doped V_2O_5 (M= Mn, Ni, and Fe; x=0, 0.1 and 0.2) samples

The atomic pair distribution functions (PDF) analysis is sensitive to local atomic ordering and is applied to investigate the influence of doping on the structure. As shown in **Figure 6.5**, the peaks of Ni doped V_2O_5 in the G(r) curves located at 1.55 Å, 2.23 Å, 4.94 Å, and 7.09 Å gradually increase with increasing concentration of the dopant cation. However, the G(r) curves of Mn and Fe doped V_2O_5 are similar to the pure V_2O_5. Therefore, the PDF analysis confirms the incorporation of Ni atom into V_2O_5.

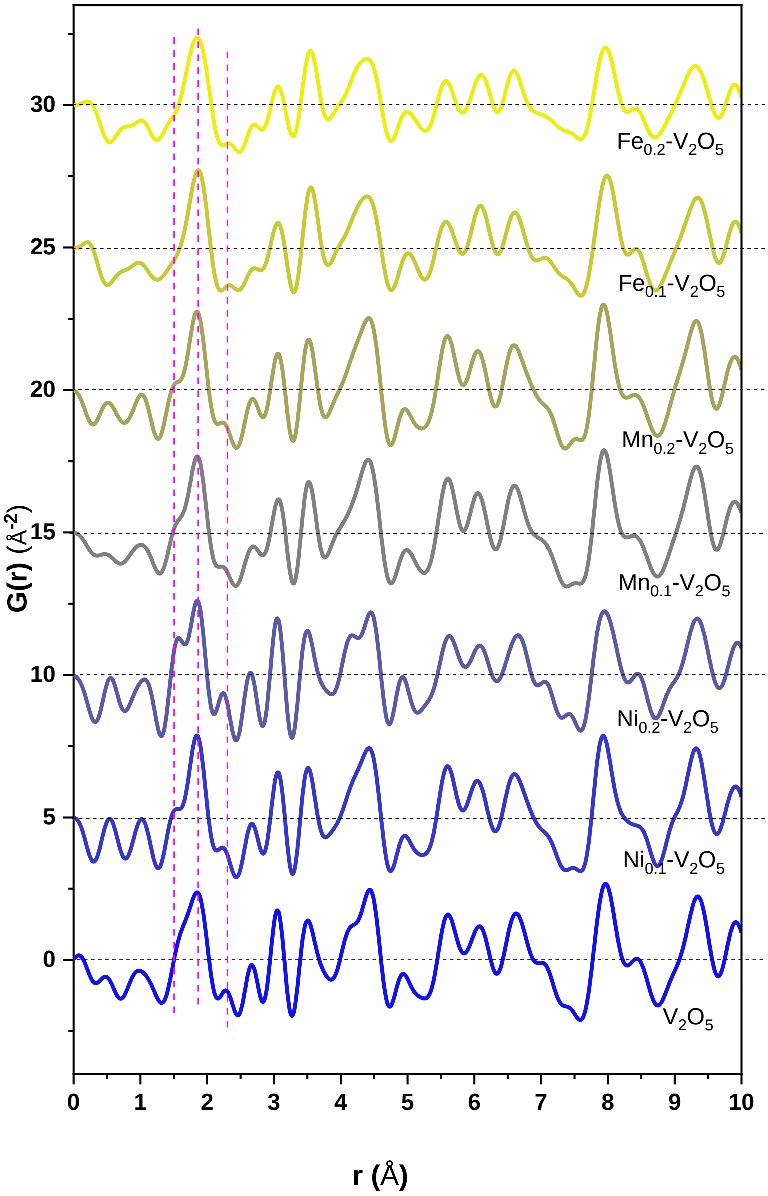

Figure 6.5 PDF data for all the M_x doped V_2O_5 (M= Mn, Ni, and Fe; x=0, 0.1 and 0.2) samples derived from X-ray total scattering data

In order to investigate the oxidation states and local electron environment of vanadium and dopants, *ex situ* XAS was collected on the $M_xV_{2-x}O_5$ samples. The edge position of V K-edge in the pure V_2O_5 material slightly lower than that of standard V_2O_5 reference (**Figure 6.6a**), indicating that the oxidation state of V in V_2O_5 is mainly +5 and in good agreement with XPS result. Moreover, an intense pre-edge peak for the V K-edge of pure V_2O_5 is observed for all samples. Interestingly, the edge position of V K-edge in the all doped V_2O_5 samples is slightly lower than that of pure V_2O_5 (**Figure 6.6a**), demonstrating the average oxidation state of V in doped samples is slightly lower and the part of reduction of V compared with pure V_2O_5 sample. The edge position of Ni K-edge for both Ni doped V_2O_5 materials overlaps with each other (**Figure 6.6b** and **c**). **Figure 6.6b** and **Figure 6.7b** suggest that the oxidation state of Ni is +2 in both Ni doped materials. **Figure 6.6c** shows that the oxidation state of Fe is +3 for both Fe doped samples. The two composition with Ni and Fe doping have slightly reduced oxidation state of Vanadium.

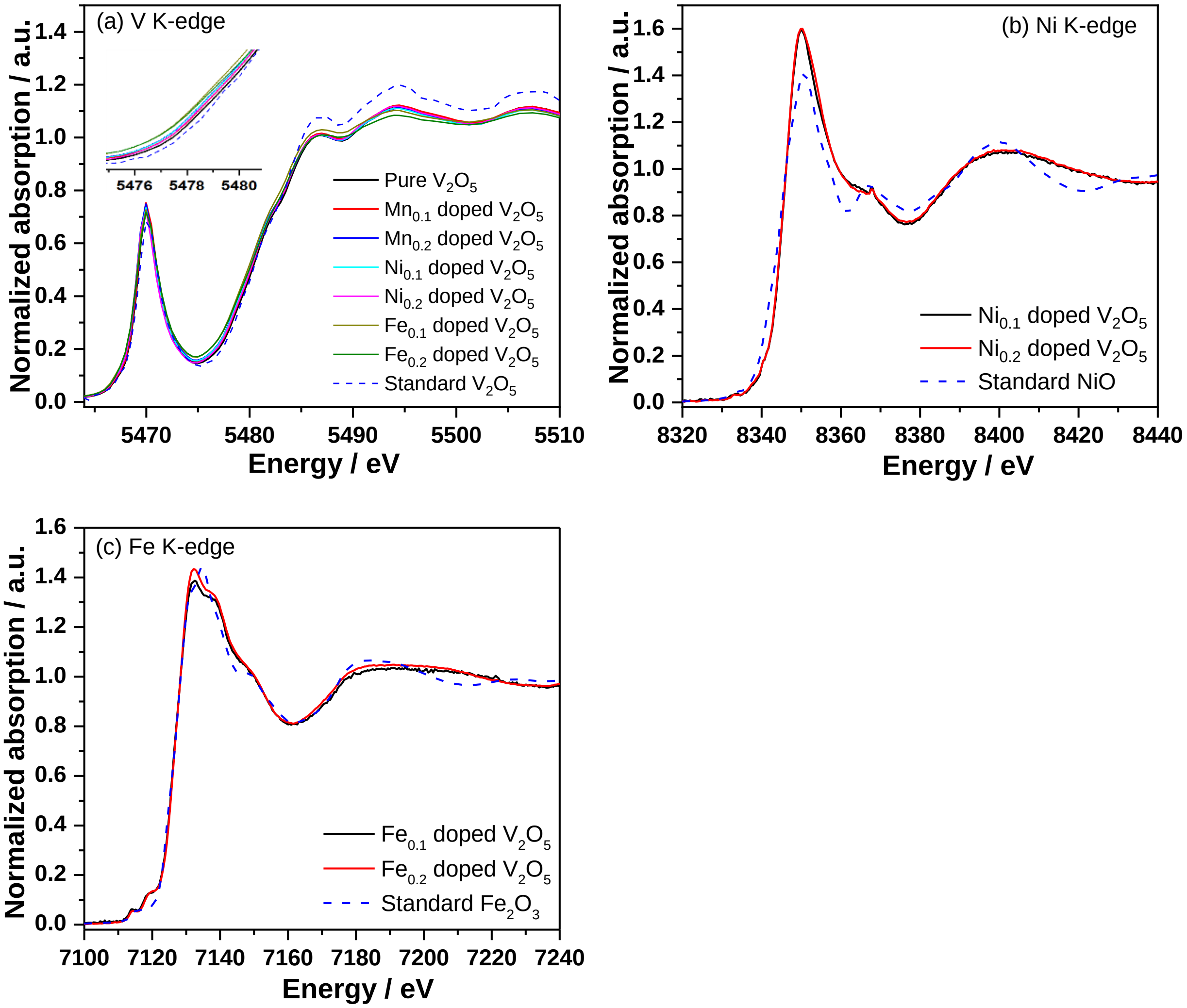

Figure 6.6 V, Ni, and Fe K-edge XANES spectra for M_x doped V_2O_5 (M= Mn, Ni, and Fe; x=0, 0.1 and 0.2)

Fourier transforms (FT) of vanadium K-edge EXAFS spectra for all doped compounds present 2 V-O distances in the first shell (see **Figure 6.7a**). Two V-O split peaks of the first coordination indicate a strongly distorted $[VO_6]$ octahedron in the orthorhombic V_2O_5[324]. The less amplitude we have, the more distorted octahedron is. The insertion of M ions can change the valence of the vanadium ions (that visible in $Fe_{0.1}$ doped and $Fe_{0.2}$ doped V_2O_5 samples) and lattice structural distortion, which is evident in the local symmetry of the VO_6 octahedra[324].

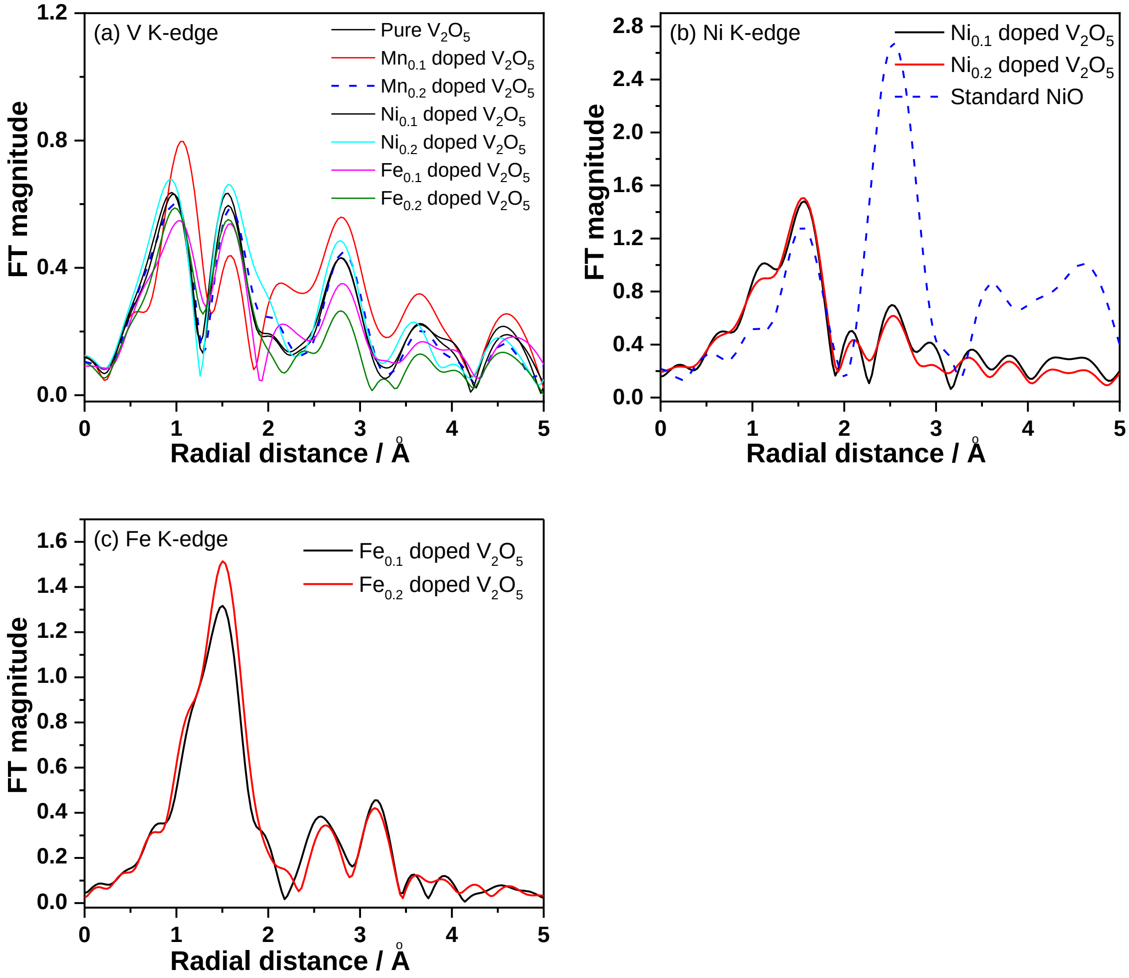

Figure 6.7 Fourier transforms (FT) of selected V K-edge (a), Ni K-edge (b), and Fe K-edge (c) EXAFS (k^3-weighted) for M_x doped V_2O_5 (M= Mn, Ni, and Fe; x=0, 0.1 and 0.2)

Fourier transforms (FT) of M (M= Ni and Fe) K-edge EXAFS spectra for all doped compounds show strong interaction in the Me-O shell, and low amplitude for the M-M shell[316]. As in the case of the Fe and Ni-doped samples, the first shell represents the main signal, and the Ni-Ni and Fe-Fe contribution is negligible. That is, the contribution of a two body M-M interaction is not significant in these samples, which can be due to the doping in the host V_2O_5 structure. However, a high quality of Mn K-edge spectrum for both Mn doped samples is not available probably because of the very low concentration in the doped samples.

6.4 Conclusion

All the M_x doped V_2O_5 materials (M= Mn, Ni, x=0, 0.1 and 0.2) were synthesized through a hydrothermal method. The chemical formula for the doped samples are estimated as $Mn_{0.01}V_2O_5$, $Mn_{0.016}V_2O_5$, $Ni_{0.012}V_2O_5$, $Ni_{0.023}V_2O_5$, $Fe_{0.11}V_2O_5$ and $Fe_{0.24}V_2O_5$ by ICP-OES. Synchrotron diffraction demonstrates that a single phase for pristine and both Mn- and Ni-doped V_2O_5 is obtained ($M_xV_{2-x}O_5$, M= Mn, Ni, x=0, 0.1 and 0.2). A phase impurity of $Fe_2V_4O_{13}$ is obtained for $Fe_xV_{2-x}O_5$ (x= 0.1 and 0.2) except for the orthorhombic Fe containing V_2O_5 phase. The preferred location of doped cation (substitutional or interstitial position) in V_2O_5 is studied with three different examples (Mn, Ni, and Fe). Rietveld refinement confirmed that the Mn and Ni would prefer locate the interstitial position for Mn-, Ni-, and Fe-doped. The cation doping in the materials is also confirmed by Raman, ^{51}V NMR and XAS.

Chapter 7 Other related work during my PhD study

In addtion to the study of V_2O_5 based materials for energy storage systems, other work has also been done during my PhD study, including the international cooperation work with Jilin University and TiO_2 in MBs and hybrid Li/Mg batteries, as well as Ca-doped LVP materials for LIBs.

7.1 NASICON-Type $Mg_{0.5}Ti_2(PO_4)_3$ Negative Electrode Material Exhibits Different Electrochemical Energy Storage Mechanisms in Na-Ion and Li-Ion Batteries

Carbon-coated $Mg_{0.5}Ti_2(PO_4)_3$ was prepared through sol-gel method. Rietveld refinement of X-ray diffraction data shows the pristine material has a main phase of $Mg_{0.5}Ti_2(PO_4)_3$ with space group R-3c and TiP_2O_7 impurity of 15 wt. %. In this work, the carbon-coated $Mg_{0.5}Ti_2(PO_4)_3$ was used as the anode material for LIBs and NIBs. It exhibits specific capacity of 268.6 mAh g^{-1} for in the potential range of 0.01-3.0 V and excellent rate capability of 94.4 mAh g^{-1} at 5000 mA g^{-1} and good cycle stability with capacity retention of 99.1 % after 300 cycles for NIBs. Upon cycling, the structure of $Mg_{0.5}Ti_2(PO_4)_3$ is maintained and the only Ti ions take part in the electrochemical redox reaction in NIBs confirmed by CV, EIS, *ex situ* XRD, XPS, TEM, and HRTEM. In comparison, $Mg_{0.5}Ti_2(PO_4)_3$ delivers capacity of 629 mAh g^{-1} for LIBs in the potential window of 0.01-3.0 V, which is mainly due to the interfacial Li^+ storage and formation/decomposition of the SEI film. It is likely that $Mg_{0.5}Ti_2(PO_4)_3$ in LIBs undergoes a different storage mechanism rather than only Li^+ intercalation reaction. It delivers a large reversible capacity of 578 mAh g^{-1} at 100 mA g^{-1} and 399 mAh g^{-1} at 1A g^{-1}, with capacity retention of only 45.2 % after 300 cycles. The decomposition reaction of pristine $Mg_{0.5}Ti_2(PO_4)_3$ into metallic Ti and Mg nanocrystallites after the first discharge was further clarified by *ex situ* XRD together with XPS, TEM, and HRTEM, which shows a fully different storage mechanism during the cycling.

Detailed information can be found: ACS Appl. Mater. Interfaces, 2017, 9 (5), pp 4709–4718
https://pubs.acs.org/doi/abs/10.1021/acsami.6b14196

7.2 Long cycle-life and high safety Na^+/Mg^{2+} hybrid-ion battery built by a TiS_2 derived titanium sulfide cathode

Recently, a new Daniell-type battery, Li^+/Mg^{2+} hybrid-ion battery (LMIB) has attracted particular attention for use in electrochemical energy storage. This kind of battery is composed of Mg anode, a Li^+ host material cathode, and a Li^+/Mg^{2+} hybrid electrolyte. During electrochemical reaction, only Mg deposition/dissolution takes place on the anode while the cathode side is dominated by Li^+ intercalation/de-intercalation. The use of Mg anode avoid the risk of internal short-circuit caused by dendrites. On the other hand, there are many options for the usage of cathode due to the larger family of Li^+ host materials. In this way, some intrinsic shortcomings of MBs such as large electrode polarization and poor cycle stability, as well as limited rate capability can be effectively overcome. Thanks to the abundance of Na and Mg in the earth crust, a Na^+/Mg^{2+} hybrid-ion battery (NMIB) could be a alternate for the application of large-scale energy storage. The first proof-of-concept NMIB has been reported by Walter et al. using FeS_2 cathode. But the sluggish conversion reaction of FeS_2 with Na^+ limits the rate capability of this NMIB cell.

In this work, a novel NMIB cell is designed using metallic Mg anode, commercial layered TiS_2 cathode, together with 1.0M $NaBH_4$+0.1M $Mg(BH_4)_2$/DGM hybrid electrolyte. The commercial TiS_2 powder has well-defined hexagonal structure with the space group *P*-3*m*1 with high crystallinity. Rietveld refinement shows the lattice parameters of the material are $a = b =$ 3.4087 Å and $c = 5.7000$ Å. This new NMIB cell significantly avoids the serious problems of dendrite formation of LIBs and NIBs and sluggish Mg^{2+} migration of MBs. This NMIB cell displays excellent electrochemical performance in terms of large reversible capacity of 200 mAh g^{-1} at 1C rate, excellent rate capability (75 mAh g^{-1} at 20C rate), ultra-long cycle life (90 % capacity retention after 3,000 cycles at 10C rate) and high safety properties. The cell exhibits a maximum discharge capacity of 105 mAh g^{-1} at 10C rate and still delivers capacity of 94 mAh g^{-1} after 3000 cycles with capacity retention of 90%. In particular, the NMIB cell demonstrates even better cycling stability with a narrow potential window of 0.4 - 1.8 V. It shows a discharge capacity of

58 mAh g^{-1} at 20C rate and keeps excellent capacity retention of ~100 % after 20000 cycles. In order to investigate the effects of electrolyte on the electrochemical properties in NMIB, controlled experiments were conducted with the $TiS_2\|x NaBH_4+y Mg(BH_4)_2/DGM\|Mg$ cell at the 200 mA g^{-1} The results demonstrate that TiS_2 in 1.0M $NaBH_4$+0.1M $Mg(BH_4)_2$/DGM electrolyte shows a best electrochemical performance of NMIB cell.

After the cell preparation, the TiS_2 electrode reacted with the Na^+/Mg^{2+} hybrid electrolyte, resulting in a new phase due to the organic species intercalation into the TiS_2 interlayers, which probably has a layered structure similar as that of TiS_2 and is highly efficient and reversible for Na^+/Mg^{2+} co-intercalation as proved through *in operando* synchrotron diffraction and *ex situ* XRD performed on TiS_2 samples aged in different solutions. However, determination of the crystal structure and chemical composition of the new phase is challenging to elucidate the reaction between TiS_2 and the hybrid electrolyte. Furthermore, the co-insertion of Na^+ and Mg^{2+} is confirmed through *ex situ* TEM, EDX, and ^{23}Na MAS NMR. DSC demonstrates the electrode at the fully charged cathode mixed with hybrid electrolyte does not exhibit any exothermic reaction in the temperature range of 50-450 °C. The endothermic peaks at 160 °C and 200 °C are coming from the Na^+/Mg^{2+} hybrid electrolyte, corresponding to decomposition of the electrolyte. Both the dendrite-free deposition and the high thermal stability of the cathode exhibit the excellent safety properties of the NMIB cell. Their outstanding performances suggest that this NMIB system could be used in large-scale applications such as grid-level stationary energy storage. Furthermore, the use of Mg anode in applicable NMIBs could reduce electrode processing procedures and provide a large volumetric energy density. This makes NMIBs competitive against traditional LIBs, due to their low cost, long cycle life, and high safety.

Detailed information can be found: J. Mater. Chem. A, 2017, 5, 600-608
https://pubs.rsc.org/en/content/articlelanding/2017/ta/c6ta08505a#!divAbstract

7.3 Electrochemical and structural investigations of different polymorphs of TiO_2 in magnesium and hybrid lithium/magnesium batteries

Synchrotron diffraction patterns demonstrate that commercial TiO_2-anatase and self-prepared TiO_2(B) via hydrothermal method are pure phase and can be indexed on the space group $I\,4_1/amd$ and $C\,2/m$, respectively and lattice parameters are a=3.7873(1) Å, c=9.5129(2) Å for TiO_2 anatase, and a=12.2572(22) Å, b=3.7772(3) Å, c=6.5271(4) Å, β=107.63º(2) for TiO_2(B). SEM displays that the TiO_2 anatase and TiO_2(B) are composed of nanoparticles (<25 nm) and nanowires, respectively.

Both commercial TiO_2 anatase and self-synthesized TiO_2(B) exhibit highly reversible capacity in the APC/LiCl hybrid electrolyte. TiO_2 anatase displays a discharge/charge capacity of 225 mAh g^{-1}/ 204 mAh g^{-1} with one flat plateau at ~0.9 V and following a slope-like region in APC/LiCl hybrid electrolyte, while the TiO_2(B) delivers high initial discharge capacity of 260 mAh g^{-1} with S-shaped discharge-charge curves in the same electrolyte. Both TiO_2 forms in pure APC electrolyte show significantly different behaviors from that in the hybrid electrolyte and only deliver discharge capacity of 53 mAh g^{-1} and 57 mAh g^{-1} with strong polarization. TiO_2 anatase in APC electrolyte with a C/70 rate exhibit a slight changes of lattice parameters identified by *in situ* synchrotron diffraction, suggesting the slow diffusion of Mg ion inside the TiO_2 anatase structure. Meanwhile TiO_2(B) shows a double layer capacitance behavior in pure APC electrolyte as proved *in situ* synchrotron diffraction thanks to the large diffusion barrier and the difficulty of Mg^{2+} desolvation. *In situ* synchrotron diffraction reveals that TiO_2 anatase undergoes as a solid solution reaction at the beginning of discharge and following a two-phase transition in the hybrid electrolyte (new phase $Li_{0.5}TiO_2$ with a space groups $Pmn2_1$) and TiO_2(B) goes through a solid solution mechanism. We believe, in our case, it is the coexistence of solid solution reaction and interfaces charge storage in the entire range of lithium uptake due to the nanostructured TiO_2(B) material and the a slow C rate of C/19 for in situ synchrotron diffraction. XPS analysis confirmed that surface charge storage phenomena happen along with the structural changes of the bulk electrodes. The high Mg/Ti ratio and Li/Ti ratio at discharged state indicate that both Li and Mg contribute to the charge storage mechanism, although the lithium insertion dominates reaction process in the bulk of cathode. Moreover, chemical insertion experiments were carried out through storing both TiO_2 into Di-*n*-butylmagnesium ($[CH_3(CH_2)_3]_2Mg$)/heptane solution to probe the possibility of Mg-insertion. *Ex situ* synchrotron diffraction and XPS reveal the possibility of the chemical magnesiation with n-Bu_2Mg for both TiO_2 forms but with quite low the efficiency.

Detailed information can be found: Electrochimica Acta, 2018, 277, 20-29
https://www.sciencedirect.com/science/article/pii/S001346861830985X

7.4 Sodium vanadium titanium phosphate electrode for symmetric sodium-ion batteries with high power and long lifespan

Because of the cost advantages and abundance, Na-ion batteries are very promising for use in large scale energy storage. However, it is very challenging to have suitable electrode materials with long cycle life and high- rate capability. In present work, NASICON-structured electrode, $Na_2VTi(PO_4)_3$ is designed optimizing different transition metal ions and prepared by a sol-gel method. Synchrotron diffraction reveals the crystal structure of $Na_2VTi(PO_4)_3$ is a rhombohedral structure in the space group R-3c and lattice parameters are a = 8.5992(1) Å and c = 21.8181(4) Å with a small amount of unknown impurity. Transmission electron microscopy reveals that the well-crystallized $Na_2VTi(PO_4)_3$ is composed of nanoparticles about 200 nm and dispersed within the amorphous carbon matrix. The amorphous carbon layer of 6 nm is coated on the surface of $Na_2VTi(PO_4)_3$ particles with carbon content of ~4.2 wt%.

The electrochemical performance of $Na_2VTi(PO_4)_3$@C was examined between 1.5 and 4.5 V at 0.1 C rate (1 C is defined as 125 mA g^{-1}). In the first charge, a flat plateau at ~3.4 V *vs.* Na^+/Na is observed, while three flat plateaus at 3.4, 2.1 and 1.6 V are obtained resulting from the stepwise reduction of $V^{4+} \rightarrow V^{3+}$, $Ti^{4+} \rightarrow Ti^{3+}$, and $V^{3+} \rightarrow V^{2+}$, respectively. It delivers an initial charge capacity of 59 mA h g^{-1} (extraction of 0.95 mol Na^+ per $Na_2VTi(PO_4)_3$) and discharge capacity of 147 mA h g^{-1} discharged to 1.5 V. It exhibits excellent rate capability with reversible capacities of 140, 120, 107, 100, 90, 77, and 50 mA h g^{-1}, respectively, from 0.1, 0.5, 1, 2, 5, 10 to 20 C rates. In addition, it shows a very high stability with the capacity retention of 77% after 500 cycles and the coulombic efficiency of nearly 100%.

A symmetric full cell is designed as $Na_2VTi(PO_4)_3$@C‖1M $NaClO_4$ in/EC:PC‖ $Na_2VTi(PO_4)_3$@C configuration and at 1 C (the battery is anode limited), it exhibits two pair of plateaus at 1.7 and 1.2 V with an initial discharge/charge capacity of 78/72 mA h g^{-1}, respectively. Surprisingly, it exhibits a good rate capability with a specific capacity of 49 mA h g^{-1} at 20 C and ultralong cycle life over 10,000 cycles with capacity retention of 74% at 10 C.

In addition, *in operando* synchrotron diffraction and XAS measurements are carried out to reveal the structural changes and charge compensation mechanism. *In operando* synchrotron diffraction reveals $Na_2VTi(PO_4)_3$ goes through a two-phase transition process during the 1st charge and undergoes two two-phase transition and solid solution processes during 1st discharge (all the phases have the same space group). The step oxidation and reduction of $V^{3+} \rightarrow V^{4+}$, $V^{4+} \rightarrow V^{3+}$, $Ti^{4+} \rightarrow Ti^{3+}$, and $V^{3+} \rightarrow V^{2+}$ are clearly demonstrated through *in operando* X-ray absorption spectroscopy. $Na_2VTi(PO_4)_3$ exhibits a highly reversible behavior in terms of charge transfer during the charge and discharge process. Our work highlights the prospect of NASICON-structured materials for the application in high-power and long-lived NIBs.

Detailed information can be found: Nature communications 2017, 8.
https://www.nature.com/articles/ncomms15888

7.5 Co_9S_8@carbon yolk-shell nanocages as a high-performance direct conversion anode material for sodium-ion batteries

Due to their appropriate working voltage and high practical capacities, Cobalt sulfides are considered as promising anode materials for sodium-ion batteries. But the severe volume change and structure transformation make their cycle stability and rate capability unsatisfactory. In this study, metal-organic framework derived Co_9S_8@carbon yolk-shell nanocages (Co_9S_8@CYSNs) was prepared by simply vulcanizing the ZIF-67 precursor and the following annealing process. SEM confirms that Co_9S_8@CYSNs is composed of uniform polyhedral particles with particle size of ~ 500 nm. TEM clearly shows Co_9S_8@CYSNs has a yolk-shell structure with a thick carbon shell of ~ 20 nm and a porous core of ~ 200 nm. High-resolution TEM (HRTEM) shows that the inner core of Co_9S_8@CYSNs is made of numerous 10 ~ 20 nm particles embedded in amorphous carbon matrix. N_2 adsorption-desorption isotherms exhibit of BET surface area of Co_9S_8@CYSNs is 112 m^2 g^{-1} with a pore size ~ 4 nm. In addition, TG analysis determines the carbon content of 27 wt.% in Co_9S_8@CYSNs. Co_9S_8@CYSNs delivers a first discharge capacity of 631.9 mAh g^{-1} and the charge capacity of 549.4 mAh g^{-1} in the potential range of 2.5 -0.2 V at 100 mA g^{-1}, resulting in an initial coulombic efficiency of 87.0 %. Co_9S_8@CYSNs exhibits good cycling stability with capacity retention of 91.8% after 50 cycles while bulk Co_9S_8 only has the capacity retention of 67.0% due to its poor kinetic properties and huge volume change. Co_9S_8@CYSNs material has high rate capability along with progressively increased current densities 0.2, 0.5, 1.0, 2.0, 4.0, 8.0, and 10.0 A g^{-1}, respectively, with reversible capacities of 547.0, 470.3, 426.9, 342.5, 244.8, 167.8, and 100.5 mA h g^{-1}. Impressively, it exhibits superior cycling performance with a capacity of 84.5% after 800 cycles at 10.0 A g^{-1} and the excellent performance of the Co_9S_8@CYSNs anode is a very attractive candidate for the application in NIBs.

A direct conversion mechanism and a "shrinking core" reaction model are identified and demonstrated, for the first time, by *in operando* XRD, *in operando* XAS and *ex situ* XPS, TEM techniques together with first-principles calculations. The poor conductivity of Na_2S makes the conversion reaction difficult to spread into the bulk and severe volume change results in bad cycling performance. In present work, Co_9S_8@CYSNs could effectively accelerate the conversion reaction, because of uniform nanoparticles and yolk-shell structure which can reduce the short diffusion distance and increase high conductivity. Moreover, the rigid carbon shell can buffer the volume variation of Co_9S_8 during cycling. As a result, it displays superior electrochemical performance with high reversible capacity, excellent high rate capability, and long cycling stability.

Detailed information can be found: Energy Storage Materials, 2018
https://www.sciencedirect.com/science/article/pii/S2405829718307712

7.6 Electrochemical and structural investigation of calcium-substituted monoclinic $Li_3V_2(PO_4)_3$ anode materials for Li-ion batteries

In this work, the effect of Li^+ substitution in $Li_3V_2(PO_4)_3$ with a large divalent ion (Ca^{2+}) toward lithium insertion is designed and studied. A series of materials, with formula $Li_{3-2x}Ca_xV_2(PO_4)_3/C$ (x=0, 0.5, 1, and 1.5), were synthesized by the carbon-thermal method and studied in the potential region of 3 - 0.01 V vs. Li^+/Li. The crystal structure, morphology, and components were studied by synchrotron diffraction, SEM, Raman, and TG. The carbon content in $Li_{3-2x}Ca_xV_2(PO_4)_3/C$ materials is estimated to be 8.06 wt%, 5.47 wt%, 6.03 wt%, and 3.89 wt%, respectively, via thermogravimetric analysis (TGA). The BET surface area of LVP/C is 54.3 m^2/g, while the BET surface area of $Ca_{1.5}VP/C$ is only 24.8 m^2/g. Two intermediate compositions $Li_2Ca_{0.5}V_2(PO_4)_3/C$ and $LiCaV_2(PO_4)_3/C$ have BET surface area 32.6 and 39.8 m^2/g, respectively. The pore-size distribution curve exhibits the pore size for all samples both in micro- and mesopore-range. These micro- and mesopores contribute about 90% of the total pore volume for sample LVP/C while the other three samples have the same value of about 60%. Moreover, Raman spectra confirmed the existence of amorphous carbon with disordered structures in the $Li_{3-2x}Ca_xV_2(PO_4)_3/C$. Synchrotron diffraction demonstrates that LVP/C has a monoclinic structure with the space group of $P2_1/n$ while $Ca_{1.5}V_2(PO_4)_3/C$ possesses a rhombohedral structure with a space group of $R\text{-}3c$. The intermediates compounds, $Li_2Ca_{0.5}V_2(PO_4)_3/C$ and $LiCaV_2(PO_4)_3/C$ are composed of two main phases, including monoclinic $Li_3V_2(PO_4)_3/C$ and rhombohedral $Ca_{1.5}V_2(PO_4)_3/C$.

Impressively, here is the first time that five reduction and oxidation peaks (instead of four) are observed in the cyclic voltammetry of LVP/C and $Li_2Ca_{0.5}V_2(PO_4)_3/C$. On the other hand, $LiCaV_2(PO_4)_3/C$ and $Ca_{1.5}V_2(PO_4)_3/C$ have no obvious oxidation and reduction peaks and their CV profile resemble a capacitive-like behavior. Indeed, by kinetic analysis, these two materials display a capacitive-like mechanism, which involves fast electron transfer at the surface of the electrode. $Li_{3-2x}Ca_xV_2(PO_4)_3/C$ compounds deliver specific capacities of 389.7, 273.6, 392.7, and 492.9 mAh g^{-1} at 1 C for x =0, 0.5, 1 and 1.5, respectively. These values are much higher than the theoretical ones. The excess of capacity might be attributed to the adsorption of ions on the amorphous carbon and on the micro-sized active materials synthesized by the carbon thermal reaction method. *In operando* synchrotron diffraction demonstrates that LVP/C undergoes two solid-solution and a short two-phase reaction during lithiation and delithiation processes, demonstrating a very good reversible structural change during the cycling and $Ca_{1.5}V_2(PO_4)_3$/C only goes through capacitive-like mechanism, showing a zero-strain material feature. *In operando* XAS confirms that the V is reduced during the first 3 Li ions insertion for both LVP/C and $Ca_{1.5}V_2(PO_4)_3$/C. The XAS results clearly show that V could not be reduced to a lower oxidation state after the insertion of 3 Li^+ ions, suggesting that at low potential the capacity is not due to the Li^+ insertion into the host materials, but has to be related to another mechanism like ion adsorption with a double layer formation, insertion into amorphous carbon with disordered structure and the SEI contribution. Among the different compositions, $Ca_{1.5}V_2(PO_4)_3$/C displays the highest discharge capacity until 40 C. At 200 C (an extreme high C-rate for battery materials), the cell polarization sensibly increases, but the electrodes are still able to deliver specific capacities higher than 50 mAh g^{-1}.

Detailed information can be found: First draft of Manuscript

Chapter 8 Conclusion and outlook

8.1 Conclusion

In the present thesis, I mainly focus on the study of the correlation between structural changes of V_2O_5 cathode materials and cations insertion/extraction with three examples Mg^{2+}, K^+, and Zn^{2+} for rechargeable Mg batteries, K-ion batteries, and aqueous Zn batteries. It is investigated through *in operando* synchrotron diffraction and *in operando* X-ray absorption spectroscopy together with *ex situ* Raman and X-ray photoelectron spectroscopy. Meanwhile, the electrochemical performance of V_2O_5 as cathode materials in three different systems were also investigated. Moreover, cation doping in the orthorhombic V_2O_5 material was studied to determine the location of doped cation in the substitutional or interstitial position with three different elements Ni, Mn, and Fe ($M_xV_2O_5$, M=Ni, Mn, and Fe).

All the orthorhombic V_2O_5 materials were successfully synthesized *via* a hydrothermal method. V_2O_5 nanowires in the cell configuration $V_2O_5 \vert Mg(ClO_4)_2/AN \vert Mg_xMo_6S_8$ deliver an initial discharge/charge capacity of 103 mAh g^{-1}/110 mAh g^{-1} and reach the highest discharge capacity of 130 mAh g^{-1} in the 6th cycle at a C/20 rate. The reversibility of the magnesium insertion/extraction in the V_2O_5 is clarified through *in operando* synchrotron diffraction and *in operando* XAS together with *ex situ* Raman and XPS. *In operando* synchrotron diffraction and *ex situ* Raman revealed the formation of a new phase of Mg-rich $Mg_xV_2O_5$ during Mg insertion and the recovery of V_2O_5 during Mg extraction. *In operando* XAS and *ex situ* XPS confirmed the reduction/oxidation of vanadium during the Mg insertion/extraction.

In comparison, V_2O_5 nanoparticles in 1 M KPF_6/PC electrolyte display an initial discharge/charge capacity up to 200 mAh g^{-1} (1.36 K^+ insertion)/217 mAh g^{-1} in the potential range of 1.5 - 4.0 V with a rate of C/12, which is much higher capacity and fast kinetics than that in MBs. However, V_2O_5 exhibits a rapid capacity loss and decreases to 54 mAh g^{-1} at the 31st cycle and then slowly increases up to 80 mAh g^{-1} after 200 cycles. *In operando* synchrotron diffraction revealed that V_2O_5 first undergoes a solid solution and then a coexistence of solid solution and two-phase reaction upon K ions insertion and a coexistence of solid solution and two-phase reaction is identified as well with irreversible process upon K ions extraction. *In operando* XAS confirmed the reduction/oxidation of vanadium during the K insertion/extraction with part of irreversibility, in consistence with the other results from synchrotron diffraction, Raman and TEM.

In the aqueous 1 M $ZnSO_4$ electrolyte, V_2O_5 nanowires deliver a much higher initial discharge/charge capacity of 277 and 432 mAh g^{-1} at a 50 mA g^{-1} (close to its theoretical capacity 294 mAh g^{-1}) compared with those in MBs and KIBs. However, it exhibits a much worse cycling stability with dramatic capacity decrease to 94 mAh g^{-1} for the 22nd cycle and very low discharge capacity of 21 mAh g^{-1} after 100 cycles. Moreover, the V_2O_5 nanowires undergo an activation process at high current density and delivers an initial discharge capacity of 278 mAh g^{-1} at 200 mA g^{-1}, demonstrating a much faster kinetics in aqueous ZBs than those in MBs and KIBs. The significant structure changes for both reduction and oxidation peaks were observed during CV scans of V_2O_5 electrode. *In operando* synchrotron diffraction revealed that V_2O_5 first undergoes a solid solution and two-phase reaction upon Zn ions insertion along with the formation of two byproducts $Zn_3(OH)_2V_2O_7{\cdot}2(H_2O)$ and $ZnSO_4Zn_3(OH)_6{\cdot}5H_2O$. This process is reversible upon Zn ions extraction with the decomposition of both byproducts, and the V_2O_5 electrode in the 2nd discharge process goes through the same two-phase reaction as that in the 1st discharge without the formation of by product $Zn_3(OH)_2V_2O_7{\cdot}2(H_2O)$. *In operando* XAS confirmed the reduction/oxidation of vanadium during the Zn insertion/extraction with part of irreversibility.

Finally, the preferred location of doped cation (substitutional or interstitial position) in V_2O_5 is investigated with three different elements (Mn, Ni, and Fe). Single phase for pristine and both Mn- and Ni-doped V_2O_5 is obtained ($M_xV_{2-x}O_5$, M= Mn, Ni, x=0, 0.1 and 0.2) through hydrothermal method. Rietveld refinement confirmed that the Mn, Ni, and Fe would prefer locate the interstitial position (between the layers) for M-doped V_2O_5 ($M_xV_{2-x}O_5$, M= Mn, Ni, x= 0.1 and 0.2). However, a phase impurity of $Fe_2V_4O_{13}$ is obtained for $Fe_xV_{2-x}O_5$ (x= 0.1 and 0.2) except the orthorhombic Fe contained V_2O_5 phase. Cation doping leads to slight change of the environments of V in the V_2O_5 structure confirmed by synchrotron diffraction, Pair distribution function (PDF), Raman, XPS, ^{51}V NMR, and XAS (XANES and EXAFS).

8.2 Outlook

The reaction mechanisms of V_2O_5 cathode materials in rechargeable Mg batteries, K-ion batteries, and aqueous Zn batteries have been investigated by *in operando* synchrotron diffraction and *in operando* X-ray absorption spectroscopy as well as by *ex situ* techniques. The electrochemical performances of the V_2O_5 cathode materials in each individual system can be, however, further improved. For example, V_2O_5 materials show very low reversible capacity in both MBs (~130 mAh g^{-1}) and KIBs (~120 mAh g^{-1}), which is much lower than its theoretical capacity of 294 mAh g^{-1}. In aqueous ZBs, V_2O_5 shows a very high initial capacity of ~277 mAh g^{-1}, which then rapidly decays. In this work, I focused on the mechanism occurring in the really first cycle, while the reason behind the strong capacity fading for these three systems are still not fully understood. To improve the performances of V_2O_5 in these three systems, the main points are addressed as below: (I) To study the dissolution of the electrode material in the electrolyte with different concentration after cycling, for example the chemical analysis of the electrolyte after cycling; (II) To investigate the structural stability of the electrode materials after cycling in different conditions with XRD, XPS, Raman, and TEM; (III) To look into the effect of the negative electrode material. For example, K metal as negative electrode could make the cell unstable because of its high reductive property; and (1) Heterogeneous structured materials such as carbon or rGO coating materials should be prepared to prevent the possible dissolution of the active materials and increase its conductivity as well, therefore improving the cycling stability and diffusion kinetics for fast rate capability; (2) Bifunctional cation doping and surface coating materials should be synthesized to enhance both electronic and ion conductivity and to stabilize the structure of the materials, therefore to improve their performances; (3) Other suitable electrolytes with wide electrochemical window and high performance should be developed by adjusting solvent, salt specimen, and concentration of the solution, even by adding additives; (4) The electrode preparation such as thickness and binder, and working voltage range should be optimized in order to obtain excellent electrochemical property. In addition, an appropriate anode should be explored to replace the current $Mg_xMo_6S_8$ and therefore to improve the capacity and energy density for MBs in the “chosen standard electrolyte”.

For the work of doped V_2O_5 samples, further analysis for PDF and EXAFS fitting is needed to clearly demonstrate the coordination of V and M.

Bibliography

1. Muldoon, J.; Bucur, C. B.; Gregory, T., Quest for Nonaqueous Multivalent Secondary Batteries: Magnesium and Beyond. *Chemical Reviews* **2014,** *114* (23), 11683–11720.
2. Larcher, D.; Tarascon, J. M., Towards greener and more sustainable batteries for electrical energy storage. *Nature Chemistry* **2015,** *7* (1), 19-29.
3. Jeong, G.; Kim, Y.-U.; Kim, H.; Kim, Y.-J.; Sohn, H.-J., Prospective materials and applications for Li secondary batteries. *Energy & Environmental Science* **2011,** *4* (6), 1986-2002.
4. Scrosati, B.; Hassoun, J.; Sun, Y.-K., Lithium-ion batteries. A look into the future. *Energy & Environmental Science* **2011,** *4* (9), 3287-3295.
5. Yang, Z.; Zhang, J.; Kintner-Meyer, M. C. W.; Lu, X.; Choi, D.; Lemmon, J. P.; Liu, J., Electrochemical Energy Storage for Green Grid. *Chemical Reviews* **2011,** *111* (5), 3577-3613.
6. Liu, C.; Li, F.; Ma, L.-P.; Cheng, H.-M., Advanced Materials for Energy Storage. *Advanced Materials* **2010,** *22* (8), E28-E62.
7. Dunn, B.; Kamath, H.; Tarascon, J.-M., Electrical Energy Storage for the Grid: A Battery of Choices. *Science* **2011,** *334* (6058), 928-935.
8. Liu, J., Addressing the Grand Challenges in Energy Storage. *Advanced Functional Materials* **2013,** *23* (8), 924-928.
9. Pan, H.; Hu, Y.-S.; Chen, L., Room-temperature stationary sodium-ion batteries for large-scale electric energy storage. *Energy & Environmental Science* **2013,** *6* (8), 2338-2360.
10. Tang, W.; Zhu, Y.; Hou, Y.; Liu, L.; Wu, Y.; Loh, K. P.; Zhang, H.; Zhu, K., Aqueous rechargeable lithium batteries as an energy storage system of superfast charging. *Energy & Environmental Science* **2013,** *6* (7), 2093-2104.
11. Wang, Y.; Yi, J.; Xia, Y., Recent Progress in Aqueous Lithium-Ion Batteries. *Advanced Energy Materials* **2012,** *2* (7), 830-840.
12. Goodenough, J. B.; Park, K.-S., The Li-Ion Rechargeable Battery: A Perspective. *Journal of the American Chemical Society* **2013,** *135* (4), 1167-1176.
13. Hwang, J.-Y.; Myung, S.-T.; Sun, Y.-K., Sodium-ion batteries: present and future. *Chemical Society Reviews* **2017,** *46* (12), 3529-3614.
14. Kubota, K.; Dahbi, M.; Hosaka, T.; Kumakura, S.; Komaba, S., Towards K-Ion and Na-Ion Batteries as "Beyond Li-Ion". *Chemical Record* **2018,** *18* (4), 459-479.
15. Whittingham, M. S., Lithium Batteries and Cathode Materials. *Chemical Reviews* **2004,** *104* (10), 4271-4302.
16. Saha, P.; Datta, M. K.; Velikokhatnyi, O. I.; Manivannan, A.; Alman, D.; Kumta, P. N., Rechargeable magnesium battery: Current status and key challenges for the future. *Progress in Materials Science* **2014,** *66*, 1-86.
17. Liu, J.; Xu, C.; Chen, Z.; Ni, S.; Shen, Z. X., Progress in Aqueous Rechargeable Batteries. *Green Energy & Environment* **2017**.
18. Li, M.; Lu, J.; Chen, Z.; Amine, K., 30 Years of Lithium-Ion Batteries. *Advanced Materials* **2018,** *30* (33), 1800561.
19. Kim, H.; Hong, J.; Park, K.-Y.; Kim, H.; Kim, S.-W.; Kang, K., Aqueous Rechargeable Li and Na Ion Batteries. *Chemical Reviews* **2014,** *114* (23), 11788-11827.
20. Yabuuchi, N.; Kubota, K.; Dahbi, M.; Komaba, S., Research Development on Sodium-Ion Batteries. *Chemical Reviews* **2014**, *114* (23), pp 11636–11682
21. Kim, H.; Kim, J. C.; Bianchini, M.; Seo, D.-H.; Rodriguez-Garcia, J.; Ceder, G., Recent Progress and Perspective in Electrode Materials for K-Ion Batteries. *Advanced Energy Materials* **2017**, 1702384.
22. Wang, N. N.; Chu, C. X.; Xu, X.; Du, Y.; Yang, J.; Bai, Z. C.; Dou, S. X., Comprehensive New Insights and Perspectives into Ti-Based Anodes for Next-Generation Alkaline Metal (Na^+, K^+) Ion Batteries. *Advanced Energy Materials* **2018,** *8* (27), 1801888.

23. Wang, Y.; Takahashi, K.; Lee, K. H.; Cao, G. Z., Nanostructured Vanadium Oxide Electrodes for Enhanced Lithium-Ion Intercalation. *Advanced Functional Materials* **2006,** *16* (9), 1133-1144.
24. Yao, J.; Li, Y.; Massé, R. C.; Uchaker, E.; Cao, G., Revitalized interest in vanadium pentoxide as cathode material for lithium-ion batteries and beyond. *Energy Storage Materials* **2018,** *11*, 205-259.
25. Wu, C.; Xie, Y., Promising vanadium oxide and hydroxide nanostructures: from energy storage to energy saving. *Energy & Environmental Science* **2010,** *3* (9), 1191.
26. Tang, P. E.; Sakamoto, J. S.; Baudrin, E.; Dunn, B., V_2O_5 aerogel as a versatile host for metal ions. *Journal of Non-Crystalline Solids* **2004,** *350*, 67-72.
27. Morcrette, M.; Chabre, Y.; Vaughan, G.; Amatucci, G.; Leriche, J. B.; Patoux, S.; Masquelier, C.; Tarascon, J. M., In situ X-ray diffraction techniques as a powerful tool to study battery electrode materials. *Electrochimica Acta* **2002,** *47* (19), 3137-3149.
28. Herklotz, M.; Weiss, J.; Ahrens, E.; Yavuz, M.; Mereacre, L.; Kiziltas-Yavuz, N.; Drager, C.; Ehrenberg, H.; Eckert, J.; Fauth, F.; Giebeler, L.; Knapp, M., A novel high-throughput setup for in situ powder diffraction on coin cell batteries. *Journal of Applied Crystallography* **2016,** *49* (1), 340-345.
29. Bak, S.-M.; Shadike, Z.; Lin, R.; Yu, X.; Yang, X.-Q., In situ/operando synchrotron-based X-ray techniques for lithium-ion battery research. *NPG Asia Materials* **2018,** *10* (7), 563-580.
30. Lin, F.; Liu, Y.; Yu, X.; Cheng, L.; Singer, A.; Shpyrko, O. G.; Xin, H. L.; Tamura, N.; Tian, C.; Weng, T.-C.; Yang, X.-Q.; Meng, Y. S.; Nordlund, D.; Yang, W.; Doeff, M. M., Synchrotron X-ray Analytical Techniques for Studying Materials Electrochemistry in Rechargeable Batteries. *Chemical Reviews* **2017,** *117* (21), 13123-13186.
31. Glazer, M. P. B.; Okasinski, J. S.; Almer, J. D.; Ren, Y., High-energy x-ray scattering studies of battery materials. *MRS Bulletin* **2016,** *41* (6), 460-465.
32. McBreen, J., The application of synchrotron techniques to the study of lithium-ion batteries. *Journal of Solid State Electrochemistry* **2009,** *13* (7), 1051-1061.
33. Gong, Z.; Yang, Y., The application of synchrotron X-ray techniques to the study of rechargeable batteries. *Journal of Energy Chemistry* **2018,** *6*, 1566-1583.
34. Etacheri, V.; Marom, R.; Elazari, R.; Salitra, G.; Aurbach, D., Challenges in the development of advanced Li-ion batteries: a review. *Energy & Environmental Science* **2011,** *4* (9), 3243-3262.
35. Ceder, G., Opportunities and challenges for first-principles materials design and applications to Li battery materials. *MRS Bulletin* **2010,** *35*, 693-701.
36. Foot, P. J. S., Principles and Prospects of High-Energy Magnesium-Ion Batteries. *Science Progress* **2015,** *98* (3), 264-275.
37. Zhang, Q.; Wang, Z.; Zhang, S.; Zhou, T.; Mao, J.; Guo, Z., Cathode Materials for Potassium-Ion Batteries: Current Status and Perspective. *Electrochemical Energy Reviews* **2018,** *1* (4), 625-658.
38. Hwang, J. Y.; Myung, S. T.; Sun, Y. K., Recent Progress in Rechargeable Potassium Batteries. *Advanced Functional Materials* **2018,** *28* (43), 1802938.
39. Liu, J.; Xu, C.; Chen, Z.; Ni, S.; Shen, Z. X., Progress in aqueous rechargeable batteries. *Green Energy & Environment* **2018,** *3* (1), 20-41.
40. Shklover, V.; Haibach, T.; Ried, F.; Nesper, R.; Novák, P., Crystal Structure of the Product of Mg^{2+} Insertion into V_2O_5 Single Crystals. *Journal of Solid State Chemistry* **1996,** *123* (2), 317-323.
41. Wang, Y.; Cao, G., Synthesis and Enhanced Intercalation Properties of Nanostructured Vanadium Oxides. *Chemistry of Materials* **2006,** *18* (12), 2787-2804.
42. Liu, X.; Zeng, J.; Yang, H.; Zhou, K.; Pan, D., V_2O_5-Based nanomaterials: synthesis and their applications. *RSC Advances* **2018,** *8* (8), 4014-4031.
43. Yue, Y.; Liang, H., Micro- and Nano-Structured Vanadium Pentoxide V_2O_5 for Electrodes of Lithium-Ion Batteries. *Advanced Energy Materials* **2017,** *7* (17), 1602545.
44. Wu, C.; Feng, F.; Xie, Y., Design of vanadium oxide structures with controllable electrical properties for energy applications. *Chemical Society Reviews* **2013,** *42* (12), 5157-5183.
45. Liu, M.; Su, B.; Tang, Y.; Jiang, X.; Yu, A., Recent Advances in Nanostructured Vanadium Oxides and Composites for Energy Conversion. *Advanced Energy Materials* **2017,** *7* (23), 1700885.

46. Pan, J.; Li, M.; Luo, Y. Y.; Wu, H.; Zhong, L.; Wang, Q.; Li, G. H., Microwave-assisted hydrothermal synthesis of V_2O_5 nanorods assemblies with an improved Li-ion batteries performance. *Materials Research Bulletin* **2016,** *74*, 90-95.
47. Song, H. Q.; Zhang, C. P.; Liu, Y. G.; Liu, C. F.; Nan, X. H.; Cao, G. Z., Facile synthesis of mesoporous V_2O_5 nanosheets with superior rate capability and excellent cycling stability for lithium ion batteries. *Journal of Power Sources* **2015,** *294*, 1-7.
48. Lv, W.; Huang, D.; Chen, Y.; Qiu, Q.; Luo, Z., Synthesis and characterization of Mo-W co-doped VO_2(R) nano-powders by the microwave-assisted hydrothermal method. *Ceramics International* **2014,** *40* (8), 12661-12668.
49. Kim, Y. B.; Shin, M. W., Synthesis of diverse structured vanadium pentoxides particles by the simplified hydrothermal method. *Materials Letters* **2014,** *132*, 247-250.
50. Bai, H.; Liu, Z.; Sun, D. D.; Chan, S. H., Hierarchical 3D micro-/nano-V_2O_5 (vanadium pentoxide) spheres as cathode materials for high-energy and high-power lithium ion-batteries. *Energy* **2014,** *76*, 607-613.
51. Tang, Y. X.; Rui, X. H.; Zhang, Y. Y.; Lim, T. M.; Dong, Z. L.; Hng, H. H.; Chen, X. D.; Yan, Q. Y.; Chen, Z., Vanadium pentoxide cathode materials for high-performance lithium-ion batteries enabled by a hierarchical nanoflower structure via an electrochemical process. *Journal of Materials Chemistry A* **2013,** *1* (1), 82-88.
52. Liu, Y. Y.; Uchaker, E.; Zhou, N.; Li, J. G.; Zhang, Q. F.; Cao, G. Z., Facile synthesis of nanostructured vanadium oxide as cathode materials for efficient Li-ion batteries. *Journal of Materials Chemistry* **2012,** *22* (46), 24439-24445.
53. Zhai, T.; Liu, H.; Li, H.; Fang, X.; Liao, M.; Li, L.; Zhou, H.; Koide, Y.; Bando, Y.; Golberg, D., Centimeter-Long V_2O_5 Nanowires: From Synthesis to Field-Emission, Electrochemical, Electrical Transport, and Photoconductive Properties. *Advanced Materials* **2010,** *22* (23), 2547-2552.
54. Liu, Y. D.; Guan, D. Y.; Gao, G. H.; Liang, X.; Sun, W.; Zhang, K.; Bi, W. C.; Wu, G. M., Enhanced electrochemical performance of electrospun V_2O_5 nanotubes as cathodes for lithium ion batteries. *Journal of Alloys and Compounds* **2017,** *726*, 922-929.
55. Lee, J. H.; Kim, J. M.; Kim, J. H.; Jang, Y. R.; Kim, J. A.; Yeon, S. H.; Lee, S. Y., Toward Ultrahigh-Capacity V_2O_5 Lithium-Ion Battery Cathodes via One-Pot Synthetic Route from Precursors to Electrode Sheets. *Advanced Materials Interfaces* **2016,** *3* (14), 1600173.
56. Wang, H.-g.; Ma, D.-l.; Huang, Y.; Zhang, X.-b., Electrospun V_2O_5 Nanostructures with Controllable Morphology as High-Performance Cathode Materials for Lithium-Ion Batteries. *Chemistry – A European Journal* **2012,** *18* (29), 8987-8993.
57. Liang, X.; Gao, G. H.; Du, Y. C.; Wang, J. C.; Sun, W.; Liu, Y. D.; Zhang, K.; Wu, G. M., Synthesis and characterization of various V_2O_5 microsphere structures and their electrochemical performance. *Journal of Alloys and Compounds* **2018,** *757*, 177-187.
58. Zhang, X. Y.; Wang, J. G.; Liu, H. Y.; Liu, H. Z.; Wei, B. Q., Facile Synthesis of V_2O_5 Hollow Spheres as Advanced Cathodes for High-Performance Lithium-Ion Batteries. *Materials* **2017,** *10* (1).
59. Li, H. K.; Wang, J. X.; Liu, X.; Sun, Q.; Djurisic, A. B.; Xie, M. H.; Mei, Y.; Tang, C. Y. Y.; Shih, K. M., Template-free synthesis of hierarchical hollow V_2O_5 microspheres with highly stable lithium storage capacity. *Rsc Advances* **2017,** *7* (5), 2480-2485.
60. Kim, K.; Lee, M. J., Template-assisted solvothermal assembly of size-controlled hierarchical V_2O_5 hollow microspheres with tunable nanoscale building blocks and their enhanced lithium storage properties. *Electrochimica Acta* **2017,** *258*, 942-950.
61. Wu, H. Y.; Qin, M. L.; Li, X. L.; Cao, Z. Q.; Jia, B. R.; Zhang, Z. L.; Zhang, D. Y.; Qu, X. H.; Volinsky, A. A., One step synthesis of vanadium pentoxide sheets as cathodes for lithium ion batteries. *Electrochimica Acta* **2016,** *206*, 301-306.
62. Ko, Y. N.; Kang, Y. C.; Park, S. B., A new strategy for synthesizing yolk-shell V_2O_5 powders with low melting temperature for high performance Li-ion batteries. *Nanoscale* **2013,** *5* (19), 8899-8903.

63. Ng, S.-H.; Patey, T. J.; Büchel, R.; Krumeich, F.; Wang, J.-Z.; Liu, H.-K.; Pratsinis, S. E.; Novák, P., Flame spray-pyrolyzed vanadium oxide nanoparticles for lithium battery cathodes. *Physical Chemistry Chemical Physics* **2009,** *11* (19), 3748-3755.
64. Wang, Y.; Cao, G. Z., Synthesis and enhanced intercalation properties of nanostructured vanadium oxides. *Chemistry of Materials* **2006,** *18* (12), 2787-2804.
65. Takahashi, K.; Limmer, S. J.; Wang, Y.; Cao, G., Synthesis and Electrochemical Properties of Single-Crystal V_2O_5 Nanorod Arrays by Template-Based Electrodeposition. *The Journal of Physical Chemistry B* **2004,** *108* (28), 9795-9800.
66. Reddy, C. V. S.; Jin, A. P.; Han, X.; Zhu, Q. Y.; Mai, L. Q.; Chen, W., Preparation and characterization of (PVP+V_2O_5) cathode for battery applications. *Electrochemistry Communications* **2006,** *8* (2), 279-283.
67. Pang, S.; Li, G.; Zhang, Z., Synthesis of Polyaniline-Vanadium Oxide Nanocomposite Nanosheets. *Macromolecular Rapid Communications* **2005,** *26* (15), 1262-1265.
68. Delmas, C.; Cognac-Auradou, H.; Cocciantelli, J. M.; Ménétrier, M.; Doumerc, J. P., The $Li_xV_2O_5$ system: An overview of the structure modifications induced by the lithium intercalation. *Solid State Ionics* **1994,** *69* (3), 257-264.
69. Cocciantelli, J. M.; Ménétrier, M.; Delmas, C.; Doumerc, J. P.; Pouchard, M.; Broussely, M.; Labat, J., On the $\delta \rightarrow \gamma$ irreversible transformation in Li//V_2O_5 secondary batteries. *Solid State Ionics* **1995,** *78* (1), 143-150.
70. Palanisamy, K.; Um, J. H.; Jeong, M.; Yoon, W.-S., Porous V_2O_5/RGO/CNT hierarchical architecture as a cathode material: Emphasis on the contribution of surface lithium storage. *Scientific reports* **2016,** *6*, 31275.
71. De Jesus, L. R.; Andrews, J. L.; Parija, A.; Banerjee, S., Defining Diffusion Pathways in Intercalation Cathode Materials: Some Lessons from V_2O_5 on Directing Cation Traffic. *ACS Energy Letters* **2018,** *3* (4), 915-931.
72. Liu, Q.; Liu, Y.; Sun, C.-J.; Li, Z.-f.; Ren, Y.; Lu, W.; Stach, E. A.; Xie, J., The Structural Evolution of V_2O_5 Nanocystals during Electrochemical Cycling Studied Using In operando Synchrotron Techniques. *Electrochimica Acta* **2014,** *136* (Supplement C), 318-322.
73. Muller-Bouvet, D.; Baddour-Hadjean, R.; Tanabe, M.; Huynh, L. T. N.; Le, M. L. P.; Pereira-Ramos, J. P., Electrochemically formed α'-NaV_2O_5: A new sodium intercalation compound. *Electrochimica Acta* **2015,** *176*, 586-593.
74. Ali, G.; Lee, J. H.; Oh, S. H.; Cho, B. W.; Nam, K.-W.; Chung, K. Y., Investigation of the Na Intercalation Mechanism into Nanosized V_2O_5/C Composite Cathode Material for Na-Ion Batteries. *ACS applied materials & interfaces* **2016,** *8* (9), 6032-6039.
75. Livage, J., Vanadium pentoxide gels. *Chemistry of Materials* **1991,** *3* (4), 578-593.
76. Aurbach, D., <Doron_Aurbach-Nonaqueous_Electrochemistry-CRC.pdf>. **1999**.
77. Chou, S.-L.; Wang, J.-Z.; Sun, J.-Z.; Wexler, D.; Forsyth, M.; Liu, H.-K.; MacFarlane, D. R.; Dou, S.-X., High Capacity, Safety, and Enhanced Cyclability of Lithium Metal Battery Using a V_2O_5 Nanomaterial Cathode and Room Temperature Ionic Liquid Electrolyte. *Chemistry of Materials* **2008,** *20* (22), 7044-7051.
78. Sasidharan, M.; Gunawardhana, N.; Yoshio, M.; Nakashima, K., V_2O_5 Hollow Nanospheres: A Lithium Intercalation Host with Good Rate Capability and Capacity Retention. *Journal of The Electrochemical Society* **2012,** *159* (5), A618-A621.
79. Velazquez, J. R.; Banerjee, S., Catalytic Growth of Single-Crystalline V_2O_5 Nanowire Arrays. *Small* **2009,** *5* (9), 1025-1029.
80. Semenenko, D. A.; Kozmenkova, A. Y.; Itkis, D. M.; Goodilin, E. A.; Kulova, T. L.; Skundin, A. M.; Tretyakov, Y. D., Growth of thin vanadia nanobelts with improved lithium storage capacity in hydrothermally aged vanadia gels. *CrystEngComm* **2012,** *14* (5), 1561-1567.
81. Shi, S.; Cao, M.; He, X.; Xie, H., Surfactant-Assisted Hydrothermal Growth of Single-Crystalline Ultrahigh-Aspect-Ratio Vanadium Oxide Nanobelts. *Crystal Growth & Design* **2007,** *7* (9), 1893-1897.

82. Nagaraju, G.; Chithaiahb, P.; Ashokac, S.; Mahadevaiah, N., Vanadium pentoxide nanobelts: One pot synthesis and its lithium storage behavior. *Crystal Research and Technology* **2012,** *47* (8), 868-875.
83. Qin, M.; Liang, Q.; Pan, A.; Liang, S.; Zhang, Q.; Tang, Y.; Tan, X., Template-free synthesis of vanadium oxides nanobelt arrays as high-rate cathode materials for lithium ion batteries. *Journal of Power Sources* **2014,** *268*, 700-705.
84. Niu, C. L.; Li, J. B.; Jin, H. B.; Shi, H. L.; Zhu, Y. Q.; Wang, W. Z.; Cao, M. S., Self-template processed hierarchical V_2O_5 nanobelts as cathode for high performance lithium ion battery. *Electrochimica Acta* **2015,** *182*, 621-628.
85. Mai, L.; Xu, L.; Han, C.; Xu, X.; Luo, Y.; Zhao, S.; Zhao, Y., Electrospun Ultralong Hierarchical Vanadium Oxide Nanowires with High Performance for Lithium Ion Batteries. *Nano Letters* **2010,** *10* (11), 4750-4755.
86. Cheah, Y. L.; Gupta, N.; Pramana, S. S.; Aravindan, V.; Wee, G.; Srinivasan, M., Morphology, structure and electrochemical properties of single phase electrospun vanadium pentoxide nanofibers for lithium ion batteries. *Journal of Power Sources* **2011,** *196* (15), 6465-6472.
87. Yin, H.; Yu, K.; Peng, H.; Zhang, Z.; Huang, R.; Travas-Sejdic, J.; Zhu, Z., Porous V_2O_5 micro/nano-tubes: Synthesis via a CVD route, single-tube-based humidity sensor and improved Li-ion storage properties. *Journal of Materials Chemistry* **2012,** *22* (11), 5013-5019.
88. Li, G.; Pang, S.; Jiang, L.; Guo, Z.; Zhang, Z., Environmentally Friendly Chemical Route to Vanadium Oxide Single-Crystalline Nanobelts as a Cathode Material for Lithium-Ion Batteries. *The Journal of Physical Chemistry B* **2006,** *110* (19), 9383-9386.
89. Rui, X.; Tang, Y.; Malyi, O. I.; Gusak, A.; Zhang, Y.; Niu, Z.; Tan, H. T.; Persson, C.; Chen, X.; Chen, Z.; Yan, Q., Ambient dissolution–recrystallization towards large-scale preparation of V_2O_5 nanobelts for high-energy battery applications. *Nano Energy* **2016,** *22*, 583-593.
90. Katsunori, T.; Steven, J. L.; Ying, W.; Guozhong, C., Growth and Electrochemical Properties of Single-Crystalline V_2O_5 Nanorod Arrays. *Japanese Journal of Applied Physics* **2005,** *44* (1S), 662.
91. Patrissi, C. J.; Martin, C. R., Sol-Gel-Based Template Synthesis and Li-Insertion Rate Performance of Nanostructured Vanadium Pentoxide. *Journal of The Electrochemical Society* **1999,** *146* (9), 3176-3180.
92. Li, Y.; Yao, J.; Uchaker, E.; Yang, J.; Huang, Y.; Zhang, M.; Cao, G., Leaf-Like V_2O_5 Nanosheets Fabricated by a Facile Green Approach as High Energy Cathode Material for Lithium-Ion Batteries. *Advanced Energy Materials* **2013,** *3* (9), 1171-1175.
93. Rui, X.; Lu, Z.; Yu, H.; Yang, D.; Hng, H. H.; Lim, T. M.; Yan, Q., Ultrathin V_2O_5 nanosheet cathodes: realizing ultrafast reversible lithium storage. *Nanoscale* **2013,** *5* (2), 556-560.
94. An, Q.; Wei, Q.; Mai, L.; Fei, J.; Xu, X.; Zhao, Y.; Yan, M.; Zhang, P.; Huang, S., Supercritically exfoliated ultrathin vanadium pentoxide nanosheets with high rate capability for lithium batteries. *Physical Chemistry Chemical Physics* **2013,** *15* (39), 16828-16833.
95. Liang, S.; Hu, Y.; Nie, Z.; Huang, H.; Chen, T.; Pan, A.; Cao, G., Template-free synthesis of ultra-large V_2O_5 nanosheets with exceptional small thickness for high-performance lithium-ion batteries. *Nano Energy* **2015,** *13*, 58-66.
96. Song, H.; Zhang, C.; Liu, Y.; Liu, C.; Nan, X.; Cao, G., Facile synthesis of mesoporous V_2O_5 nanosheets with superior rate capability and excellent cycling stability for lithium ion batteries. *Journal of Power Sources* **2015,** *294*, 1-7.
97. Wang, S.; Li, S.; Sun, Y.; Feng, X.; Chen, C., Three-dimensional porous V_2O_5 cathode with ultra high rate capability. *Energy & Environmental Science* **2011,** *4* (8), 2854-2857.
98. Wang, J.; Tang, H.; Zhang, L.; Ren, H.; Yu, R.; Jin, Q.; Qi, J.; Mao, D.; Yang, M.; Wang, Y.; Liu, P.; Zhang, Y.; Wen, Y.; Gu, L.; Ma, G.; Su, Z.; Tang, Z.; Zhao, H.; Wang, D., Multi-shelled metal oxides prepared via an anion-adsorption mechanism for lithium-ion batteries. *Nature Energy* **2016,** *1*, 16050.

99. Shao, J.; Li, X.; Wan, Z.; Zhang, L.; Ding, Y.; Zhang, L.; Qu, Q.; Zheng, H., Low-Cost Synthesis of Hierarchical V_2O_5 Microspheres as High-Performance Cathode for Lithium-Ion Batteries. *ACS applied materials & interfaces* **2013,** *5* (16), 7671-7675.
100. Wang, S.; Lu, Z.; Wang, D.; Li, C.; Chen, C.; Yin, Y., Porous monodisperse V_2O_5 microspheres as cathode materials for lithium-ion batteries. *Journal of Materials Chemistry* **2011,** *21* (17), 6365-6369.
101. Pang, H.; Cheng, P.; Yang, H.; Lu, J.; Guo, C. X.; Ning, G.; Li, C. M., Template-free bottom-up synthesis of yolk–shell vanadium oxide as high performance cathode for lithium ion batteries. *Chemical communications* **2013,** *49* (15), 1536-1538.
102. Liu, J.; Zhou, Y.; Wang, J.; Pan, Y.; Xue, D., Template-free solvothermal synthesis of yolk-shell V_2O_5 microspheres as cathode materials for Li-ion batteries. *Chemical communications* **2011,** *47* (37), 10380-10382.
103. Pan, A. Q.; Wu, H. B.; Zhang, L.; Lou, X. W., Uniform V_2O_5 nanosheet-assembled hollow microflowers with excellent lithium storage properties. *Energy & Environmental Science* **2013,** *6* (5), 1476-1479.
104. Zhang, X. F.; Wu, M. Z.; Gao, S.; Xu, Y. M.; Cheng, X. L.; Zhao, H.; Huo, L. H., Facile synthesis of uniform flower-like V_2O_5 hierarchical architecture for high-performance Li-ion battery. *Materials Research Bulletin* **2014,** *60*, 659-664.
105. Zheng, Y.-Z.; Ding, H.; Uchaker, E.; Tao, X.; Chen, J.-F.; Zhang, Q.; Cao, G., Nickel-mediated polyol synthesis of hierarchical V_2O_5 hollow microspheres with enhanced lithium storage properties. *Journal of Materials Chemistry A* **2015,** *3* (5), 1979-1985.
106. Pan, A.; Zhu, T.; Wu, H. B.; Lou, X., Template-Free Synthesis of Hierarchical Vanadium-Glycolate Hollow Microspheres and Their Conversion to V_2O_5 with Improved Lithium Storage Capability. *Chemistry-a European Journal* **2013,** *19* (2), 493-499.
107. Cao, A. M.; Hu, J. S.; Liang, H. P.; Wan, L. J., Self-assembled vanadium pentoxide V_2O_5 hollow microspheres from nanorods and their application in lithium-ion batteries. *Angewandte Chemie-International Edition* **2005,** *44* (28), 4391-4395.
108. Mai, L.; An, Q.; Wei, Q.; Fei, J.; Zhang, P.; Xu, X.; Zhao, Y.; Yan, M.; Wen, W.; Xu, L., Nanoflakes-Assembled Three-Dimensional Hollow-Porous V_2O_5 as Lithium Storage Cathodes with High-Rate Capacity. *Small* **2014,** *10* (15), 3032-3037.
109. Uchaker, E.; Zhou, N.; Li, Y.; Cao, G., Polyol-Mediated Solvothermal Synthesis and Electrochemical Performance of Nanostructured V_2O_5 Hollow Microspheres. *The Journal of Physical Chemistry C* **2013,** *117* (4), 1621-1626.
110. Aricò, A. S.; Bruce, P.; Scrosati, B.; Tarascon, J.-M.; van Schalkwijk, W., Nanostructured materials for advanced energy conversion and storage devices. *Nature materials* **2005,** *4*, 366.
111. Jiang, C.; Hosono, E.; Zhou, H., Nanomaterials for lithium ion batteries. *Nano Today* **2006,** *1* (4), 28-33.
112. Ren, Y.; Armstrong, A. R.; Jiao, F.; Bruce, P. G., Influence of Size on the Rate of Mesoporous Electrodes for Lithium Batteries. *Journal of the American Chemical Society* **2010,** *132* (3), 996-1004.
113. Liu, R.; Duay, J.; Lee, S. B., Heterogeneous nanostructured electrode materials for electrochemical energy storage. *Chemical communications* **2011,** *47* (5), 1384-1404.
114. Chen, Z.; Qin, Y.; Amine, K.; Sun, Y. K., Role of surface coating on cathode materials for lithium-ion batteries. *Journal of Materials Chemistry* **2010,** *20* (36), 7606.
115. Koltypin, M.; Pol, V.; Gedanken, A.; Aurbach, D., The Study of Carbon-Coated V_2O_5 Nanoparticles as a Potential Cathodic Material for Li Rechargeable Batteries. *Journal of The Electrochemical Society* **2007,** *154* (7), A605-A613.
116. Zhang, X.-F.; Wang, K.-X.; Wei, X.; Chen, J.-S., Carbon-Coated V_2O_5 Nanocrystals as High Performance Cathode Material for Lithium Ion Batteries. *Chemistry of Materials* **2011,** *23* (24), 5290-5292.

117. Zou, R.; Liu, Q.; He, G.; Yuen, M. F.; Xu, K.; Hu, J.; Parkin, I. P.; Lee, C.-S.; Zhang, W., Nanoparticles Encapsulated in Porous Carbon Matrix Coated on Carbon Fibers: An Ultrastable Cathode for Li-Ion Batteries. *Advanced Energy Materials* **2017,** *7* (2), 1601363.

118. Yan, B.; Li, X.; Bai, Z.; Zhao, Y.; Dong, L.; Song, X.; Li, D.; Langford, C.; Sun, X., Crumpled reduced graphene oxide conformally encapsulated hollow V_2O_5 nano/microsphere achieving brilliant lithium storage performance. *Nano Energy* **2016,** *24*, 32-44.

119. Gittleson, F. S.; Hwang, J.; Sekol, R. C.; Taylor, A. D., Polymer coating of vanadium oxide nanowires to improve cathodic capacity in lithium batteries. *Journal of Materials Chemistry A* **2013,** *1* (27), 7979-7984.

120. Sun, X.; Li, Q.; Mao, Y. B., Understanding the Influence of Polypyrrole Coating over V_2O_5 Nanofibers on Electrochemical Properties. *Electrochimica Acta* **2015,** *174*, 563-573.

121. Li, L.; Peng, S.; Chen, H.-Y.; Han, X.; Cheng, F.; Srinivasan, M.; Adams, S.; Ramakrishna, S.; Chen, J., Polypyrrole-coated hierarchical porous composites nanoarchitectures for advanced solid-state flexible hybrid devices. *Nano Energy* **2016,** *19*, 307-317.

122. Xie, M.; Sun, X.; Sun, H.; Porcelli, T.; George, S. M.; Zhou, Y.; Lian, J., Stabilizing an amorphous V_2O_5/carbon nanotube paper electrode with conformal TiO_2 coating by atomic layer deposition for lithium ion batteries. *Journal of Materials Chemistry A* **2016,** *4* (2), 537-544.

123. Xu, H.; Chen, J.; Zhang, H.; Zhang, Y.; Li, W.; Wang, Y., Fabricating SiO_2-coated V_2O_5 nanoflake arrays for high-performance lithium-ion batteries with enhanced cycling capability. *Journal of Materials Chemistry A* **2016,** *4* (11), 4098-4106.

124. Cheng, J.; Wang, B.; Xin, H. L.; Yang, G.; Cai, H.; Nie, F.; Huang, H., Self-assembled V_2O_5 nanosheets/reduced graphene oxide hierarchical nanocomposite as a high-performance cathode material for lithium ion batteries. *Journal of Materials Chemistry A* **2013,** *1* (36), 10814-10820.

125. Han, C.; Yan, M.; Mai, L.; Tian, X.; Xu, L.; Xu, X.; An, Q.; Zhao, Y.; Ma, X.; Xie, J., V_2O_5 quantum dots/graphene hybrid nanocomposite with stable cyclability for advanced lithium batteries. *Nano Energy* **2013,** *2* (5), 916-922.

126. Rui, X.; Zhu, J.; Sim, D.; Xu, C.; Zeng, Y.; Hng, H. H.; Lim, T. M.; Yan, Q., Reduced graphene oxide supported highly porous V_2O_5 spheres as a high-power cathode material for lithium ion batteries. *Nanoscale* **2011,** *3* (11), 4752-4758.

127. Choi, S. H.; Kang, Y. C., Uniform Decoration of Vanadium Oxide Nanocrystals on Reduced Graphene-Oxide Balls by an Aerosol Process for Lithium-Ion Battery Cathode Material. *Chemistry – A European Journal* **2014,** *20* (21), 6294-6299.

128. Cheng, J.; Gu, G.; Guan, Q.; Razal, J. M.; Wang, Z.; Li, X.; Wang, B., Synthesis of a porous sheet-like V_2O_5–CNT nanocomposite using an ice-templating 'bricks-and-mortar' assembly approach as a high-capacity, long cyclelife cathode material for lithium-ion batteries. *Journal of Materials Chemistry A* **2016,** *4* (7), 2729-2737.

129. Liu, Y. D.; Gao, G. H.; Liang, X.; Wu, G. M., Nanofibers of V_2O_5/C@MWCNTs as the cathode material for lithium-ion batteries. *Journal of Solid State Electrochemistry* **2018,** *22* (8), 2385-2393.

130. Zhao, H.; Pan, L.; Xing, S.; Luo, J.; Xu, J., Vanadium oxides–reduced graphene oxide composite for lithium-ion batteries and supercapacitors with improved electrochemical performance. *Journal of Power Sources* **2013,** *222*, 21-31.

131. Cao, Z.; Wei, B., V_2O_5/single-walled carbon nanotube hybrid mesoporous films as cathodes with high-rate capacities for rechargeable lithium ion batteries. *Nano Energy* **2013,** *2* (4), 481-490.

132. Jia, X.; Zhang, L.; Zhang, R.; Lu, Y.; Wei, F., Carbon nanotube-penetrated mesoporous V_2O_5 microspheres as high-performance cathode materials for lithium-ion batteries. *RSC Advances* **2014,** *4* (40), 21018-21022.

133. Zhou, X.; Wu, G.; Wu, J.; Yang, H.; Wang, J.; Gao, G.; Cai, R.; Yan, Q., Multiwalled carbon nanotubes–V_2O_5 integrated composite with nanosized architecture as a cathode material for high performance lithium ion batteries. *Journal of Materials Chemistry A* **2013,** *1* (48), 15459-15468.

134. Li, G.; Zhang, C.; Peng, H.; Chen, K., One-Dimensional V_2O_5@Polyaniline Core/Shell Nanobelts Synthesized by an In situ Polymerization Method. *Macromolecular Rapid Communications* **2009,** *30* (21), 1841-1845.

135. Zhao, H.; Yuan, A.; Liu, B.; Xing, S.; Wu, X.; Xu, J., High cyclic performance of V_2O_5@PPy composite as cathode of recharged lithium batteries. *Journal of Applied Electrochemistry* **2012,** *42* (3), 139-144.

136. Murugan, A. V.; Kwon, C.-W.; Campet, G.; Kale, B. B.; Maddanimath, T.; Vijayamohanan, K., Electrochemical lithium insertion into a poly(3,4-ethylenedioxythiophene)PEDOT/V_2O_5 nanocomposite. *Journal of Power Sources* **2002,** *105* (1), 1-5.

137. Chen, Y.; Yang, G.; Zhang, Z.; Yang, X.; Hou, W.; Zhu, J.-J., Polyaniline-intercalated layered vanadium oxide nanocomposites—One-pot hydrothermal synthesis and application in lithium battery. *Nanoscale* **2010,** *2* (10), 2131-2138.

138. Li, X.; Liu, C.; Zhang, C.; Fu, H.; Nan, X.; Ma, W.; Li, Z.; Wang, K.; Wu, H.; Cao, G., Effects of Preinserted Na Ions on Li-Ion Electrochemical Intercalation Properties of V_2O_5. *ACS applied materials & interfaces* **2016,** *8* (37), 24629-24637.

139. Xiao, F.; Song, X.; Li, Z.; Zhang, H.; Zhang, L.; Lei, G.; Xiao, Q.; Hu, Z.; Ding, Y., Embedding of Mg-doped V_2O_5 nanoparticles in a carbon matrix to improve their electrochemical properties for high-energy rechargeable lithium batteries. *Journal of Materials Chemistry A* **2017,** *5* (33), 17432-17441.

140. Zhan, S. Y.; Wei, Y. J.; Bie, X. F.; Wang, C. Z.; Du, F.; Chen, G.; Hu, F., Structural and electrochemical properties of Al^{3+} doped V_2O_5 nanoparticles prepared by an oxalic acid assisted soft-chemical method. *Journal of Alloys and Compounds* **2010,** *502* (1), 92-96.

141. Li, S. R.; Ge, S. Y.; Qiao, Y.; Chen, Y. M.; Feng, X. Y.; Zhu, J. F.; Chen, C. H., Three-dimensional porous $Fe_{0.1}V_2O_{5.15}$ thin film as a cathode material for lithium ion batteries. *Electrochimica Acta* **2012,** *64*, 81-86.

142. Maingot, S.; Deniard, P.; Baffier, N.; Pereira-Ramos, J. P.; Kahn-Harari, A.; Brec, R.; Willmann, P., Origin of the improved cycling capability of sol-gel prepared $Fe_{0.12}V_2O_{5.16}$ compared with V_2O_5. *Journal of Power Sources* **1995,** *54* (2), 342-345.

143. Kryukova, G. N.; Zenkovets, G. A.; Pfänder, N.; Su, D. S.; Schlögl, R., Synthesis and characterization of the titanium doped nanostructural V_2O_5. *Materials Science and Engineering: A* **2003,** *343* (1), 8-12.

144. Sahana, M. B.; Sudakar, C.; Thapa, C.; Naik, V. M.; Auner, G. W.; Naik, R.; Padmanabhan, K. R., The effect of titanium on the lithium intercalation capacity of V_2O_5 thin films. *Thin Solid Films* **2009,** *517* (24), 6642-6651.

145. Zeng, H.; Liu, D.; Zhang, Y.; See, K. A.; Jun, Y.-S.; Wu, G.; Gerbec, J. A.; Ji, X.; Stucky, G. D., Nanostructured Mn-Doped V_2O_5 Cathode Material Fabricated from Layered Vanadium Jarosite. *Chemistry of Materials* **2015,** *27* (21), 7331-7336.

146. Peng, C.; Xiao, F.; Yang, J.; Li, Z.; Lei, G.; Xiao, Q.; Ding, Y.; Hu, Z., Carbon-encapsulated Mn-doped V_2O_5 nanorods with long span life for high-power rechargeable lithium batteries. *Electrochimica Acta* **2016,** *192*, 216-226.

147. Xiao, L.; Zhao, Y.; Yin, J.; Zhang, L., Clewlike ZnV_2O_4 hollow spheres: nonaqueous sol-gel synthesis, formation mechanism, and lithium storage properties. *Chemistry* **2009,** *15* (37), 9442-50.

148. Soudan, P.; Pereira-Ramos, J. P.; Grégoire, G.; Baffier, N., The sol-gel mixed oxide $Cr_{0.11}V_2O_{5.16}$: An attractive cathodic material for secondary lithium batteries. *Ionics* **1997,** *3* (3), 261-264.

149. Zhan, S.; Chen, G.; Liu, D.; Li, A.; Wang, C.; Wei, Y., Effects of Cr doping on the structural and electrochemical properties of V_2O_5. *Journal of Alloys and Compounds* **2009,** *479* (1), 652-656.

150. Wei, Y.; Ryu, C.-W.; Kim, K.-B., Improvement in electrochemical performance of V_2O_5 by Cu doping. *Journal of Power Sources* **2007,** *165* (1), 386-392.

151. Yu, H.; Rui, X.; Tan, H.; Chen, J.; Huang, X.; Xu, C.; Liu, W.; Yu, D. Y. W.; Hng, H. H.; Hoster, H. E.; Yan, Q., Cu doped V_2O_5 flowers as cathode material for high-performance lithium ion batteries. *Nanoscale* **2013,** *5* (11), 4937-4943.

152. Sakunthala, A.; Reddy, M. V.; Selvasekarapandian, S.; Chowdari, B. V. R.; Selvin, P. C., Energy storage studies of bare and doped vanadium pentoxide, $(V_{1.95}M_{0.05})O_5$, M = Nb, Ta, for lithium ion batteries. *Energy & Environmental Science* **2011,** *4* (5), 1712-1725.
153. Chu, Y.-Q.; Qin, Q.-Z., Fabrication and Characterization of Silver−V_2O_5 Composite Thin Films as Lithium-Ion Insertion Materials. *Chemistry of Materials* **2002,** *14* (7), 3152-3157.
154. Lee, J. M.; Hwang, H.-S.; Cho, W.-I.; Cho, B.-W.; Kim, K. Y., Effect of silver co-sputtering on amorphous V_2O_5 thin-films for microbatteries. *Journal of Power Sources* **2004,** *136* (1), 122-131.
155. Xiong, C.; Aliev, A. E.; Gnade, B.; Balkus, K. J., Fabrication of Silver Vanadium Oxide and V_2O_5 Nanowires for Electrochromics. *ACS Nano* **2008,** *2* (2), 293-301.
156. Yao, J. H.; Yin, Z. L.; Zou, Z. G.; Li, Y. W., Y-doped V_2O_5 with enhanced lithium storage performance. *RSC Advances* **2017,** *7* (51), 32327-32335.
157. Li, Y.; Yao, J.; Uchaker, E.; Zhang, M.; Tian, J.; Liu, X.; Cao, G., Sn-Doped V_2O_5 Film with Enhanced Lithium-Ion Storage Performance. *The Journal of Physical Chemistry C* **2013,** *117* (45), 23507-23514.
158. Li, Z.; Zhang, C.; Liu, C.; Fu, H.; Nan, X.; Wang, K.; Li, X.; Ma, W.; Lu, X.; Cao, G., Enhanced Electrochemical Properties of Sn-doped V_2O_5 as a Cathode Material for Lithium Ion Batteries. *Electrochimica Acta* **2016,** *222* (Supplement C), 1831-1838.
159. Huang, X.; Rui, X.; Hng, H. H.; Yan, Q., Vanadium Pentoxide-Based Cathode Materials for Lithium-Ion Batteries: Morphology Control, Carbon Hybridization, and Cation Doping. *Particle & Particle Systems Characterization* **2015,** *32* (3), 276-294.
160. Yoo, H. D.; Shterenberg, I.; Gofer, Y.; Gershinsky, G.; Pour, N.; Aurbach, D., Mg rechargeable batteries: an on-going challenge. *Energy & Environmental Science* **2013,** *6* (8), 2265-2279.
161. Keyzer, E. N.; Glass, H. F. J.; Liu, Z. G.; Bayley, P. M.; Dutton, S. E.; Grey, C. P.; Wright, D. S., $Mg(PF_6)_2$-Based Electrolyte Systems: Understanding Electrolyte-Electrode Interactions for the Development of Mg-Ion Batteries. *Journal of the American Chemical Society* **2016,** *138* (28), 8682-8685.
162. Aurbach, D.; Lu, Z.; Schechter, A.; Gofer, Y.; Gizbar, H.; Turgeman, R.; Cohen, Y.; Moshkovich, M.; Levi, E., Prototype systems for rechargeable magnesium batteries. *Nature* **2000,** *407* (6805), 724-727.
163. Levi, M. D.; Gizbar, H.; Lancry, E.; Gofer, Y.; Levi, E.; Aurbach, D., A comparative study of Mg^{2+} and Li^+ ion insertions into the Mo_6S_8 Chevrel phase using electrochemical impedance spectroscopy. *Journal of Electroanalytical Chemistry* **2004,** *569* (2), 211-223.
164. Levi, M. D.; Lancry, E.; Gizbar, H.; Lu, Z.; Levi, E.; Gofer, Y.; Aurbach, D., Kinetic and thermodynamic studies of Mg^{2+} and Li^+ ion insertion into the Mo_6S_8 Chevrel phase. *Journal of the Electrochemical Society* **2004,** *151* (7), A1044-A1051.
165. Canepa, P.; Sai Gautam, G.; Hannah, D. C.; Malik, R.; Liu, M.; Gallagher, K. G.; Persson, K. A.; Ceder, G., Odyssey of Multivalent Cathode Materials: Open Questions and Future Challenges. *Chemical Reviews* **2017,** *117* (5), 4287-4341.
166. Huie, M. M.; Bock, D. C.; Takeuchi, E. S.; Marschilok, A. C.; Takeuchi, K. J., Cathode materials for magnesium and magnesium-ion based batteries. *Coordination Chemistry Reviews* **2015,** *287*, 15-27.
167. Yu, L.; Zhang, X. G., Electrochemical insertion of magnesium ions into V_2O_5 from aprotic electrolytes with varied water content. *Journal of Colloid and Interface Science* **2004,** *278* (1), 160-165.
168. Kim, R.-H.; Kim, J.-S.; Kim, H.-J.; Chang, W.-S.; Han, D.-W.; Lee, S.-S.; Doo, S.-G., Highly reduced VO_x nanotube cathode materials with ultra-high capacity for magnesium ion batteries. *Journal of Materials Chemistry A* **2014,** *2*, 20636-20641.
169. Andrews, J. L.; Mukherjee, A.; Yoo, H. D.; Parija, A.; Marley, P. M.; Fakra, S.; Prendergast, D.; Cabana, J.; Klie, R. F.; Banerjee, S., Reversible Mg-Ion Insertion in a Metastable One-Dimensional Polymorph of V_2O_5. *Chem* **2018,** *4* (3), 564-585.
170. Cheng, Y.; Shao, Y.; Raju, V.; Ji, X.; Mehdi, B. L.; Han, K. S.; Engelhard, M. H.; Li, G.; Browning, N. D.; Mueller, K. T.; Liu, J., Molecular Storage of Mg Ions with Vanadium Oxide Nanoclusters. *Advanced Functional Materials* **2016,** *26* (20), 3446-3453.

171. Gershinsky, G.; Yoo, H. D.; Gofer, Y.; Aurbach, D., Electrochemical and Spectroscopic Analysis of Mg^{2+} Intercalation into Thin Film Electrodes of Layered Oxides: V_2O_5 and MoO_3. *Langmuir* **2013,** *29* (34), 10964-10972.
172. Okoshi, M.; Yamada, Y.; Komaba, S.; Yamada, A.; Nakai, H., Theoretical Analysis of Interactions between Potassium Ions and Organic Electrolyte Solvents: A Comparison with Lithium, Sodium, and Magnesium Ions. *Journal of The Electrochemical Society* **2017,** *164* (2), A54-A60.
173. Hamon, Y.; Brousse, T.; Jousse, F.; Topart, P.; Buvat, P.; Schleich, D. M., Aluminum negative electrode in lithium ion batteries. *Journal of Power Sources* **2001,** *97-98*, 185-187.
174. Obrovac, M. N.; Chevrier, V. L., Alloy Negative Electrodes for Li-Ion Batteries. *Chemical Reviews* **2014,** *114* (23), 11444-11502.
175. Vaalma, C.; Buchholz, D.; Passerini, S., Non-aqueous potassium-ion batteries: a review. *Current Opinion in Electrochemistry* **2018,** *9*, 41-48.
176. Adams, R. A.; Syu, J. M.; Zhao, Y. P.; Lo, C. T.; Varma, A.; Pol, V. G., Binder-Free N- and O-Rich Carbon Nanofiber Anodes for Long Cycle Life K-Ion Batteries. *ACS applied materials & interfaces* **2017,** *9* (21), 17872-17881.
177. Jian, Z. L.; Luo, W.; Ji, X. L., Carbon Electrodes for K-Ion Batteries. *Journal of the American Chemical Society* **2015,** *137* (36), 11566-11569.
178. Luo, W.; Wan, J. Y.; Ozdemir, B.; Bao, W. Z.; Chen, Y. N.; Dai, J. Q.; Lin, H.; Xu, Y.; Gu, F.; Barone, V.; Hu, L. B., Potassium Ion Batteries with Graphitic Materials. *Nano Letters* **2015,** *15* (11), 7671-7677.
179. Zhao, J.; Zou, X. X.; Zhu, Y. J.; Xu, Y. H.; Wang, C. S., Electrochemical Intercalation of Potassium into Graphite. *Advanced Functional Materials* **2016,** *26* (44), 8103-8110.
180. Liu, L.; Chen, Y.; Xie, Y. H.; Tao, P.; Li, Q. Y.; Yan, C. L., Understanding of the Ultrastable K-Ion Storage of Carbonaceous Anode. *Advanced Functional Materials* **2018,** *28* (29).
181. Xu, Y.; Zhang, C. L.; Zhou, M.; Fu, Q.; Zhao, C. X.; Wu, M. H.; Lei, Y., Highly nitrogen doped carbon nanofibers with superior rate capability and cyclability for potassium ion batteries. *Nature communications* **2018,** *9*.
182. Bin, D.-S.; Lin, X.-J.; Sun, Y.-G.; Xu, Y.-S.; Zhang, K.; Cao, A.-M.; Wan, L.-J., Engineering Hollow Carbon Architecture for High-Performance K-Ion Battery Anode. *Journal of the American Chemical Society* **2018,** *140* (23), 7127-7134.
183. Xing, Z. Y.; Qi, Y. T.; Jian, Z. L.; Ji, X. L., Polynanocrystalline Graphite: A New Carbon Anode with Superior Cycling Performance for K-Ion Batteries. *ACS applied materials & interfaces* **2017,** *9* (5), 4343-4351.
184. Kishore, B.; Venkatesh, G.; Munichandraiah, N., $K_2Ti_4O_9$: A Promising Anode Material for Potassium Ion Batteries. *Journal of the Electrochemical Society* **2016,** *163* (13), A2551-A2554.
185. Han, J.; Xu, M.; Niu, Y.; Li, G.-N.; Wang, M.; Zhang, Y.; Jia, M.; Li, C. m., Exploration of K2Ti8O17 as an anode material for potassium-ion batteries. *Chemical communications* **2016,** *52* (75), 11274-11276.
186. Pal, D.; Abdi, S. H.; Shukla, M., Structural and EPR studies of Lithium inserted layered Potassium tetra titanate $K_2Ti_4O_9$ as material for K ions battery. *Journal of Materials Science-Materials in Electronics* **2015,** *26* (9), 6647-6652.
187. Han, J.; Niu, Y.; Bao, S.-j.; Yu, Y.-N.; Lu, S.-Y.; Xu, M., Nanocubic $KTi_2(PO_4)_3$ electrodes for potassium-ion batteries. *Chemical communications* **2016,** *52* (78), 11661-11664.
188. Naveen, N.; Park, W. B.; Han, S. C.; Singh, S. P.; Jung, Y. H.; Ahn, D.; Sohn, K. S.; Pyo, M., Reversible K^+-Insertion/Deinsertion and Concomitant Na+-Redistribution in P ' 3-$Na_{0.52}CrO_2$ for High-Performance Potassium-Ion Battery Cathodes. *Chemistry of Materials* **2018,** *30* (6), 2049-2057.
189. Kim, H.; Kim, J. C.; Bo, S.-H.; Shi, T.; Kwon, D.-H.; Ceder, G., K-Ion Batteries Based on a P2-Type $K_{0.6}CoO_2$ Cathode. *Advanced Energy Materials* **2017,** *7* (17), 1700098.

190. Wang, X. P.; Xu, X. M.; Niu, C. J.; Meng, J. S.; Huang, M.; Liu, X.; Liu, Z.; Mai, L. Q., Earth Abundant Fe/Mn-Based Layered Oxide Interconnected Nanowires for Advanced K-Ion Full Batteries. *Nano Letters* **2017,** *17* (1), 544-550.

191. Liu, C.; Luo, S.; Huang, H.; Wang, Z.; Hao, A.; Zhai, Y.; Wang, Z., $K_{0.67}Ni_{0.17}Co_{0.17}Mn_{0.66}O_2$: A cathode material for potassium-ion battery. *Electrochemistry Communications* **2017,** *82*, 150-154.

192. Hwang, J. Y.; Kim, J.; Yu, T. Y.; Myung, S. T.; Sun, Y. K., Development of P3-$K_{0.69}CrO_2$ as an ultra-high-performance cathode material for K-ion batteries. *Energy & Environmental Science* **2018,** *11* (10), 2821-2827.

193. Baioun, A.; Kellawi, H.; Falah, A., Nano Prussian Yellow Film Modified Electrode: A Cathode Material for Aqueous Potassium Ion Secondary Battery with Zinc Anode. *Current Nanoscience* **2018,** *14* (3), 227-233.

194. Bie, X. F.; Kubota, K.; Hosaka, T.; Chihara, K.; Komaba, S., A novel K-ion battery: hexacyanoferrate(II)/graphite cell. *Journal of Materials Chemistry A* **2017,** *5* (9), 4325-4330.

195. Pei, Y. H.; Mu, C. N.; Li, H. X.; Li, F. J.; Chen, J., Low-Cost $K_4Fe(CN)_6$ as a High-Voltage Cathode for Potassium-Ion Batteries. *ChemSusChem* **2018,** *11* (8), 1285-1289.

196. Wu, X. Y.; Jian, Z. L.; Li, Z. F.; Ji, X. L., Prussian white analogues as promising cathode for non-aqueous potassium-ion batteries. *Electrochemistry Communications* **2017,** *77*, 54-57.

197. Padigi, P.; Thiebes, J.; Swan, M.; Goncher, G.; Evans, D.; Solanki, R., Prussian Green: A High Rate Capacity Cathode for Potassium Ion Batteries. *Electrochimica Acta* **2015,** *166*, 32-39.

198. Xue, L. G.; Li, Y. T.; Gao, H. C.; Zhou, W. D.; Lu, X. J.; Kaveevivitchai, W.; Manthiram, A.; Goodenough, J. B., Low-Cost High-Energy Potassium Cathode. *Journal of the American Chemical Society* **2017,** *139* (6), 2164-2167.

199. Kim, H.; Seo, D. H.; Bianchini, M.; Clement, R. J.; Kim, H.; Kim, J. C.; Tian, Y. S.; Shi, T.; Yoon, W. S.; Ceder, G., A New Strategy for High-Voltage Cathodes for K-Ion Batteries: Stoichiometric $KVPO_4F$. *Advanced Energy Materials* **2018,** *8* (26).

200. Tian, B.; Tang, W.; Leng, K.; Chen, Z.; Tan, S. J. R.; Peng, C.; Ning, G.-H.; Fu, W.; Su, C.; Zheng, G. W.; Loh, K. P., Phase Transformations in TiS_2 during K Intercalation. *ACS Energy Letters* **2017,** *2* (8), 1835-1840.

201. Ren, X. D.; Zhao, Q.; McCulloch, W. D.; Wu, Y. Y., MoS_2 as a long-life host material for potassium ion intercalation. *Nano Research* **2017,** *10* (4), 1313-1321.

202. Jia, B. R.; Yu, Q. Y.; Zhao, Y. Z.; Qin, M. L.; Wang, W.; Liu, Z. W.; Lao, C. Y.; Liu, Y.; Wu, H. W.; Zhang, Z. L.; Qu, X. H., Bamboo-Like Hollow Tubes with MoS_2/N-Doped-C Interfaces Boost Potassium-Ion Storage. *Advanced Functional Materials* **2018,** *28* (40).

203. Lei, K. X.; Wang, C. C.; Liu, L. J.; Luo, Y. W.; Mu, C. N.; Li, F. J.; Chen, J., A Porous Network of Bismuth Used as the Anode Material for High-Energy-Density Potassium-Ion Batteries. *Angewandte Chemie-International Edition* **2018,** *57* (17), 4687-4691.

204. Liu, Y. J.; Tai, Z. X.; Zhang, Q.; Wang, H. Q.; Pang, W. K.; Liu, H. K.; Konstantinov, K.; Guo, Z. P., A new energy storage system: Rechargeable potassium-selenium battery. *Nano Energy* **2017,** *35*, 36-43.

205. Madec, L.; Gabaudan, V.; Gachot, G.; Stievano, L.; Monconduit, L.; Martinez, H., Paving the Way for K-Ion Batteries: Role of Electrolyte Reactivity through the Example of Sb-Based Electrodes. *ACS applied materials & interfaces* **2018,** *10* (40), 34116-34122.

206. Chen, Y. N.; Luo, W.; Carter, M.; Zhou, L. H.; Dai, J. Q.; Fu, K.; Lacey, S.; Li, T.; Wan, J. Y.; Han, X. G.; Bao, Y. P.; Hu, L. B., Organic electrode for non-aqueous potassium-ion batteries. *Nano Energy* **2015,** *18*, 205-211.

207. Yang, C.; Feng, J. R.; Lv, F.; Zhou, J. H.; Lin, C. F.; Wang, K.; Zhang, Y. L.; Yang, Y.; Wang, W.; Li, J. B.; Guo, S. J., Metallic Graphene-Like VSe_2 Ultrathin Nanosheets: Superior Potassium-Ion Storage and Their Working Mechanism. *Advanced Materials* **2018,** *30* (27), 1800036.

208. Liu, C.; Luo, S.; Huang, H.; Wang, Z.; Wang, Q.; Zhang, Y.; Liu, Y.; Zhai, Y.; Wang, Z., Potassium vanadate $K_{0.23}V_2O_5$ as anode materials for lithium-ion and potassium-ion batteries. *Journal of Power Sources* **2018,** *389*, 77-83.
209. Tian, B.; Tang, W.; Su, C.; Li, Y., Reticular $V_2O_5 \cdot 0.6H_2O$ Xerogel as Cathode for Rechargeable Potassium Ion Batteries. *ACS applied materials & interfaces* **2018,** *10* (1), 642-650.
210. Ye, F.; Lu, D.; Gui, X.; Wang, T.; Zhuang, X.; Luo, W.; Huang, Y., Atomic layer deposition of core-shell structured V_2O_5@CNT sponge as cathode for potassium ion batteries. *Journal of Materiomics* **2018**.
211. Zhu, Y.-H.; Zhang, Q.; Yang, X.; Zhao, E.-Y.; Sun, T.; Zhang, X.-B.; Wang, S.; Yu, X.-Q.; Yan, J.-M.; Jiang, Q., Reconstructed Orthorhombic V_2O_5 Polyhedra for Fast Ion Diffusion in K-Ion Batteries. *Chem* **2019**, *5* (1) 168-179.
212. Clites, M.; Hart, J. L.; Taheri, M. L.; Pomerantseva, E., Chemically Preintercalated Bilayered $K_xV_2O_5$ center dot nH_2O Nanobelts as a High-Performing Cathode Material for K-Ion Batteries. *Acs Energy Letters* **2018,** *3* (3), 562-567.
213. Deng, L.; Niu, X.; Ma, G.; Yang, Z.; Zeng, L.; Zhu, Y.; Guo, L., Layered Potassium Vanadate $K_{0.5}V_2O_5$ as a Cathode Material for Nonaqueous Potassium Ion Batteries. *Advanced Functional Materials* **2018,** *0* (0), 1800670.
214. Jin, T.; Li, H. X.; Li, Y.; Jiao, L. F.; Chen, J., Intercalation pseudocapacitance in flexible and self-standing V_2O_3 porous nanofibers for high-rate and ultra-stable K ion storage. *Nano Energy* **2018,** *50*, 462-467.
215. Wan, F.; Zhang, L.; Dai, X.; Wang, X.; Niu, Z.; Chen, J., Aqueous rechargeable zinc/sodium vanadate batteries with enhanced performance from simultaneous insertion of dual carriers. *Nature communications* **2018,** *9* (1), 1656.
216. Kundu, D.; Adams, B. D.; Duffort, V.; Vajargah, S. H.; Nazar, L. F., A high-capacity and long-life aqueous rechargeable zinc battery using a metal oxide intercalation cathode. *Nature Energy* **2016,** *1* (10), 16119.
217. Song, M.; Tan, H.; Chao, D.; Fan, H. J., Recent Advances in Zn-Ion Batteries. *Advanced Functional Materials* **2018,** *28* (41), 1802564.
218. Xu, C.; Li, B.; Du, H.; Kang, F., Energetic zinc ion chemistry: the rechargeable zinc ion battery. *Angewandte Chemie* **2012,** *51* (4), 933-5.
219. Alfaruqi, M. H.; Mathew, V.; Gim, J.; Kim, S.; Song, J.; Baboo, J. P.; Choi, S. H.; Kim, J., Electrochemically Induced Structural Transformation in a γ-MnO_2 Cathode of a High Capacity Zinc-Ion Battery System. *Chemistry of Materials* **2015,** *27* (10), 3609-3620.
220. Wu, B. K.; Zhang, G. B.; Yan, M. Y.; Xiong, T. F.; He, P.; He, L.; Xu, X.; Mai, L. Q., Graphene Scroll-Coated alpha-MnO_2 Nanowires as High-Performance Cathode Materials for Aqueous Zn-Ion Battery. *Small* **2018,** *14* (13).
221. Alfaruqi, M. H.; Gim, J.; Kim, S.; Song, J.; Jo, J.; Kim, S.; Mathew, V.; Kim, J., Enhanced reversible divalent zinc storage in a structurally stable α-MnO_2 nanorod electrode. *Journal of Power Sources* **2015,** *288* (Supplement C), 320-327.
222. Lee, B.; Yoon, C. S.; Lee, H. R.; Chung, K. Y.; Cho, B. W.; Oh, S. H., Electrochemically-induced reversible transition from the tunneled to layered polymorphs of manganese dioxide. *Scientific reports* **2014,** *4,* 6066.
223. Lee, J.; Ju, J. B.; Cho, W. I.; Cho, B. W.; Oh, S. H., Todorokite-type MnO2 as a zinc-ion intercalating material. *Electrochimica Acta* **2013,** *112* (Supplement C), 138-143.
224. Xu, C.; Chiang, S. W.; Ma, J.; Kang, F., Investigation on Zinc Ion Storage in Alpha Manganese Dioxide for Zinc Ion Battery by Electrochemical Impedance Spectrum. *Journal of The Electrochemical Society* **2013,** *160* (1), A93-A97.
225. Sun, W.; Wang, F.; Hou, S.; Yang, C.; Fan, X.; Ma, Z.; Gao, T.; Han, F.; Hu, R.; Zhu, M.; Wang, C., Zn/MnO_2 Battery Chemistry With H^+ and Zn^{2+} Coinsertion. *Journal of the American Chemical Society* **2017,** *139* (29), 9775-9778.

226. Alfaruqi, M. H.; Gim, J.; Kim, S.; Song, J.; Pham, D. T.; Jo, J.; Xiu, Z.; Mathew, V.; Kim, J., A layered δ-MnO_2 nanoflake cathode with high zinc-storage capacities for eco-friendly battery applications. *Electrochemistry Communications* **2015,** *60* (Supplement C), 121-125.
227. Islam, S.; Alfaruqi, M. H.; Mathew, V.; Song, J.; Kim, S.; Kim, S.; Jo, J.; Baboo, J. P.; Pham, D. T.; Putro, D. Y.; Sun, Y. K.; Kim, J., Facile synthesis and the exploration of the zinc storage mechanism of beta-MnO_2 nanorods with exposed (101) planes as a novel cathode material for high performance eco-friendly zinc-ion batteries. *Journal of Materials Chemistry A* **2017,** *5* (44), 23299-23309.
228. Alfaruqi, M. H.; Islam, S.; Gim, J.; Song, J.; Kim, S.; Pham, D. T.; Jo, J.; Xiu, Z.; Mathew, V.; Kim, J., A high surface area tunnel-type α-MnO_2 nanorod cathode by a simple solvent-free synthesis for rechargeable aqueous zinc-ion batteries. *Chemical Physics Letters* **2016,** *650* (Supplement C), 64-68.
229. Lee, B.; Lee, H. R.; Kim, H.; Chung, K. Y.; Cho, B. W.; Oh, S. H., Elucidating the intercalation mechanism of zinc ions into α-MnO_2 for rechargeable zinc batteries. *Chemical communications* **2015,** *51* (45), 9265-9268.
230. Pan, H.; Shao, Y.; Yan, P.; Cheng, Y.; Han, K. S.; Nie, Z.; Wang, C.; Yang, J.; Li, X.; Bhattacharya, P.; Mueller, K. T.; Liu, J., Reversible aqueous zinc/manganese oxide energy storage from conversion reactions. *Nature Energy* **2016,** *1*, 16039.
231. Wang, R. Y.; Wessells, C. D.; Huggins, R. A.; Cui, Y., Highly Reversible Open Framework Nanoscale Electrodes for Divalent Ion Batteries. *Nano Letters* **2013,** *13* (11), 5748-5752.
232. Lu, K.; Song, B.; Zhang, Y. X.; Ma, H. Y.; Zhang, J. T., Encapsulation of zinc hexacyanoferrate nanocubes with manganese oxide nanosheets for high-performance rechargeable zinc ion batteries. *Journal of Materials Chemistry A* **2017,** *5* (45), 23628-23633.
233. Trócoli, R.; La Mantia, F., An Aqueous Zinc-Ion Battery Based on Copper Hexacyanoferrate. *ChemSusChem* **2015,** *8* (3), 481-485.
234. Zhang, L.; Chen, L.; Zhou, X.; Liu, Z., Towards High-Voltage Aqueous Metal-Ion Batteries Beyond 1.5 V: The Zinc/Zinc Hexacyanoferrate System. *Advanced Energy Materials* **2015,** *5* (2), n/a-n/a.
235. Alfaruqi, M. H.; Mathew, V.; Song, J.; Kim, S.; Islam, S.; Pham, D. T.; Jo, J.; Kim, S.; Baboo, J. P.; Xiu, Z.; Lee, K.-S.; Sun, Y.-K.; Kim, J., Electrochemical Zinc Intercalation in Lithium Vanadium Oxide: A High-Capacity Zinc-Ion Battery Cathode. *Chemistry of Materials* **2017,** *29* (4), 1684-1694.
236. He, P.; Quan, Y. L.; Xu, X.; Yan, M. Y.; Yang, W.; An, Q. Y.; He, L.; Mai, L. Q., High-Performance Aqueous Zinc-Ion Battery Based on Layered $H_2V_3O_8$ Nanowire Cathode. *Small* **2017,** *13* (47).
237. Jo, J. H.; Sun, Y.-K.; Myung, S.-T., Hollandite-type Al-doped $VO_{1.52}(OH)_{0.77}$ as a zinc ion insertion host material. *Journal of Materials Chemistry A* **2017,** *5* (18), 8367-8375.
238. Chuan, X.; Jing, G.; Peng, L.; Xixiang, Z.; N., A. H., Highly Stable Aqueous Zinc-Ion Storage Using a Layered Calcium Vanadium Oxide Bronze Cathode. *Angewandte Chemie International Edition* **2018,** *57* (15), 3943-3948.
239. Chuan, X.; Jing, G.; Yongjiu, L.; Hanfeng, L.; Chao, Z.; N., A. H., Rechargeable Aqueous Zinc-Ion Battery Based on Porous Framework Zinc Pyrovanadate Intercalation Cathode. *Advanced Materials* **2018,** *30* (5), 1705580.
240. Dai, X.; Wan, F.; Zhang, L.; Cao, H.; Niu, Z., Freestanding graphene/VO_2 composite films for highly stable aqueous Zn-ion batteries with superior rate performance. *Energy Storage Materials* **2018**.
241. Ding, J.; Du, Z.; Gu, L.; Li, B.; Wang, L.; Wang, S.; Gong, Y.; Yang, S., Ultrafast Zn^{2+} Intercalation and Deintercalation in Vanadium Dioxide. *Advanced Materials* **2018,** *30* (26), 1800762.
242. He, P.; Zhang, G.; Liao, X.; Yan, M.; Xu, X.; An, Q.; Liu, J.; Mai, L., Sodium Ion Stabilized Vanadium Oxide Nanowire Cathode for High-Performance Zinc-Ion Batteries. *Advanced Energy Materials* **2018**, *8*, 1702463.
243. Hu, P.; Zhu, T.; Wang, X.; Wei, X.; Yan, M.; Li, J.; Luo, W.; Yang, W.; Zhang, W.; Zhou, L.; Zhou, Z.; Mai, L., Highly Durable $Na_2V_6O_{16}\cdot 1.63H_2O$ Nanowire Cathode for Aqueous Zinc-Ion Battery. *Nano Letters* **2018,** *18* (3), 1758-1763.

244. Kundu, D.; Hosseini Vajargah, S.; Wan, L.; Adams, B.; Prendergast, D.; Nazar, L. F., Aqueous vs. nonaqueous Zn-ion batteries: consequences of the desolvation penalty at the interface. *Energy & Environmental Science* **2018,** *11* (4), 881-892.
245. Mengyu, Y.; Pan, H.; Ying, C.; Shanyu, W.; Qiulong, W.; Kangning, Z.; Xu, X.; Qinyou, A.; Yi, S.; Yuyan, S.; T., M. K.; Liqiang, M.; Jun, L.; Jihui, Y., Water-Lubricated Intercalation in $V_2O_5 \cdot nH_2O$ for High-Capacity and High-Rate Aqueous Rechargeable Zinc Batteries. *Advanced Materials* **2018,** *30* (1), 1703725.
246. Park, J. S.; Jo, J. H.; Aniskevich, Y.; Bakavets, A.; Ragoisha, G.; Streltsov, E.; Kim, J.; Myung, S. T., Open-Structured Vanadium Dioxide as an Intercalation Host for Zn Ions: Investigation by First-Principles Calculation and Experiments. *Chemistry of Materials* **2018,** *30* (19), 6777-6787.
247. Qiang, P.; Congli, S.; Yanhao, Y.; Kangning, Z.; Ziyi, Z.; M., V. P.; Gang, C.; Yingjin, W.; Xudong, W., $H_2V_3O_8$ Nanowire/Graphene Electrodes for Aqueous Rechargeable Zinc Ion Batteries with High Rate Capability and Large Capacity. *Advanced Energy Materials* **2018,** *0* (0), 1800144.
248. Sambandam, B.; Soundharrajan, V.; Kim, S.; Alfaruqi, M. H.; Jo, J.; Kim, S.; Mathew, V.; Sun, Y. K.; Kim, J., Aqueous rechargeable Zn-ion batteries: an imperishable and high-energy $Zn_2V_2O_7$ nanowire cathode through intercalation regulation. *Journal of Materials Chemistry A* **2018,** *6* (9), 3850-3856.
249. Sambandam, B.; Soundharrajan, V.; Kim, S.; Alfaruqi, M. H.; Jo, J.; Kim, S.; Mathew, V.; Sun, Y. K.; Kim, J., $K_2V_6O_{16}$ center dot 2.7H_2O nanorod cathode: an advanced intercalation system for high energy aqueous rechargeable Zn-ion batteries. *Journal of Materials Chemistry A* **2018,** *6* (32), 15530-15539.
250. Shen, C.; Li, X.; Li, N.; Xie, K.; Wang, J.-g.; Liu, X.; Wei, B., Graphene-Boosted, High-Performance Aqueous Zn-Ion Battery. *ACS applied materials & interfaces* **2018,** *10* (30), 25446-25453.
251. Soundharrajan, V.; Sambandam, B.; Kim, S.; Alfaruqi, M. H.; Putro, D. Y.; Jo, J.; Kim, S.; Mathew, V.; Sun, Y. K.; Kim, J., $Na_2V_6O_{16}$ center dot 3H_2O Barnesite Nanorod: An Open Door to Display a Stable and High Energy for Aqueous Rechargeable Zn-Ion Batteries as Cathodes. *Nano Letters* **2018,** *18* (4), 2402-2410.
252. Li, W.; Wang, K.; Cheng, S.; Jiang, K., A long-life aqueous Zn-ion battery based on $Na_3V_2(PO_4)_2F_3$ cathode. *Energy Storage Materials* **2018,** *15*, 14-21.
253. He, P.; Yan, M.; Zhang, G.; Sun, R.; Chen, L.; An, Q.; Mai, L., Layered VS2 Nanosheet-Based Aqueous Zn Ion Battery Cathode. *Advanced Energy Materials* **2017,** *7* (11), 1601920.
254. Cheng, Y.; Luo, L.; Zhong, L.; Chen, J.; Li, B.; Wang, W.; Mao, S. X.; Wang, C.; Sprenkle, V. L.; Li, G.; Liu, J., Highly Reversible Zinc-Ion Intercalation into Chevrel Phase Mo_6S_8 Nanocubes and Applications for Advanced Zinc-Ion Batteries. *ACS applied materials & interfaces* **2016,** *8* (22), 13673-13677.
255. Zhang, N.; Cheng, F.; Liu, Y.; Zhao, Q.; Lei, K.; Chen, C.; Liu, X.; Chen, J., Cation-Deficient Spinel $ZnMn_2O_4$ Cathode in $Zn(CF_3SO_3)_2$ Electrolyte for Rechargeable Aqueous Zn-Ion Battery. *Journal of the American Chemical Society* **2016,** *138* (39), 12894-12901.
256. Wu, X.; Xiang, Y.; Peng, Q.; Wu, X.; Li, Y.; Tang, F.; Song, R.; Liu, Z.; He, Z.; Wu, X., Green-low-cost rechargeable aqueous zinc-ion batteries using hollow porous spinel $ZnMn_2O_4$ as the cathode material. *Journal of Materials Chemistry A* **2017,** *5* (34), 17990-17997.
257. Kundu, D.; Oberholzer, P.; Glaros, C.; Bouzid, A.; Tervoort, E.; Pasquarello, A.; Niederberger, M., Organic Cathode for Aqueous Zn-Ion Batteries: Taming a Unique Phase Evolution toward Stable Electrochemical Cycling. *Chemistry of Materials* **2018,** *30* (11), 3874-3881.
258. Qing Zhao, W. H., Zhiqiang Luo, Luojia Liu, Yong Lu, Yixin Li, Lin Li, Jinyan Hu, Hua Ma and Jun Chen,, High-capacity aqueous zinc batteries using sustainable quinone electrodes. *Science Advances* **2018,** *4*, eaao176.
259. Zhou, J.; Shan, L.; Wu, Z.; Guo, X.; Fang, G.; Liang, S., Investigation of V_2O_5 as a low-cost rechargeable aqueous zinc ion battery cathode. *Chemical communications* **2018,** *54* (35), 4457-4460.

260. Zhang, N.; Dong, Y.; Jia, M.; Bian, X.; Wang, Y.; Qiu, M.; Xu, J.; Liu, Y.; Jiao, L.; Cheng, F., Rechargeable Aqueous Zn–V_2O_5 Battery with High Energy Density and Long Cycle Life. *ACS Energy Letters* **2018,** *3* (6), 1366-1372.
261. Huang, W.; Marcelli, A.; Xia, D., Application of Synchrotron Radiation Technologies to Electrode Materials for Li- and Na-Ion Batteries. *Advanced Energy Materials* **2017,** *7* (21), n/a-n/a.
262. McBreen, J.; Mukerjee, S.; Yang, X. Q., In Situ Synchrotron X-ray Studies of Battery and Fuel Cell Materials. *Synchrotron Radiation News* **1998,** *11*, 18.
263. Thurston, T. R.; Jisrawi, N. M.; Mukerjee, S.; Yang, X. Q.; McBreen, J.; Daroux, M. L.; Xing, X. K., Synchrotron X-Ray Diffraction Studies of the Structural Properties of Electrode Materials in Operating Battery Cells. *Appl. Phys. Lett.* **1996,** *69*, 194.
264. Skotheim, T. A.; Yang, X. Q.; Xue, K. H.; Lee, H. S.; McBreen, J.; Lu, F., X-Ray Absorption Studies on Organo-Disulfide Redox Cathodes. *Electrochim. Acta* **1992,** *37*, 1635.
265. McBreen, J.; O'Grady, W. E.; Pandya, K. I., Exafs: A New Tool for the Study of Battery and Fuel Cell Materials. *J. Power Sources* **1988,** *22*, 323.
266. Fauth, F.; Peral, I.; Popescu, C.; Knapp, M., The new Material Science Powder Diffraction beamline at ALBA Synchrotron. *Powder Diffraction* **2013,** *28* (S2), S360-S370.
267. Weckert, E.; Balewski, K.; Brefeld, W.; Decking, W.; Drube, W.; Franz, H.; Gürtler, P.; Hahn, U.; Pflüger, J.; Schulte-Schrepping, H.; Tischer, M.; Schneider, J., PETRA III: A New High Brilliance Synchrotron Radiation Source at DESY. *AIP Conference Proceedings* **2004,** *705* (1), 73-76.
268. Welter, E.; Chernikov, R.; Herrmann, M.; Nemausat, R., A beamline for bulk sample x-ray absorption spectroscopy at the high brilliance storage ring PETRA III. *AIP Conference Proceedings* **2019,** *2054* (1), 040002.
269. Welter, E., Design considerations for a new beamline for standard EXAFS at a high-energy low-emittance storage ring. *Journal of Synchrotron Radiation* **2012,** *19* (6), 905-910.
270. Waluś, S.; Barchasz, C.; Colin, J.-F.; Martin, J.-F.; Elkaïm, E.; Leprêtre, J.-C.; Alloin, F., New insight into the working mechanism of lithium–sulfur batteries: in situ and operando X-ray diffraction characterization. *Chemical communications* **2013,** *49* (72), 7899-7901.
271. Gregory, T. D.; Hoffman, R. J.; Winterton, R. C., Nonaqueous Electrochemistry of Magnesium Applications to Energy Storage. *J. Electrochem. Soc.,* **1990,** *137*, 775-780.
272. Mizrahi, O.; Amir, N.; Pollak, E.; Chusid, O.; Marks, V.; Gottlieb, H.; Larush, L.; Zinigrad, E.; Aurbach, D., Electrolyte solutions with a wide electrochemical window for recharge magnesium batteries. *Journal of the Electrochemical Society* **2008,** *155* (2), A103-A109.
273. Cheng, Y.; Liu, T.; Shao, Y.; Engelhard, M. H.; Liu, J.; Li, G., Electrochemically stable cathode current collectors for rechargeable magnesium batteries. *Journal of Materials Chemistry A* **2014,** *2* (8), 2473-2477.
274. Tang, H.; Peng, Z.; Wu, L.; Xiong, F.; Pei, C.; An, Q.; Mai, L., Vanadium-Based Cathode Materials for Rechargeable Multivalent Batteries: Challenges and Opportunities. *Electrochemical Energy Reviews* **2018,** *1* (2), 169-199.
275. Wang, Z.; Su, Q.; Deng, H., Single-layered V_2O_5 a promising cathode material for rechargeable Li and Mg ion batteries: an ab initio study. *Physical Chemistry Chemical Physics* **2013,** *15* (22), 8705-8709.
276. Zhou, B.; Shi, H.; Cao, R.; Zhang, X.; Jiang, Z., Theoretical study on the initial stage of a magnesium battery based on a V_2O_5 cathode. *Physical Chemistry Chemical Physics* **2014,** *16* (34), 18578-18585.
277. Zhao, X. D.; Zhang, X.; Wu, D. H.; Zhang, H. C.; Ding, F.; Zhou, Z., Ab initio investigations on bulk and monolayer V_2O_5 as cathode materials for Li-, Na-, K- and Mg-ion batteries. *Journal of Materials Chemistry A* **2016,** *4* (42), 16606-16611.
278. Tepavcevic, S.; Liu, Y.; Zhou, D.; Lai, B.; Maser, J.; Zuo, X.; Chan, H.; Král, P.; Johnson, C. S.; Stamenkovic, V.; Markovic, N. M.; Rajh, T., Nanostructured Layered Cathode for Rechargeable Mg-Ion Batteries. *ACS Nano* **2015,** *9* (8), 8194–8205.

279. Lossius, L. P.; Emmenegger, F., Plating of magnesium from organic solvents. *Electrochimica Acta* **1996,** *41* (3), 445-447.

280. Chusid, O.; Gofer, Y.; Gizbar, H.; Vestfrid, Y.; Levi, E.; Aurbach, D.; Riech, I., Solid-state rechargeable magnesium batteries. *Advanced Materials* **2003,** *15* (7-8), 627-630.

281. Chen, Z.; Qin, Y.; Weng, D.; Xiao, Q.; Peng, Y.; Wang, X.; Li, H.; Wei, F.; Lu, Y., Design and Synthesis of Hierarchical Nanowire Composites for Electrochemical Energy Storage. *Advanced Functional Materials* **2009,** *19* (21), 3420-3426.

282. Lancry, E.; Levi, E.; Mitelman, A.; Malovany, S.; Aurbach, D., Molten salt synthesis (MSS) Of $Cu_2Mo_6S_8$- New way for large-scale production of Chevrel phases. *Journal of Solid State Chemistry* **2006,** *179* (6), 1879-1882.

283. Parry, K. L.; Shard, A. G.; Short, R. D.; White, R. G.; Whittle, J. D.; Wright, A., ARXPS characterisation of plasma polymerised surface chemical gradients. *Surface and Interface Analysis* **2006,** *38* (11), 1497-1504.

284. Scofield, J. H., Hartree-Slater subshell photoionization cross-sections at 1254 and 1487 eV. *Journal of Electron Spectroscopy and Related Phenomena* **1976,** *8* (2), 129-137.

285. Tanuma, S.; Powell, C. J.; Penn, D. R., Calculations of electron inelastic mean free paths. V. Data for 14 organic compounds over the 50–2000 eV range. *Surface and Interface Analysis* **1994,** *21* (3), 165-176.

286. Nikolowski, K.; Baehtz, C.; Bramnik, N. N.; Ehrenberg, H., A Swagelok-type in situ cell for battery investigations using synchrotron radiation. *Journal of Applied Crystallography* **2005,** *38*, 851-853.

287. J. Rodríguez-Carvajal, Recent Developments of the Program FULLPROF. *in Commission on Powder Diffraction (IUCr). Newsletter* **2001,** *26*, 12-19.

288. Herklotz, M.; Scheiba, F.; Hinterstein, M.; Nikolowski, K.; Knapp, M.; Dippel, A.-C.; Giebeler, L.; Eckert, J.; Ehrenberg, H., Advances in in situ powder diffraction of battery materials: a case study of the new beamline P02.1 at DESY, Hamburg. *Journal of Applied Crystallography* **2013,** *46* (4), 1117-1127.

289. Ravel, B.; Newville, M., ATHENA, ARTEMIS, HEPHAESTUS: data analysis for X-ray absorption spectroscopy using IFEFFIT. *Journal of Synchrotron Radiation* **2005,** *12* (4), 537-541.

290. Moretti, A.; Passerini, S., Bilayered Nanostructured $V_2O_5{\cdot}nH_2O$ for Metal Batteries. *Advanced Energy Materials* **2016,** *6* (23), 1600868.

291. Arora, P.; White, R. E.; Doyle, M., Capacity Fade Mechanisms and Side Reactions in Lithium-Ion Batteries. *Journal of The Electrochemical Society* **1998,** *145* (10), 3647-3667.

292. Leger, C.; Bach, S.; Soudan, P.; Pereira-Ramos, J. P., Evaluation of the sol–gel mixed oxide $Cr_{0.11}V_2O_{5.16}$ as a rechargeable positive electrode working in the potential range 3.8/1.5 V vs. Li. *Solid State Ionics* **2005,** *176* (15), 1365-1369.

293. Millet, P.; Satto, C.; Sciau, P.; Galy, J., MgV_2O_5 and $\delta Li_xV_2O_5$: A Comparative Structural Investigation. *Journal of Solid State Chemistry* **1998,** *136* (1), 56-62.

294. Pereira-Ramos, J. P.; Messina, R.; Perichon, J., Electrochemical formation of a magnesium vanadium bronze $Mg_xV_2O_5$ in sulfone-based electrolytes at 150°C. *Journal of Electroanalytical Chemistry and Interfacial Electrochemistry* **1987,** *218* (1–2), 241-249.

295. Sai Gautam, G.; Canepa, P.; Abdellahi, A.; Urban, A.; Malik, R.; Ceder, G., The Intercalation Phase Diagram of Mg in V_2O_5 from First-Principles. *Chemistry of Materials* **2015,** *27* (10), 3733-3742.

296. Cocciantelli, J. M.; Doumerc, J. P.; Pouchard, M.; Broussely, M.; Labat, J., Crystal chemistry of electrochemically inserted $Li_xV_2O_5$. *Journal of Power Sources* **1991,** *34* (2), 103-111.

297. Xiao, R.; Xie, J.; Luo, T.; Huang, L.; Zhou, Y.; Yu, D.; Chen, C.; Liu, Y., Phase Transformation and Diffusion Kinetics of V_2O_5 Electrode in Rechargeable Li and Mg Batteries: A First-Principle Study. *The Journal of Physical Chemistry C* **2018,** *122* (3), 1513-1521.

298. S.Crouch-Baker; C-K. Huang; Huggins, R. A., Rationalization of the electrochemical behavior of transition metal oxide positive electrode materials at room temperature. *Proc. Electrochem. Soc.* **1988,** *88-6*, 44.

299. Tanaka, T.; Yamashita, H.; Tsuchitani, R.; Funabiki, T.; Yoshida, S., X-ray absorption (EXAFS/XANES) study of supported vanadium oxide catalysts. Structure of surface vanadium oxide species on silica and [gamma]-alumina at a low level of vanadium loading. *Journal of the Chemical Society, Faraday Transactions 1: Physical Chemistry in Condensed Phases* **1988,** *84* (9), 2987-2999.
300. Wong, J.; Lytle, F. W.; Messmer, R. P.; Maylotte, D. H., K-edge absorption spectra of selected vanadium compounds. *Physical Review B* **1984,** *30* (10), 5596-5610.
301. Yoo, H. D.; Liang, Y.; Dong, H.; Lin, J.; Wang, H.; Liu, Y.; Ma, L.; Wu, T.; Li, Y.; Ru, Q.; Jing, Y.; An, Q.; Zhou, W.; Guo, J.; Lu, J.; Pantelides, S. T.; Qian, X.; Yao, Y., Fast kinetics of magnesium monochloride cations in interlayer-expanded titanium disulfide for magnesium rechargeable batteries. *Nature communications* **2017,** *8* (1), 339.
302. Liu, X.; Wang, D.; Liu, G.; Srinivasan, V.; Liu, Z.; Hussain, Z.; Yang, W., Distinct charge dynamics in battery electrodes revealed by in situ and operando soft X-ray spectroscopy. *Nature communications* **2013,** *4*, 2568.
303. Baddour-Hadjean, R.; Pereira-Ramos, J. P.; Navone, C.; Smirnov, M., Raman Microspectrometry Study of Electrochemical Lithium Intercalation into Sputtered Crystalline V_2O_5 Thin Films. *Chemistry of Materials* **2008,** *20* (5), 1916-1923.
304. Silversmit, G.; Depla, D.; Poelman, H.; Marin, G. B.; De Gryse, R., Determination of the V2p XPS binding energies for different vanadium oxidation states (V^{5+} to V^{0+}). *Journal of Electron Spectroscopy and Related Phenomena* **2004,** *135* (2-3), 167-175.
305. P., L. G.; G., C. D.; D., R. B., XPS O 1s binding energies for polymers containing hydroxyl, ether, ketone and ester groups. *Surface and Interface Analysis* **1991,** *17* (5), 267-272.
306. Zhu, K.; Qiu, H.; Zhang, Y.; Zhang, D.; Chen, G.; Wei, Y., Synergetic Effects of Al^{3+} Doping and Graphene Modification on the Electrochemical Performance of V_2O_5 Cathode Materials. *ChemSusChem* **2015,** *8* (6), 1017-1025.
307. Światowska-Mrowiecka, J.; Maurice, V.; Zanna, S.; Klein, L.; Marcus, P., XPS study of Li ion intercalation in V_2O_5 thin films prepared by thermal oxidation of vanadium metal. *Electrochimica Acta* **2007,** *52* (18), 5644-5653.
308. Eftekhari, A., Potassium secondary cell based on Prussian blue cathode. *Journal of Power Sources* **2004,** *126* (1), 221-228.
309. Eftekhari, A.; Jian, Z.; Ji, X., Potassium Secondary Batteries. *ACS applied materials & interfaces* **2017,** *9* (5), 4404-4419.
310. Parija, A.; Liang, Y.; Andrews, J. L.; De Jesus, L. R.; Prendergast, D.; Banerjee, S., Topochemically De-Intercalated Phases of V_2O_5 as Cathode Materials for Multivalent Intercalation Batteries: A First-Principles Evaluation. *Chemistry of Materials* **2016,** *28* (16), 5611-5620.
311. Bucur, C. B.; Gregory, T.; Oliver, A. G.; Muldoon, J., Confession of a Magnesium Battery. *The Journal of Physical Chemistry Letters* **2015,** *6* (18), 3578-3591.
312. Komaba, S.; Hasegawa, T.; Dahbi, M.; Kubota, K., Potassium intercalation into graphite to realize high-voltage/high-power potassium-ion batteries and potassium-ion capacitors. *Electrochemistry Communications* **2015,** *60*, 172-175.
313. Pramudita, J. C.; Sehrawat, D.; Goonetilleke, D.; Sharma, N., An Initial Review of the Status of Electrode Materials for Potassium-Ion Batteries. *Advanced Energy Materials* **2017,** *7* (24), 1602911.
314. Koch, D.; Kulish, V. V.; Manzhos, S., A first-principles study of potassium insertion in crystalline vanadium oxide phases as possible potassium-ion battery cathode materials. *MRS Communications* **2017,** *7* (4), 819-825.
315. Chen, X.; Wang, L.; Li, H.; Cheng, F.; Chen, J., Porous V_2O_5 nanofibers as cathode materials for rechargeable aqueous zinc-ion batteries. *Journal of Energy Chemistry* **2019**.
316. Frabetti, E.; Deluga, G. A.; Smyrl, W. H.; Giorgetti, M.; Berrettoni, M., X-ray absorption spectroscopy study of $Cu_{0.25}V_2O_5$ and $Zn_{0.25}V_2O_5$ aerogel-like cathodes for lithium batteries. *Journal of Physical Chemistry B* **2004,** *108* (12), 3765-3771.

317. Giorgetti, M.; Berrettoni, M.; Smyrl, W. H., Doped V_2O_5-Based Cathode Materials: Where Does the Doping Metal Go? An X-ray Absorption Spectroscopy Study. *Chemistry of Materials* **2007,** *19* (24), 5991-6000.
318. Hammersley, A., FIT2D: a multi-purpose data reduction, analysis and visualization program. *Journal of Applied Crystallography* **2016,** *49* (2), 646-652.
319. Qiu, X.; Thompson, J. W.; Billinge, S. J. L., PDFgetX2: a GUI-driven program to obtain the pair distribution function from X-ray powder diffraction data. *Journal of Applied Crystallography* **2004,** *37* (4), 678.
320. Farrow, C. L.; Juhas, P.; Liu, J. W.; Bryndin, D.; Božin, E. S.; Bloch, J.; Th, P.; Billinge, S. J. L., PDFfit2 and PDFgui: computer programs for studying nanostructure in crystals. *Journal of Physics: Condensed Matter* **2007,** *19* (33), 335219.
321. Kasnatscheew, J.; Evertz, M.; Streipert, B.; Wagner, R.; Klöpsch, R.; Vortmann, B.; Hahn, H.; Nowak, S.; Amereller, M.; Gentschev, A. C.; Lamp, P.; Winter, M., The truth about the 1st cycle Coulombic efficiency of $LiNi_{1/3}Co_{1/3}Mn_{1/3}O_2$ (NCM) cathodes. *Physical Chemistry Chemical Physics* **2016,** *18* (5), 3956-3965.
322. Gee, B. A.; Wong, A., Vanadium-51 MAS and Static NMR Studies of the Binary $V_2O_5-WO_3$ System. *The Journal of Physical Chemistry B* **2003,** *107* (33), 8382-8387.
323. Pyykkö, P., Year-2008 nuclear quadrupole moments. *Molecular Physics* **2008,** *106* (16-18), 1965-1974.
324. Chen, C. L.; Dong, C. L.; Ho, Y. K.; Chang, C. C.; Wei, D. H.; Chan, T. C.; Chen, J. L.; Jang, W. L.; Hsu, C. C.; Kumar, K.; Wu, M. K., Electronic and atomic structures of gasochromic V_2O_5 films. *EPL (Europhysics Letters)* **2013,** *101* (1), 17006.

Publications

Publications during PhD study:

1. **Qiang Fu***, Angelina Sarapulova, Vanessa Trouillet, Lihua Zhu, Francois Fauth, Stefan Mangold, Edmund Welter, Sylvio Indris, Michael Knapp, Sonia Dsoke, Natalia Bramnik, Helmut Ehrenberg, In operando Synchrotron Diffraction and in operando X-ray Absorption Spectroscopy Investigations of Orthorhombic V_2O_5 Nanowires as Cathode Materials for Mg-Ion Batteries. *J. Am. Chem. Soc.*, 2019, 141 (6), 2305–2315.
2. **Qiang Fu** et al. In operando study of orthorhombic V_2O_5 as cathode materials for K-ion batteries First draft of Manuscript
3. **Qiang Fu** et al. Electrochemical and structural investigation of calcium substituted monoclinic $Li_3V_2(PO_4)_3$ anode materials for Li-ion batteries First draft of Manuscript
4. Yingying Zhao, **Qiang Fu***, Dashuai Wang, Qiang Pang, Yu Gao, Aleksandr Missiul, Ruidy Nemausat, Angelina Sarapulova, Helmut Ehrenberg, Yingjin Wei*, Gang Chen, Co_9S_8@carbon yolk-shell nanocages as a high performance direct conversion anode material for sodium ion batteries. *Energy Storage Materials*, 2018
5. **Qiang Fu**, Raheleh Azmi, Angelina Sarapulova, Daria Mikhailova, Sonia Dsoke, Aleksandr Missiul, Vanessa Trouillet, Michael Knapp, Natalia Bramnik, Helmut Ehrenberg, Electrochemical and structural investigations of different polymorphs of TiO_2 in magnesium and hybrid lithium/magnesium batteries, *Electrochimica Acta*, 2018, 277, 20-29
6. Dongxue Wang, Xiaofei Bie, **Qiang Fu**, Ditty Dixon, Natalia Bramnik, Yongsheng Hu, Francois Fauth, Yingjin Wei, Helmut Ehrenberg, Gang Chen, Fei Du, Sodium vanadium titanium phosphate electrode for symmetric sodium-ion batteries with high power and long lifespan. *Nature communications* 2017, 8.
7. Xiaofei Bian, Yu Gao, **Qiang Fu***, Sylvio Indris, Yanming Ju, Yuan Meng, Fei Du, Natalia Bramnik, Helmut Ehrenberg, Yingjin Wei*, A long cycle-life and high safety Na^+/Mg^{2+} hybrid-ion battery built by using a TiS_2 derived titanium sulfide cathode, *J. Mater. Chem. A*, 2017, 5, 600-608.
8. Zijian Zhao, Guiying Tian, Angelina Sarapulova, Vanessa Trouillet, **Qiang Fu**, Udo Geckle, Helmut Ehrenberg, and Sonia Dsoke, Elucidating the energy storage mechanism of $ZnMn_2O_4$ as promising anode for Li-ion batteries, *J. Mater. Chem. A*, 2018,6, 19381-19392
9. Yingying Zhao, Zhixuan Wei, Qiang Pang, Yingjin Wei, Yongmao Cai, **Qiang Fu**, Fei Du, Angelina Sarapulova, Helmut Ehrenberg, Bingbing Liu, and Gang Chen, NASICON-Type

$Mg_{0.5}Ti_2(PO_4)_3$ Negative Electrode Material Exhibits Different Electrochemical Energy Storage Mechanisms in Na-Ion and Li-Ion Batteries, *ACS Appl. Mater. Interfaces*, 2017, 9 (5), pp 4709–4718.

Previous Publications during master study

1. **Qiang Fu**, Fei Du, Xiaofei Bian, Yuhui Wang, Xiao Yan, Yongquan Zhang, Kai Zhu, Gang Chen, Chunzhong Wang, Yingjin Wei, "Electrochemical performance and thermal stability of $Li_{1.18}Co_{0.15}Ni_{0.15}Mn_{0.52}O_2$ surface coated with the ionic conductor Li_3VO_4", *Journal of Materials Chemistry A*, 2 (2014) 7555-7562.
2. Yuhui. Wang, Xiao. Yan, Xiaofei. Bie, **Qiang. Fu**, Fei. Du, Gang. Chen, Chunzhong. Wang, Yingjin. Wei, "Effects of Aging in Electrolyte on the Structural and Electrochemical Properties of the $Li[Li_{0.18}Ni_{0.15}Co_{0.15}Mn_{0.52}]O_2$ Cathode Material", *Electrochimica Acta*, 116 (2014) 250-257.
3. Rongyu. Zhang, Yongquan. Zhang, Kai. Zhu, Fei. Du, **Qiang. Fu**, Xu. Yang, Yuhui. Wang, Xiaofei. Bie, Gang. Chen, Yingjin. Wei, "Carbon and RuO_2 Binary Surface Coating for the $Li_3V_2(PO_4)_3$ Cathode Material for Lithium-Ion Batteries", *ACS Applied Materials & Interfaces*, 6(2014) 12523-12530
4. Qiang. Pang, **Qiang. Fu**, Yuhui. Wang, Yongquan. Zhang, Bo. Zou, Fei. Du, Gang. Chen, Yingjin. Wei, "Improved Electrochemical Properties of Spinel $LiNi_{0.5}Mn_{1.5}O_4$ Cathode Materials by Surface Modification with RuO_2 Nanoparticles", *Electrochimica. Acta*, 152 (2015) 240-248.
5. Xiaofei Bian, **Qiang Fu**, Chengguang Qiu, Xiaofei Bie, Fei Du, Yuhui Wang, Yongquan Zhang, Hailong Qiu, Gang Chen, Yingjin Wei, "Carbon Black and Vapor Grown Carbon Fibers Binary Conductive Additive for the $Li_{1.18}Co_{0.15}Ni_{0.15}Mn_{0.52}O_2$ Electrodes for Li-ion Batteries", *Materials Chemistry and Physics*, 156 (2015) 69-75.
6. Xiaofei Bian, **Qiang Fu**, Xiaofei Bie, Peilei Yang, Hailong Qiu, Qiang Pang, Gang Chen, Fei Du, Yingjin Wei, "Improved Electrochemical Performance and Thermal Stability of Li-excess $Li_{1.18}Co_{0.15}Ni_{0.15}Mn_{0.52}O_2$ Cathode Material by Li_3PO_4 Surface Coating", *Electrochimica. Acta*, 174 (2015) 875-884.
7. Yongquan Zhang, **Qiang Fu**, Qiaoling Xu, Xiao Yan, Rongyu Zhang, Zhendong Guo, Fei Du, Yingjin Wei, Dong Zhang, and Gang Chen, "Improved Electrochemical Performance of Nitrogen Doped TiO_2-B Nanowires as Anode Materials for Li-ion Batteries", *Nanoscale*, 7 (2015) 12215-12224.
8. Xiaofei Bian, **Qiang Fu**, Hailong Qiu, Fei Du, Yu Gao, Lijie Zhang, Bo Zou, Gang Chen, Yingjin Wei. "High-Performance $Li(Li_{0.18}Ni_{0.15}Co_{0.15}Mn_{0.52})O_2@Li_4M_5O_{12}$ Heterostructured Cathode Material Coated with a Lithium Borate Oxide Glass Layer", *Chemistry of materials*, 27 (2015) 5745-5754

9. Zhendong Guo, Dong Zhang, Hailong Qiu, Tong Zhang, **Qiang Fu**, Lijie Zhang, Xiao Yan, Xing Meng, Gang Chen, Yingjin Wei , “Improved Cycle Stability and Rate Capability of Graphene Oxide Wrapped Tavorite $LiFeSO_4F$ as Cathode Material for Lithium-Ion Batteries”, *ACS Applied Materials & Interfaces*, 7 (2015) 13972-13979.

10. Rongyu Zhang, Xu Yang, Dong Zhang, Hailong Qiu, **Qiang Fu**, Hui Na, ZhenDong Guo, Fei Du, Gang Chen, and Yingjin Wei, “Water Soluble Styrene Butadiene Rubber and Sodium Carboxyl Methyl Cellulose Binder for $ZnFe_2O_4$ Anode Electrodes in Lithium Ion Batteries”, *Journal of Power Sources*, 285 (2015) 227-234.